

Copyright

by

Matthew John Paul

2017

**The Dissertation Committee for Matthew John Paul
certifies that this is the approved version of the following dissertation:**

**Transport and Sorption of Noble Gases
in Porous Geological Media**

Committee:

Steven Biegalski, Supervisor

Derek Haas

Sheldon Landsberger

Justin Lowrey

**Transport and Sorption of Noble Gases
in Porous Geological Media**

by

Matthew John Paul, B.S. C. & Bio. E.; M.S.

Dissertation

Presented to the Faculty of the Graduate School of
The University of Texas at Austin
in Partial Fulfillment
of the Requirements
for the Degree of

Doctor of Philosophy

The University of Texas at Austin

May 2017

Dedication

To my grandfather, Leo, for teaching me the mathematics and physics at a young age. I have strived to be the helluva an engineer you wanted me to be.

To my parents, for their unconditional support throughout my life, especially for those times when I have been more of a ramblin' wreck.

To my fiancée, Abigail, thank you for being yourself. Although this chapter in our lives is over, I cannot wait for what comes next.

Acknowledgements

First and foremost, this work would not have been possible without the guidance and support of Dr. Steven Biegalski; you have provided me a great opportunity and have opened up boundless possibilities for my future. A thank you to Dr. Justin Lowrey and Dr. Derek Haas of whose pioneering work in the field of radionuclide transport identified the idiosyncrasies in xenon transport that served as inspiration for this work. To Dr. Erich Schneider, whose suggestion of identifying the non-dimensional numbers provided much greater clarity to the theory proposed in this work. Finally, a thank you to Dr. Sheldon Landsberger, whose enterprising distance recruiting efforts led to my enrollment, from which all other opportunities followed.

In addition, I would like to thank Dr. Hugh Daigle of Petroleum and Geosystems Engineering, Dr. Ian Riddington of the Chemistry Department, and the other faculty and staff of the University of Texas whose generosity in time and resources make cross-disciplinary research possible.

This work was sponsored in part by the State Department Key Verification Assets Fund (V Fund) project “Exploring the Effect of Ground Water on the Detection of Radioactive Noble Gases from Underground Nuclear Explosions: How Smokin’ is the Smoking Gun?” under Interagency Agreement # SIAA14AVCVTT008 with the Pacific Northwest National Laboratory in 2015. Additional support was provided through the Defense Threat Reduction Agency (Award #HDTRA1-12-1-0009).

Transport and Sorption of Noble Gases in Porous Geological Media

Matthew John Paul, Ph.D.

The University of Texas at Austin, 2017

Supervisor: Steven Biegalski

The transport of noble gas radionuclides in porous media is critical to the detection of underground nuclear explosions as well as the sequestration of reprocessing off-gases. However, in field tests releasing radioxenon underground, the quantity of radioxenon observed at the surface has fallen well below expectations. This research has examined the diffusivity and sorption of noble gases (Ar, Kr, and Xe) and the inert molecular gas sulfur hexafluoride (SF₆) in both dry and wet porous media seeking a plausible mechanism for this discrepancy.

In support of this, the two-bulb method for estimating diffusivity has been modified for experimentation in porous media. To replicate underground transport conditions, low-level concentrations of the tracer gas species were required. Detecting trace quantities of these inert species necessitated the development of precision gas chromatography-mass spectrometry (GC-MS) capabilities for these permanent gases. This was accomplished through the use of internal standards; atmospheric nitrogen, which contains the scarce isotope ¹⁵N, and synthetic carbon tetrafluoride, CF₄, were both

utilized. Both internal standards were shown to be capable of producing acceptable results under ideal conditions, but the CF_4 method showed more resiliency.

The results of the diffusivity trials demonstrated the adequacy of the porosity-tortuosity factor model for both dry and wet macroporous media. However, in both the dry and wet trials, the equilibrium concentration of Xe converged at a lower fraction of initial concentration than the other tracer gases considered.

The deviation in equilibrium fraction is expected in the wet trial due to the increased solubility of Xe versus the other tracer species. However, deviation in the dry trial necessitates consideration of adsorption effects. While the physical adsorption of Xe on shale formations has been considered as a potential mechanism for the scarcity of primordial Xe isotopes in the atmosphere, adsorption measurements were conducted on a range of materials demonstrating not only the relative strength of xenon adsorption over other noble gases, but also that the magnitude of this effect readily exceeds that of solubility. Consequently, with the observation of significant gas adsorption, consideration of adsorbed phase accumulation is necessary when scaling to larger geological systems.

Table of Contents

List of Tables	xii
List of Figures.....	xiv
1. Introduction.....	1
1.1. Motivation	1
1.2. Statement of Goals.....	5
1.3. Organization	6
2. Transport Theory.....	7
2.1. Noble Gas Production.....	7
2.2. Radioactive Decay Kinetics.....	12
2.3. Porous Media	15
2.4. Kinetic Theory of Gases	20
2.5. Maxwell-Stefan Diffusion	29
2.6. Knudsen Diffusion and the Dusty Gas Model.....	30
2.7. Sorption Equilibria	38
2.8. Sorption Kinetics	44
2.9. Absorption Kinetics and Transport.....	46
2.10. Combined Three-phase Model	49
2.11. Double Porosity Model and the Fracture-Matrix Interface	58
2.12. Periodic or Impermeable Boundaries	60
2.13. Initial and Time-Varying Boundary Conditions.....	61
2.14. Diffusive Transport of a Stable Tracer in a Finite Matrix	61

2.15. Diffusive Transport of a Reactive Tracer in a Matrix	63
2.16. Fracture-Matrix Flux	70
3. Gas Chromatography-Mass Spectrometry on Permanent Gases	76
3.1. Selection of Quantitative Method.....	76
3.2. Description of the Gas Chromatography-Mass Spectrometry System	78
3.2.1. Ion Sources.....	79
3.2.2. Mass Analyzers	82
3.2.3. Gas Chromatograph	84
3.3. Quantitative Method Development.....	84
3.3.1. External Calibration	86
3.3.2. Internal Calibration	92
3.3.3. Atmospheric Internal Reference	95
3.3.4. Synthetic Internal Reference	102
3.4. Gas Chromatography via Molecular Sieves	104
4. Quasi-Steady-State Diffusivity Measurements.....	108
4.1. Two-bulb Apparatus	109
4.1.1. Concentration Profile in the Bridge	111
4.1.2. Interfacial Flux	113
4.1.3. Coupled Two-bulb System	114
4.2. Experimental Apparatus	116
4.3. Linear Transformation of Concentration to Ion Count Ratio	119
4.4. Maximum Likelihood Estimate of Eigenvalues and Eigenvectors.....	120

4.5. Nitrogen Standard	126
4.5.1. Results	127
4.5.2. Analysis	135
4.6. Carbon Tetrafluoride Standard	139
4.6.1. Results	139
4.6.2. Analysis	142
4.7. Wet Porous Media	145
4.7.1. Results	146
4.7.2. Analysis	147
4.8. Conclusions	153
5. Adsorption of Permanent Gases on Geological Materials	154
5.1. Methodology	157
5.2. Results:	158
5.3. Analysis	162
5.4. Conclusions	165
6. Conclusions	166
6.3. Attainment of Goals	166
6.4. Major Findings Related to Transport	167
6.3. Findings Related to Laboratory Methods	171
6.4. Recommendations	173
Appendices	174
Appendix A: Quasi-Steady-State Numerical Method	174

Appendix B: Semi-infinite Approximation for Radioactive Tracers.....	177
Bibliography	182
Vita	189

List of Tables

Table 2.1	Half-lives of Noble Gas Radionuclides	11
Table 2.2	Diffusive Decay Length of Noble Gas Radionuclides in Air	70
Table 3.1	Stable Argon, Krypton, and Xenon Weights and Isotopic Abundances.....	81
Table 3.2	Normal Composition of Clean, Dry Atmospheric Air Near Sea Level	95
Table 3.3	Atomic Weights and Abundances of Stable Neon Isotopes	96
Table 3.4	Weights and Abundances of Stable Nitrogen Isotopologues.....	98
Table 4.1	Geometric Parameters of the Two-bulb Apparatus	118
Table 4.2	Unobstructed Two-bulb Apparatus Time Constants	119
Table 4.3	Two-bulb Results Utilizing ^{15}N	136
Table 4.4	Estimated Diffusivities and Porous Media Factors utilizing ^{15}N	136
Table 4.5	Apparent Volumes and Adsorption using Nitrogen	138
Table 4.6	Eigenvalues and Eigenvectors from Concurrent Diffusion Trials.....	142
Table 4.7	Diffusivities Measured using Carbon Tetrafluoride	143
Table 4.8	Asymmetry Measured using Carbon Tetrafluoride	144
Table 4.9	Apparent Volumes and Adsorption using Carbon Tetrafluoride.....	145
Table 4.10	Two-bulb Wet Result Eigenvalues and Eigenvectors.....	147
Table 4.11	Effective Diffusivity of Wet vs. Dry Trials	147
Table 4.12	Reduced Mass Ratio of Tracer Species with Water Vapor and Atmosphere	149
Table 4.13	Comparison of Nitrogen, Knudsen, and Dusty Gas Diffusivities at $1\ \mu\text{m}$.	151

Table 4.14	Apparent Volumes of Tracers in Wet Media versus Argon in Dry Media	.152
Table 5.1	Henry's Law Isotherms for Xenon on Geological Materials162
Table B.1	Infinite-Approximation Parameters for Radioxenon Isotopes179

List of Figures

Figure 1.1	International Monitoring System Stations (Comprehensive Nuclear-Test-Ban Treaty Organization 2017)	2
Figure 2.1	Independent Fast Fission Yields from ^{235}U and ^{235}Pu (Katakura 2011).....	9
Figure 2.2	^{135}Xe Decay Chain from Fission Products	13
Figure 2.3	Effect of Pore Diameter on Diffusivity in Nitrogen	35
Figure 2.4	Solubility of Saturated Fluoride and Noble Gases in Liquid Water.....	41
Figure 2.5	Kr and Xe Adsorption on Shale (Fanale and Cannon 1971)	43
Figure 2.6	Capacity Factor vs. Water Saturation	55
Figure 2.7	Theoretical Flux of ^{37}Ar , ^{127}Xe , and SF_6 undergoing Sorption and Decay	74
Figure 3.1	Atmospheric Xenon Mass Spectrum (Stein 2014)	80
Figure 3.2	The GC-MS at the Nuclear Engineering Teaching Laboratory.....	85
Figure 3.3	Linearity of Xe and SF_6 Target Ion Counts with Concentration	89
Figure 3.4	Concentration vs. Time Utilizing External Calibration.....	90
Figure 3.5	Discontinuities in Target Ion Counts during Irregular Sampling Intervals ...	91
Figure 3.6	Nitrogen Internal Reference Intensity versus Time.....	93
Figure 3.7	Atmospheric Argon Mass Spectrum (Stein 2014)	97
Figure 3.8	Atmospheric Carbon Dioxide Mass Spectrum (Stein 2014)	97
Figure 3.9	Atmospheric Nitrogen Mass Spectrum (Stein 2014).....	99
Figure 3.10	Covariance of Xenon Nuclides vs. $^{15}\text{N}^{14}\text{N}$	100
Figure 3.11	Covariance of Xenon Nuclides vs. ^{132}Xe	101

Figure 3.12	Covariance of Xe, Kr, and SF ₆ vs. CF ₄	103
Figure 3.13	Selected Ion Monitoring Chromatogram using a Molecular Sieve	106
Figure 4.1	Two-bulb Diffusion Apparatus	110
Figure 4.2	Sulfur Hexafluoride Trial	128
Figure 4.3	Semi-logarithmic Sulfur Hexafluoride Trial	129
Figure 4.4	Xenon Trial.....	130
Figure 4.5	Semi-logarithmic Xenon Trial.....	131
Figure 4.6	Krypton Trial	132
Figure 4.7	Semi-logarithmic Krypton Trial	133
Figure 4.8	Argon Trial	134
Figure 4.9	Semi-logarithmic Argon Trial	135
Figure 4.10	Trial 1: Concurrent Diffusion of Kr, Xe, and SF ₆	140
Figure 4.11	Trial 2: Concurrent Diffusion of Kr, Xe, and SF ₆	141
Figure 4.12	Trial 3: Concurrent Diffusion of Kr, Xe, and SF ₆	141
Figure 4.13	Two-bulb Wet Test Results	146
Figure 4.14	Mole Fraction H ₂ O at 100% Humidity	150
Figure 5.1	Noble Gas Abundances in Atmosphere and Chondrites (Fanale and Cannon 1971).....	156
Figure 5.2	Xe Adsorption Isotherms on Geological Media.....	158
Figure 5.3	SF ₆ Adsorption on Geological Media.....	160
Figure 5.4	Ar Adsorption on Geological Media	161
Figure 5.5	Volumetric Capacity vs. Porosity due to Adsorption.....	164

Figure 6.1	Dilution Factor due to a Sorbent Reactive-Diffusive Matrix	169
Figure 6.2	Dilution Factor of Tracer Gases at the NNSS (Olsen, et al. 2016)	170
Figure B.1	Infinite Approximation Fit vs. List-Mode HPGe Data for Radioxenon	178

1. Introduction

1.1. MOTIVATION

The Comprehensive Nuclear-Test-Ban Treaty (CTBT) is a pending treaty that prohibits the detonation of nuclear explosives is prohibited without regard to civil or martial intent. In support of the pending treaty, the Preparatory Commission for the CTBTO has been chartered to develop the International Monitoring System (IMS) and the International Data Centre for the eventual implementation of the treaty. In addition, an On-Site Inspection (OSI) may be conducted as a final verification measure in response to a suspicious event.

The IMS is a network of monitoring stations that seek to identify suspicious events that may be evidence of violations of the CTBT. To that aim, the system consists of four technologies. Three of these technologies - seismic, hydroacoustic, and infrasound, - seek to identify suspicious events underground, underwater, or in the atmosphere. While these methods have the advantage of rapid signal response to events at a distance, these methods cannot necessarily distinguish a nuclear event from other large releases of energy, such as naturally occurring earthquakes or large chemical explosions.

To provide more direct evidence that a suspected event was nuclear in nature, a fourth detection method is employed – radionuclide. This method may consider a wide range of radionuclides, including the fallout of particulates. But if a suspected event has

occurred underground, the likelihood of particulate radionuclides reaching a remote monitoring station may be insufficient. However, not all fission products are solid at ambient conditions. Notably, four radioisotopes of xenon meet the requirements of a suitably long half-life to reach to surface and potentially an IMS detector: ^{131m}Xe , ^{133m}Xe , ^{133}Xe , and ^{135}Xe –. In addition, ^{37}Ar may form as an activation product after high-energy neutrons strike calcium deposits. Figure 1.1 depicts current deployed the IMS stations and their corresponding technologies:

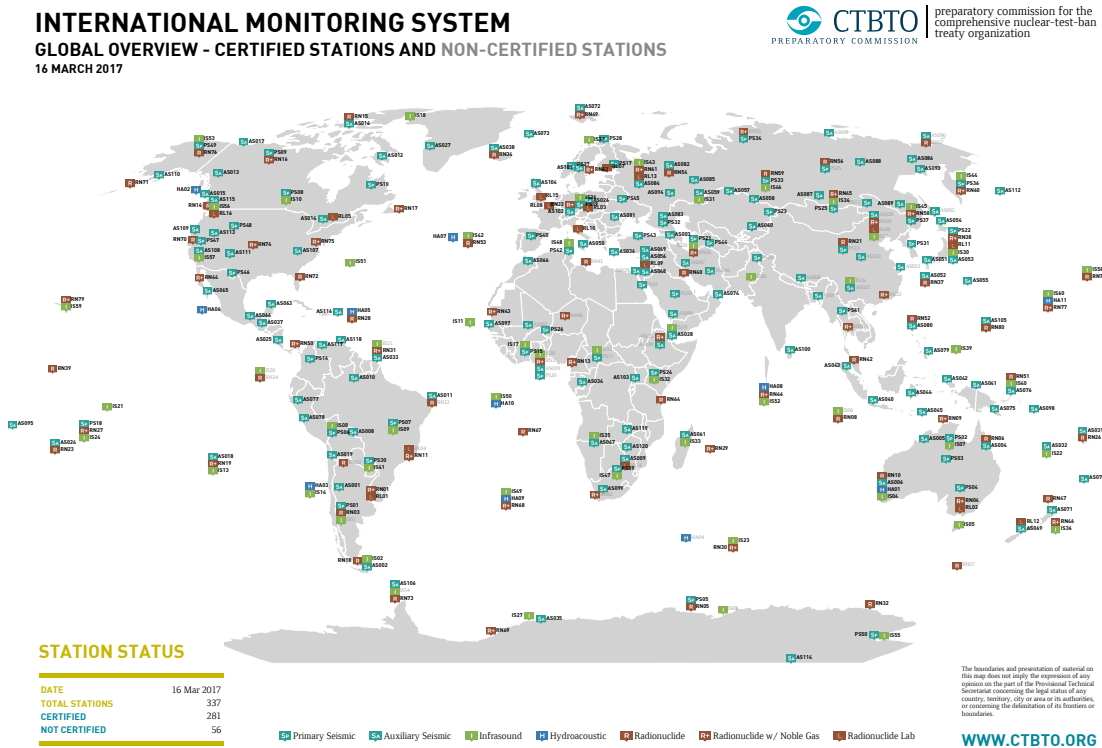


Figure 1.1 International Monitoring System Stations (Comprehensive Nuclear-Test-Ban Treaty Organization 2017)

While the IMS seeks to identify suspicious events from a distance, treaty signatories can request an On-Site Inspection (OSI) of a suspected nuclear test site. Consequently, even if a noble gas tracer is not detected at an IMS station, samples measured during the OSI presumably have a higher likelihood of detection.

A significant question is what levels of radioactivity is expected to reach the surface. Whereas an uncontained nuclear explosion will readily release measureable quantities, a party conducting clandestine nuclear activities may take great care to contain the initial blast. However, even if the initial prompt component is successfully contained, measureable quantities may reach the surface through barometric pumping in the fractured geological material (Nilson, et al. 1991).

The barometric pumping model was later demonstrated in a field test conducted by Lawrence Livermore National Laboratory. In this test, a 1-kilotonne chemical explosive was detonated in a former nuclear test cavity at the Nevada Nuclear Security Site (Carrigan, et al. 1996). However, the tracer gases used in this experiment were not radionuclides but instead sulfur hexafluoride and the scarce isotope of helium, ^3He . While indicative of the transport of stable tracers during barometric pumping, without additional supporting evidence, these results provide only one piece of information as to how radioxenon or radioargon may behave.

While data on the radionuclides in geological media is scarce, in 2013, a team from Pacific Northwest National Laboratory (PNNL) conducted a gas migration experiment at the Nevada National Security Site (NSSL) (Olsen, et al. 2016). ^{127}Xe , ^{37}Ar , and SF_6 were injected in a former nuclear explosion cavity. After 90 days, the cavity was

pressurized and sampled. After accounting for radioactive decay, both ^{127}Xe and ^{37}Ar were depleted with respect to SF_6 . As ^{37}Ar has a significantly higher diffusivity, larger losses to the surrounding rock matrix are not unexpected. However, the magnitude of the Xe loss could not be explained by diffusivity alone.

Similarly, in 1967, significant quantities of ^{133}Xe were injected underground at, what is now the Idaho National Laboratory (Robertson 1969). In this experiment, the objective was exploring a concept to sequester nuclear reprocessing off-gasses, but the construction of the experiment was comparable. Similarly, the quantity of radioxenon detected at the surface fell well below expectations.

With two large field tests reporting a dearth of radioxenon reaching the surface, potential selective loss mechanisms were considered. Despite being a noble gas, xenon is remarkably soluble in water due to the polarizability of its large atomic orbitals and 54 electrons. In contrast, the more commonly used geological tracer gases SF_6 and ^3He have far lower solubility. Even though the previously mentioned tests were conducted in arid environments, groundwater retained in capillary pores is expected regardless of surface conditions.

Additionally, consideration was given to the relative scarcity of xenon in the atmosphere of the earth. While it is assumed that the earth and chondritic meteorites are composed of the same primordial nuclides, there is a significant deficiency of Xe when compared to the abundances of primordial Ne, Ar, and Kr. Thus, aside from the question of whether radioxenon will reach the surface after a nuclear detonation, there is an open question in geophysics as to where the missing xenon may be residing (Sanloup, et al.

2005) (Shcheka and Keppler 2012). As demonstrated by Fanale and Cannon, significant physical adsorption can occur on materials with significant surface areas (Fanale and Cannon 1971). While this may not totally explain the paucity of xenon in the atmosphere, adsorption of Xe by the geological matrix may nevertheless cause a significant reduction in Xe radionuclides migrating to the surface either from an underground nuclear explosion or when sequestering reprocessing off-gases.

1.2. STATEMENT OF GOALS

Goal 1: Identify and establish a model for mechanisms that may selectively dilute xenon versus other tracer gases, notably sulfur hexafluoride and argon. Mechanisms to consider include Knudsen diffusion, surface diffusion, and adsorption into solid media and absorption into retained groundwater.

Goal 2: Develop a reliable process to measure dilute concentrations of both sulfur hexafluoride and noble gases in ordinary atmosphere. As sulfur hexafluoride has no suitable radiological tracer forms and molecular spectroscopy cannot be performed on monatomic noble gases, mass spectrometry has been identified for development.

Goal 3: Measure the diffusivity of the gas tracers in porous geological media to determine the acceptability of the porosity-tortuosity model or if additional parameters need be considered. These measurements must be both reliable and reproducible.

Goal 4: Measure the effects of surface adsorption on a variety of geological material and assess the impact of these effects on geological transport in an open field scenario.

1.3. ORGANIZATION

In support of these goals, this dissertation has been divided into chapters tied to each of these aims. Chapter 2 details both the fundamentals of gas diffusion and porous media parameters that are necessary to develop a method for which to measure diffusivity. In addition, a model is proposed for which to assess the impact of solubility of tracer gases into retained water and for surface adsorption.

Chapter 3 details the development of quantitative gas chromatography-mass spectrometry (GC-MS) techniques developed to support this work. Because microscopic gas volumes are difficult to extract reliable aliquots from, considerable effort was required to develop robust, precise, and accuracy quantitative methods.

Chapter 4 details the implementation and execution of a two-bulb quasi-steady-state method of determining the diffusivity of the dilute tracer gases in porous media. While this method was originally developed for use with mass spectrometry, the inclusion of sorbent porous media posed unique challenges. The results of these experiments are reported and discussed.

Chapter 5 reports the measurement of tracer gas adsorption isotherms on a variety of geological materials. The implication of these results are discussed in the context of both the diffusivity measurements of Chapter 4 and the Transport theory of chapter 2.

Finally, Chapter 6 provides a summary of the findings and provides a brief analysis as to how sorption may enhance diffusive transport as viewed from the fracture.

2. Transport Theory

The primary challenge in determining the quantity of a radionuclide, or chemical tracer, that may reach the surface is determining how the tracer will distribute itself throughout the geological system. As the boundaries of the geological system cannot be controlled, an estimation of the quantities lost to inaccessible areas must be made to account for observations made at the surface. Employing a control volume approach to a material balance, the following equation simply states that the rate of accumulation or depletion of a chemical or radionuclide species i in a volume V must equal the rate at which that material transports across the boundaries of that volume or is created or destroyed by chemical or nuclear reactions:

$$\frac{\partial}{\partial t} \int_V c_i dV = - \oint_V N_i \cdot dA + \int_V r_i dV$$

Throughout, c_i will represent the molar volumetric concentration, N_i as the net molar flux, and r_i as the molar reaction rate, each for respective species i . Due to the presence of porous media and potentially an aqueous liquid phase, there are considerable nuances that must be accounted for when calculating the molar flux. However, as radioactivity is paramount, it will be discussed first.

2.1. NOBLE GAS PRODUCTION

In a nuclear detonation, radioisotopes of noble gas elements may be formed by a variety of processes. The heavier noble gases krypton and xenon are predominately

formed from fission products whereas argon may be formed as an activation product. However, all of these species are unstable and will decay with a characteristic time known as a half-life. Fortunately, the decay of these species is accompanied by the emission of characteristic photons, beta particles, or both, enabling exceedingly small molar concentrations to be detected.

In a fission reaction, a neutron interacts with a fissionable nuclide. Provided the neutron has sufficient energy, the nucleus is destabilized and breaks into two charged fragments and additional neutrons. In a nuclear explosion, an uncontrolled chain reaction occurs, resulting in the rapid escalation of the neutron population and the fissionable material is rapidly consumed. The resulting distribution of protons and neutrons in the fission fragments is dependent on the fissionable nuclide and the energy of the incident neutron. Figure 2.1 depicts the independent fast fission yield, by atomic number, for ^{235}U and ^{239}Pu using data available from the Japanese Atomic Energy Agency (Katakura 2011).

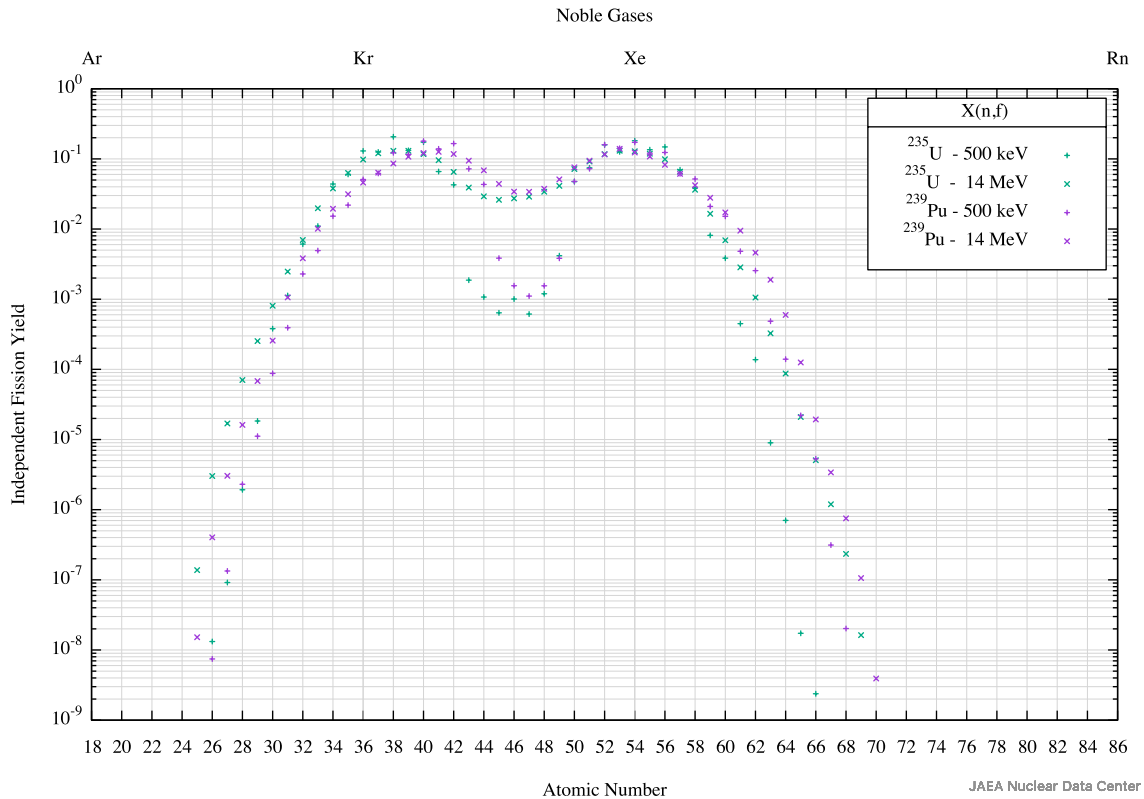


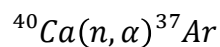
Figure 2.1 Independent Fast Fission Yields from ^{235}U and ^{239}Pu (Katakura 2011)

For reference, the atomic numbers of the noble gas elements are located at the upper x-axis. While neither curve is entirely representative of the fission fragments formed by a nuclear explosive, because there is insufficient time to thermalize neutrons in a nuclear explosion, the incident neutron energy must be somewhere between these fast ranges. What this figure does illustrate is that krypton and xenon nuclides are among the most common independent products formed uranium and plutonium fission for a range of neutron energies.

In addition to the independent fission yield, additional krypton or xenon may be produced by beta decay of adjacent nuclides. In beta decay, an electron or positron is emitted, changing the atomic number of the nucleus. Because both uranium and

plutonium have an excess number of neutrons for their fission fragments, these fragments tend to be neutron rich and decay by electron emission. Through this mechanism, neutron-rich isotopes of iodine will beta decay to isotopes of xenon. Some of these xenon isotopes will also be neutron-rich and beta-decay to cesium. These radioisotopes of xenon are of primary interest as they are detectable at trace concentration. As a consequence of this decay, the source of radiokrypton and radioxenon has both a prompt and delayed component.

The other route of noble gas production is through neutron activation. Neutrons that are not absorbed by the nuclear device will be released to the surrounding geological material. While the geological makeup of a suspected nuclear site will vary, the most ubiquitous terrestrial elements are expected to be present. Calcium, which is the fifth-most abundant element in the earth's crust, is of particular interest. Approximately 96% of all terrestrial calcium is the isotope ^{40}Ca , which can undergo the following nuclear reaction with neutrons of sufficient energy:



While the cross-section for this reaction is not known precisely, experiments conducted at the Nuclear Engineering Teaching Lab (NETL) suggest it is the tens of millibarns for epithermal neutrons sourced from a TRIGA reactor (Egnatuk and Biegalski 2013). Of course, the neutron spectrum from a nuclear explosive would have far more neutrons exceeding the 0.5-MeV threshold for this reaction. Regardless of the precision cross-section, the total quantity of ^{37}Ar produced will be largely dependent upon the abundance of calcium in the local geology.

Once the noble gases form in the geological medium, they must be transported to the surface in order to be detected. If the nuclear explosion is not fully contained, there may be a prompt radionuclide signature. However, even if the initial explosion is effectively contained, there is a possibility that the radionuclides may seep to the surface (Ringbom and Miley 2009). The time to transport the produced gases will vary with depth, geology, hydrology, and meteorology, but it is anticipated to take on the order of weeks for a detonation 400 m below the surface (Carrigan, et al. 1996). Consequently, only noble gas radionuclides that will be present after this period of time are utilizable. Table 2.1 lists the half-lives of noble gas radionuclides being considered by the CTBTO (Saey 2007). All half-lives reported were obtained from the National Nuclear Data Center (Tuli 2005).

Table 2.1 Half-lives of Noble Gas Radionuclides

Radionuclide	Half-life (h)
³⁷ Ar	838.8
⁸⁵ Kr	94003.2
^{131m} Xe	286.4
^{133m} Xe	52.6
¹³³ Xe	125.8
¹³⁵ Xe	9.1

While some of these radionuclides have half-lives that would indicate they would not be present in significant quantities if only emitted from a prompt source, the delayed creation through beta-decay may result in detections over extended periods of time.

2.2. RADIOACTIVE DECAY KINETICS

In contrast to the other aspects of tracer gas transport, the kinetics of radioactive decay are well known and independent of temperature, pressure, physical phase, and essentially all other external conditions. In the absence of a delayed source, the activity A_i of a radionuclide i in a closed system will follow first-order decay kinetics:

$$\frac{dA_i}{dt} = -\lambda_i A_i$$

Here, λ_i is the decay constant for a particular radionuclide. As this rate equation is linear and first order, the solution is the exponential decay curve:

$$A_i(t) = A_i(0)e^{-\lambda_i t}$$

To be consistent with the definition of a half-life, the decay constant is related to the half-life $T_{1/2}$ by:

$$\lambda_i = \frac{\ln(2)}{T_{1/2,i}}$$

With the possibility of a parent radionuclide, the situation becomes more complex. As mentioned earlier, neutron-rich iodine isotopes tend to form xenon through beta decay. However, neutron-rich tellurium also will form radioiodine through beta decay. Figure 2.2 depicts some of the direct and indirect pathways that may form ^{135}Xe from the fission of uranium or plutonium. The curved arrows indicate independent fission yield while the straight arrows indicate subsequent decay reactions.

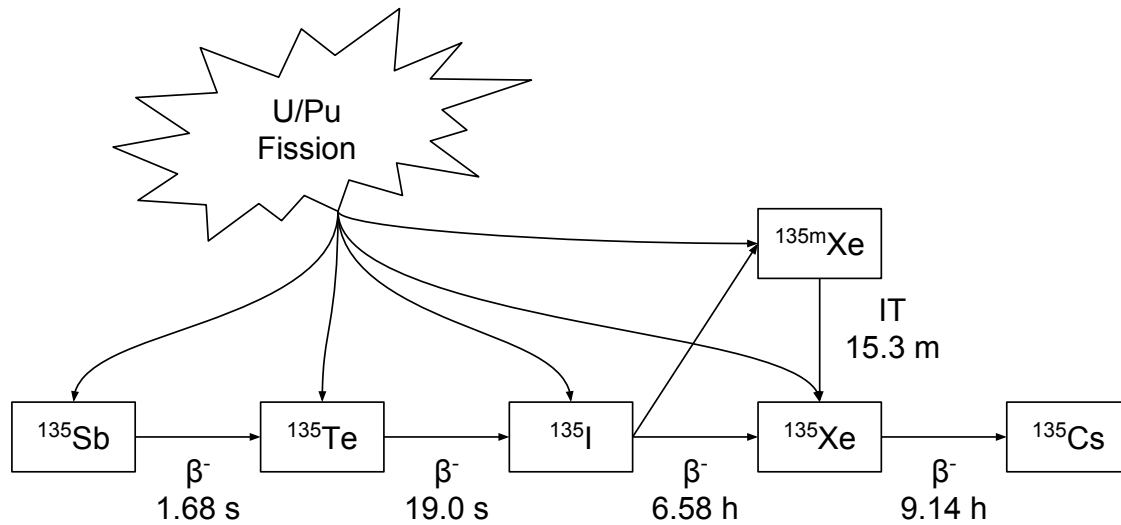


Figure 2.2 ^{135}Xe Decay Chain from Fission Products

This figure also depicts that ^{135}I decay may result in either ^{135}Xe or $^{135\text{m}}\text{Xe}$. In this instance, ^{135}I yields $^{135\text{m}}\text{Xe}$ only 1.9% of the time with the balance yielding ^{135}Xe directly. Due to the relative magnitudes, the significance of branching is limited here, but it nevertheless illustrates the need to account for such possibilities.

For a closed system, the cumulative decay and production of a nuclide i from a mixture of n radionuclides results in the system of n differential equations:

$$\frac{dA_i}{dt} = -\lambda_i A_i + \sum_{j \neq i}^n f_{i,j} \lambda_j A_j$$

Here $f_{i,j}$ represents the branching fraction that is the fraction of decays of a parent nuclide j that results in the daughter i . Since each of these equations is linear and first order, albeit inhomogeneous, this system of equations can be solved using Laplace transforms. In the absence of branches, the general solution found using this method is well known as the Bateman Equations (Bateman 1910).

While the Bateman Equations can provide an accurate measurement of the total inventory of a radionuclide, the total activity of radionuclides cannot be directly observed from the surface. In practice, detection of trace quantities of noble gas radionuclides requires large volumes of air to be collected, concentrated, and separated from background radon, before being counted low-level gas proportional counter or beta-gamma coincidence detector – depending on the radionuclide. With rigorous methodology, the minimum detectable concentration of ^{133}Xe activity is 1 mBq/m³ or less after a 24-hour counting period (Schulze, Auer and Werzi 2000). The molar concentration of a species can then be calculated from the activity concentration by dividing by the decay constant and the Avogadro number:

$$c_i = \frac{A_i/V}{N_A \lambda_i}$$

From this, it can be calculated that, with a minimum detectable concentration of 1 mBq/m³ ^{133}Xe is equivalent to molar concentration of 1.1×10^{-21} mol/m³ of ^{133}Xe . Assuming standard temperature and pressure (STP) conditions, this is a mole fraction of approximately 2.4×10^{-23} . This is impossibly small fraction to measure by chemical techniques, but as the molar concentration is equally applicable to stable gas tracers, this form of concentration will be used henceforth.

As the molar concentration is directly proportional to the activity concentration, the rate of radioactive decay necessary for the control volume can be written as:

$$r_i(c_i, c_j, \dots, c_n) = -\lambda_i c_i + \sum_{i \neq j}^n f_{i,j} \lambda_j c_j$$

With the exception of $^{133\text{m}}\text{Xe}$ isomeric transition to ^{133}Xe , the parent radionuclides of the noble gas tracers are not generally found in the gas phase. While the delayed production of noble gas radionuclides is an important aspect to the OSI, it is not critical far from the source material. In the absence of parent radionuclides in proximity of the media being considered, the reaction rate reduces to a homogeneous form:

$$r_i(c_i) = -\lambda_i c_i$$

Of course, for a stable nuclide or an inert chemical tracer, the reaction rate is zero.

2.3. POROUS MEDIA

In contrast to radioactive decay, the remaining parameters of the transport equation are strongly dependent upon not only temperature and pressure, but also the presence of absence of solid or liquid phases. Because of the presence of a solid and liquid phase, it is apparent that the gas concentration cannot be homogeneous throughout the media. A logical approach is to separate the control volume into three distinct regions by phase, solid, liquid and gas. In doing so, there are six distinct surface interfaces, gas-gas, gas-liquid, gas-solid, liquid-liquid, liquid-solid, and solid-solid. Consequently, expressions are necessary for concentration in each of the three phases and for flux in each of the six interfaces.

Further complicating this problem is that each of these volumes and surfaces are in close proximity. Considering the number of disconnected pore, liquid, and solid volumes possible, modeling individual control volumes for each particular region is an

unreasonable endeavor. Instead, the approach used will follow the concept of the representative elementary volume (REV) as set form by Bear. (Bear 1972)

While the distribution of the solid, liquid, and gas phases is clearly discontinuous on a microscopic scale, the REV is selected such that the average of this heterogeneity is nearly constant from one region to the next. That is, for pores on the order of millimeters, the REV may be on the order of centimeters. While heterogeneity may occur on a scale larger than this, the number of control volumes necessary to model a discontinuous system is still dramatically reduced.

Within an REV, the concept of porosity can be defined. Generally speaking, porosity is the volumetric fraction of the REV not occupied by the solid phase. A more rigorous definition specifies that not only is this volume devoid of solid material but also that is interconnected to other void regions. That is to say, regions totally engulfed by the solid phase cannot interchange fluids with other regions and thereby do not contribute to the porosity. Denoted the volume of the interconnected pores as the void space, the volumetric porosity is defined as:

$$\varepsilon_V = \frac{V_{void}}{V_{void} + V_{solid}}$$

For an isotropic media, the volumetric porosity must be differentiable in each direction consistently. Under this requirement, the areal porosity on the surfaces of the REV must be equal to the volumetric porosity:

$$\varepsilon_x = \varepsilon_y = \varepsilon_z = \frac{A_{void}}{A_{void} + A_{solid}} = \varepsilon_V$$

Throughout this work, the geological media will be assumed to be isotropic. Consequently, the volumetric and areal porosities will be referred to simply as the porosity, ε .

A second characteristic relevant to transport through porous media is its tortuosity. Unlike porosity, the tortuosity has a more tenuous definition. Carman defined the tortuosity as the degree to which a streamline is deflected by the solid media (Carman 1956). By this definition, the tortuosity is defined as the average microscopic distance travelled to result in a macroscopic displacement.

$$q = \frac{L_{distance}}{L_{displacement}}$$

Unfortunately, it is not generally known what path a streamline will take in a disordered structure. The length traversed in turbulent flow will greatly vary from the length traversed by viscous flow. In the limit of stagnant flow, the path traversed by a molecule transported only by diffusion may be different still. Albeit inconsistent with differing flow conditions, this ratio is nevertheless greater than unity for randomly packed geological media.

In addition to the volume displaced by the solid media, some or all of the void space may be occupied by one or more liquid phases. In geological systems, these phases are typically aqueous or organic. Similarly to the porosity, the volume of the a liquid phase α can be expressed as a fraction of the total REV:

$$\theta_{\alpha} = \frac{V_{\alpha}}{V_{total}}$$

However, because some of the REV is occupied by the solid phase, the volumetric content of all liquid phases is limited to be the additive complement of the porosity. The degree of saturation for a fluid α , or simply saturation, is then:

$$S_{\alpha} = \frac{V_{\alpha}}{V_{void}} = \frac{V_{\alpha}}{\varepsilon V_{total}}$$

As UNE are not anticipated to be conducted in petroleum reservoirs, only a single aqueous phase will be considered. Consequently, the subscript for the identity of the liquid phase will be dropped.

Water retained in porous media can be separated into two zones: the saturated and the unsaturated. A region is said to be saturated when the majority of the pore volume is filled with the liquid phase. As the liquid phase is far denser than the gas phase, the liquid tends to drain under the influence of gravity. Therefore, for a region to remain saturated, the liquid phase must be supported by fluid pressure from below. This condition occurs at a depth known as the water table. Regions below the water table are said to be the saturated or phreatic zone. While some trapped gas pockets may exist, they may not be contiguous and the rate of gas transport is severely hindered. Of course, some gas may solvate into the liquid phase, but transport in this region is not of primary focus for noble gas migration to the surface.

The second region is the unsaturated region or vadose zone. Through surface tension, water tends to adhere more strongly to most solid phases than the gas phase, it is known as the wetting fluid. This can be observed visually as water forms a concave meniscus with glassware and develops a capillary pressure. The capillary pressure is then

able to retain the dense liquid phase within narrow pores without the support of a hydrostatic pressure from below. In this region, the liquid phase is presumed to be stagnant, although rainfall and snowmelt percolating through may result in transient advective flux downwards.

As the solid and liquid phases volumes have been defined, the remaining volume must be filled with the gas phase. With a singular liquid phase, the ratio of gas volume to total volume is:

$$\frac{V_{gas}}{V_{total}} = \varepsilon(1 - S)$$

The impact of water content on tortuosity is not as straightforward. Because of the wetting properties of water, water will disproportionately adhere to rough or tortuous paths. For example, a cul-de-sac pore has contact angles that support the retention of wetting liquids. However, a cul-de-sac also represents a far more tortuous pathway to both advection and diffusion. Because these pores are preferentially filled by the wetting liquid, the remaining gas volume may have a smoother and more direct pathways, albeit less of them. Presuming the areal porosity is adequately truncated by the degree of saturation, and as the exact tortuosity is generally not known in the dry media to begin with, no corrections will be made to tortuosity versus water content.

Returning to the material balance, the control volume can be integrated on three distinct regions of the REV: solid, liquid, and gas.

$$\frac{\partial}{\partial t} \int_{(1-\varepsilon)V} c_{i,s} dV = - \oint_{(1-\varepsilon)V} N_i \cdot dA + \int_{(1-\varepsilon)V} r_i(c_{i,s}) dV$$

$$\frac{\partial}{\partial t} \int_{\varepsilon SV} c_{i,l} dV = - \oint_{\varepsilon SV} N_i \cdot dA + \int_{\varepsilon SV} r_i(c_{i,l}) dV$$

$$\frac{\partial}{\partial t} \int_{\varepsilon(1-S)V} c_{i,g} dV = - \oint_{\varepsilon(1-S)V} N_i \cdot dA + \int_{\varepsilon(1-S)V} r_i(c_{i,g}) dV$$

Fortunately, as radioactivity is unaffected by material phase, a separate expression for the reaction rate term is unnecessary. While separating into three control volumes conserves the total volume, the area on which to evaluate the surface integrals has increased.

As the gas phase concentration is the only quantity observable in an OSI, the liquid and solid phase concentrations will be expressed as a function of this quantity. The properties of the gas, liquid, and solid phases will be considered to develop expressions for both the intra- and inter-facial fluxes.

2.4. KINETIC THEORY OF GASES

The kinetic theory of gases is a successful mathematical model that establishes not only the equilibrium properties of a gas, but also non-equilibrium behavior. As a system undergoing transport is, by its very nature, not in thermodynamic equilibrium, kinetic theory is the foundation for the analytical treatment of diffusion. The details of this theory are laid out in a number of texts (D. A. McQuarrie 2000), with pioneering work developed by Chapman and Cowling (Chapman and Cowling 1970). Central to this theorem is the premise that a gas is composed of numerous particles of finite mass but with variable position, momentum, and kinetic energy. Typically, these particles are

either atoms — as they are for noble gases — or molecules. These particles can transfer momentum and kinetic energy with one another through collisions or, more generally speaking, encounters. That is to say, a particle only needs to come under the influence of the presence of another particle and they need not directly collide.

In addition, the volume of these particles is assumed to be very small in contrast with the total volume a gas occupies. Because of this, the average distance between any two particles is, in contrast, very large. Consequently, the likelihood of more than two particles being in proximity to each other is exceedingly small. Therefore, only binary collisions or encounter are likely and are considered to be only interactions of importance.

Furthermore, only translational motion is significant for predicting transport properties. While molecules may have modes of vibration or rotation, this energy is not as readily transferrable to molecules of a different type. Classically, the kinetic energy for the particle i is defined as:

$$E_i = \frac{1}{2} m_i v_i^2$$

Here m_i is the mass and v_i is the velocity of the particle. However, because of the immense number of particles involved, it is not practical to track the trajectory of all the particles in the system. Instead, probabilistic arguments must be made.

To describe the properties of the gas, a solution for the probability distribution of the particles in both position and velocity spaces is sought. As the system may not be in equilibrium, this distribution may also be a function of time. In addition, due to

differences in molecular weight, the velocity distribution of two different gas species will be different, even at equilibrium. Consequently, each distinguishable gas species will have its own probability distribution.

Because the total number of particles is – neglecting chemical or nuclear reactions – conserved, the distribution f_i must be normalized such that integrating over all possible velocities yields the number density – or molar concentration – for that species.

$$c_i = \int f_i(r, v, t) dv$$

Here, $f_i(r, v, t)$ is the probability distribution for a species i as a function of position r , velocity v , and time t . In addition to the molar concentration, the molar flux in the gas phase can also be found by integrating the probability distribution weighted by velocity:

$$N_i = c_i \bar{v} = \int v f_i(r, v, t) dv$$

For brevity, the bar notation indicated a weighted property. As velocity is a vector, it may have positive and negative components in the probability distribution. An imbalance in the average velocity indicated particles are, as a whole, migrating in position.

In addition to these two quantities, which appear directly in the gas-phase control volume, the hydrostatic partial pressure, p_i , is found to be the mean momentum transferred of stagnant gas particles of species i impinging on a solid surface. As gas is free to travel in three dimensions, is one third of the total averaged squared velocity is

incident on the solid surface. Weighting this by the molecular weight gives a measure of the momentum transferred:

$$p_i = \frac{1}{3} c_i m_i \overline{v_i^2}$$

Integrating the probability distribution of each species weighted by their own mass and mean squared velocity subsequently yields the total hydrostatic pressure, P , as a sum of the partial pressures, demonstrating Dalton's Law:

$$P = \frac{1}{3} \sum_i^n c_i m_i \overline{v_i^2}$$

A central postulate of kinetic theory is that the kinetic energy of a gas is directly proportional to temperature T . This relates the kinetic temperature to the mean squared velocity. The constant of proportionality, k , is known as the Boltzmann constant.

$$\overline{E}_i = \frac{1}{2} m_i \overline{v_i^2} = \frac{3}{2} kT$$

Combined with the previous derivation of pressure demonstrates that this postulate is sufficient to demonstrate the ideal gas law:

$$c_i = \frac{p_i}{N_A kT} = \frac{p_i}{RT}$$

Here, it is evident that the Boltzmann constant times the Avogadro number is equivalent to the ideal gas constant, R . As will be shown, this is one aspect of kinetic theory necessary to relate the concentration of the various phases. However, a more detailed determination of the probability distribution is necessary to evaluate the molar flux.

To do so requires additional information about the nature of the distribution and how it responds in time from a non-equilibrium state. Complicating the matter is that the position and velocity are dependent in time. From fundamental mathematical principles, the total derivative of the distribution in time can be found as a function of partial derivatives of each variable weighted by their own time dependence:

$$\frac{D}{Dt} f(r, v, t) = \frac{\partial f}{\partial t} + \frac{dr}{dt} \cdot \frac{\partial f}{\partial r} + \frac{dv}{dt} \cdot \frac{\partial f}{\partial v}$$

Fortunately, the change in position with respect to time, $\frac{dr}{dt}$, is simply the particle velocity v . From Newton's Second Law of Motion, the change in velocity of a particle is simply the net force F exerted over the mass m_i . This results in the Boltzmann Transport Equation:

$$\frac{Df}{Dt} = \frac{\partial f}{\partial t} + v \cdot \frac{\partial f}{\partial r} + \frac{F}{m_i} \cdot \frac{\partial f}{\partial v}$$

In the absence of reactions altering the quantity of the gas particles, $\frac{\partial f}{\partial t}$, or collisions or other forces altering their velocities, $\frac{F}{m_i}$, the velocities of the particles indefinitely follow a path based on their initial position and velocity. While this is the case of a rarefied gas in an infinite vacuum, this is not the behavior in porous media transport. Forces may be exerted on the particles both their gas-gas collisions and gas-solid collisions. In addition, the total number of particles is not, strictly speaking, a constant, as radioactive decay may remove particles from the distribution. Fortunately, unlike some other non-equilibrium phenomena, e.g. evaporative cooling, gas-phase

chemical reactions, or thermalization of neutrons, the likelihood of a particle leaving the distribution by radioactive decay is independent of position and velocity.

In the absence of gas-solid collisions and reaction rates, the gas-gas particle encounters dominate. The most basic model of these encounters is the hard-sphere collision model. In this model, for a force to be exerted, two particles must overlap in time and space. The likelihood of this occurring in space depends upon the diameter of the hard-spheres and their abundances. As laid out by McQuarrie, the gas collision cross section for species i and j is:

$$\sigma_{ij} = \frac{\pi}{4} (d_i + d_j)^2$$

From this, the collisions density of the gas can be found by integrating over all velocities for the distributions of i and j :

$$\iint f_i f_j \sigma_{ij} dv_i dv_j$$

To determine the force exerted by difference species on one another also requires a model for the magnitude of the momentum transferred per collision in addition to the rate of collisions. As only kinetic energy is considered to be transferable, these collisions must be totally elastic, i.e. both kinetic energy and momentum must be conserved by the interaction.

By this, the relative speed of the particles before and collision must be identical in magnitude, though not necessarily in direction. Because the system is in three-dimensional space, the momentum transferred – equivalent to the force exerted in a moment of time – will therefore be dependent on both the magnitude of the relative

velocities and the angle of incidence. If α_{ij} is a function of these angle of incidence, including the effective cross-section, and v_{ij} is the relative velocities, the frequency and magnitude of collision density is then:

$$\iint f_i f_j v_{ij} \alpha_{ij} dv_i dv_j$$

Because of Newton's Third Law, this integral can be used to represent the force on the species i or j . However, without a definition of $f(r, v, t)$, the total derivative cannot yet be integrated over time explicitly. As collisions occur over very short time scales, the change in a distribution due to collisions can be approximated as:

$$f\left(r + v\Delta t, v + \frac{F}{m}\Delta t, t + \Delta t\right) = f'$$

$$\frac{Df}{Dt} \cong \frac{f' - f}{\Delta t} = \iint (f'_i f'_j - f_i f_j) v_{ij} \alpha_{ij} dv_i dv_j$$

For a system in equilibrium, the total derivative must equal zero. Maxwell demonstrated that, for a random system where the relative velocities are nonzero, the distribution must satisfy:

$$f'_i f'_j = f_i f_j$$

Taking the logarithm of each side and requiring the distribution of both i and j to satisfy must independently satisfy:

$$\ln f' = \ln f$$

As the number, momentum, and kinetic energy are conserved, a solution is sought that satisfies these criteria in logarithmic space. Doing so results in the Maxwell-Boltzmann velocity-distribution function:

$$f_i = \frac{c_i}{N_A} \left(\frac{m_i}{2\pi kT} \right)^{3/2} e^{-\frac{m_i v_i^2}{2kT}}$$

This is the distribution that all gases must approach to be in equilibrium. Noticeably absent from this distribution is any dependency upon position. In the absence of external forces, the molar concentration and velocity profile must approach this solution. Deviations from a homogeneous distribution can be expressed as temperature or concentration gradients. For a binary system, as determined by Chapman, this yields the relationship between the gradients and their resulting average velocities (Chapman and Cowling 1970).

$$\bar{v}_j - \bar{v}_i = \frac{N_i}{c_i} - \frac{N_j}{c_j} = -\frac{c^2 D_{ij}}{c_i c_j} (\nabla x_i + k_T \nabla \ln T)$$

The concentration gradient is expressed in terms of mole fraction as, for an isobaric binary system, the gradient of i is equal but opposite to the gradient of j . In doing so, it is apparent, in addition to the concentration gradient, relative molar flux can be induced by the thermal gradient. The term k_T is the thermal diffusivity ratio. As temperature affects the velocity distribution dissimilarly for particles of differing weights, a temperature gradient can induce a concentration gradient. This phenomenon is known by various terms, including the Soret effect, thermodiffusion, or thermophoresis. This phenomenon has been exploited in the isotopic enrichment of gases, for example H^{37}Cl

from H^{35}Cl by Kranz and Watson (Kranz and Watson 1953). However, the temperature gradient in geological media tests is will be small compared with the concentration gradient, minimizing the importance of this effect.

By the Chapman-Enskog method, magnitude of these coefficients, as well as viscosity and conductivity can be estimated by perturbation methods. (Chapman and Cowling 1970). Whereas all of these coefficients are significant in a non-equilibrium system, of primary importance to this work is the mass diffusivity. To the first order approximation, the Chapman-Enskog diffusion coefficient is (Mason and Malinauskas 1983):

$$[D_{ij}]_1 = \frac{3}{8} \sqrt{\frac{\pi kT}{2\mu_{ij}}} \frac{N_A}{c\pi\sigma_{ij}^2\Omega_{ij}}$$

For compactness, the mass of the particles is expressed as the reduced mass μ_{ij} . n is the number density of all gas particles in the system – not exclusively species i or j . Finally, Ω_{ij} is known as the collision integral. As mentioned earlier, the magnitude of the energy transferred is dependent upon the angle on incidence, which is non-trivial for particles that do not act as hard spheres. It is, however, on the order of unity.

In practice, both the collision diameter and collision integral are experimental parameters that depend on the chemical identity of the particles. However, what this definition of the diffusion coefficient does allow is the estimation of the diffusion coefficient at other temperatures and pressures, as well as the development of any number of empirical correlations. Recognizing that the molar concentration can be found from the ideal gas law:

$$\frac{D_{ij}(P, T)}{D_{ij}(P_o, T_o)} = \frac{P_o}{P} \left(\frac{T}{T_o} \right)^{\frac{3}{2}}$$

Furthermore, as the change in electronic structure is minor with changes in neutron number, the diffusion coefficients of isotopes are essentially inversely proportional to the square root of their reduced mass:

$$\frac{D_{ij}}{D_{im}} = \sqrt{\frac{\mu_{im}}{\mu_{ij}}}$$

These diffusivity relationships as well as the ideal gas law, Dalton's law of partial pressures, and the Maxwell-Boltzmann distribution provide the basis for which additional analysis can take place.

2.5. MAXWELL-STEFAN DIFFUSION

To this point, an explicit relationship for the molar flux has only been given in terms of the probability distribution. Integrating the probability distributions of two different species yielded an expression for the relative velocity, but this is limited to the case of a binary mixture. As the concentration and temperature gradient are defined for each species irrespective of all other species, the Maxwell-Stefan (MS) approach seeks to collect the independent terms and express the dependent terms as a summation. The diffusion for a multicomponent mixture is compactly expressed in MS form (Leonardi and Angeli 2010):

$$-\frac{x_i}{RT} \nabla \mu_i = \sum_{j=1, j \neq i}^N \frac{x_j N_i - x_i N_j}{c D_{ij}}$$

Here, μ_i is the chemical potential for the species, which will typically be equal to the molar concentration. The MS approach can be produced from kinetic theory by integrating the weighted velocity distribution of each possible gas pair. If the net molar flux is defined by advective flow, there are $n - 1$ independent equations, where n is the number of species.

2.6. KNUDSEN DIFFUSION AND THE DUSTY GAS MODEL

In the absence of porous media, kinetic theory has provided the Maxwell-Stefan equations that are sufficient to determine the diffusive flux. However, kinetic theory only covered collisions between gas particles, albeit of various types. The only mention of interfacial collisions was in the explanation of the macroscopic pressure, which was defined as the rate of momentum transfer at a solid surface.

The importance of interfacial interactions can be viewed as a balance between the gas-gas collision rates versus the gas-solid collision rate. In the limit of small pore sizes, the surface area of the solid increases very rapidly while gas-gas collision rate is a function of pressure and temperature only. Similarly, gas-solid interactions can become significant in vacuum systems, where the scarcity of gas particles results in very low gas collision densities, despite macroscopic dimensions.

Collisions with the solid phase differ from collisions with gas particles in two significant ways. The first is that the solid phase is composed of an immense number of atoms compared with a singular gas particle. Consequently, the reduced mass of a binary system gas particle i and solid particle K pair is essentially that of the gas species alone.

$$\mu_{iK} = \lim_{\frac{m_K}{m_i} \rightarrow \infty} \frac{m_i m_K}{m_i + m_K} \rightarrow m_i$$

Because of the immense mass, the relative velocity of the pair is essentially that of the gas particle in the reference frame of the solid. In addition, because of the immense mass, the effectiveness of each collision is approximately independent of the angle of incidence.

The second significant difference is in the collision cross section. The number density of the solid particles is immensely smaller than the number density of the gas particles. Countering this is that the interaction cross-section of each particle is now immensely larger than a singular gas molecule. If the pores are approximately cubic, the likelihood of interaction is a product of the number of particles per pore versus the surface area per pore:

$$n_K \pi \sigma_{AK}^2 = \frac{A_K}{V_K} \approx \frac{1}{d_K}$$

Substituting this relationship as well as the reduced mass provides an estimate of the gas-solid diffusion coefficient:

$$[D_{AK}]_1 = \frac{3}{8} \sqrt{\frac{\pi kT}{2\mu_{AK}}} \frac{1}{n\pi\sigma_{AK}^2 \Omega_{AK}} = \frac{3}{8} d_K \sqrt{\frac{\pi kT}{2m_A}}$$

The Knudsen diffusion coefficient is more typically defined using the concept of a mean-free path and the mean thermal velocity. The Knudsen diffusion coefficient is defined in texts, (Welty, et al. 2001) as one-third the product of the pore diameter and the

mean-thermal velocity – which can be obtained by integrating the Maxwell-Boltzmann distribution.

$$D_{AK} = \frac{d_K}{3} \overline{v_A} = \frac{d_K}{3} \sqrt{\frac{8kT}{\pi m_A}}$$

By this method, the relationships with pore diameter, temperate, and mass are identical. The constant parameters vary by approximately 10%. At any rate, the pore diameter at the relevant length scales is difficult to measure at best. In addition, the Knudsen coefficient may not behave ideally if the gas-solid particle interaction deviates from the hard sphere model.

Mason and Malinauskas therefore suggest referring to this diameter as the Knudsen flow parameter that, while dependent upon pore length scales, is not a literal diameter and must be experimentally measured. Here, the diameter notation will be retained but with knowledge it is not a literal measurement. In fact, as porous media is rarely homogeneous, this parameter must represent the average gas-solid interaction for a range of pores.

In either case, in the limit of a rarefied gas relative to pore dimensions, this diffusive process dominates the flow through porous media. When the flow through the media loses its viscous contribution, it is more specifically known as effusion. In this limit, flow increases through the media with pressure, not because of hydrodynamic contributions but because pressure is directly proportional to concentration. The most significant industrial use of this process is the gaseous diffusion method enriching uranium hexafluoride. The following relationship governs fully effusive flow:

$$N_i = -D_{iK} \nabla c_i$$

However, diffusion through porous media is not always fully defined by either Knudsen or binary gas diffusion. The Knudsen diffusion coefficient more accurately represents a minimum contribution to the total diffusivity in a medium. To account for the total diffusive flux in the transition region requires a model that can accommodate interactions with both phases simultaneous.

The primary model capable of this is known as the Dusty Gas Model (DGM). The DGM is a logical extension of the kinetic theory and MS approach. As its name suggest, the solid media is treated as a gas of dust particles. These particles are just one additional component in the MS approach, but with the same two stipulations required of the Knudsen diffusion coefficient: the dust particles have infinite mass and the likelihood of interaction is independent of gas density. The inclusion of dusty gas particles labeled K proceeds as follows:

$$-\frac{x_i}{RT} \nabla \mu_i = \frac{x_K N_i - x_i N_K}{c_{N+K} D_{iK}} + \sum_{j=1, j \neq i}^N \frac{x_j N_i - x_i N_j}{c_{N+K} D_{ij}}$$

The question here is how to treat the mole fraction and molar flux of the dust particles. The system can be normalized such that y_i is the mole fraction of the gas particles – not including the dust – and c_N is the total gas density non-inclusive of the dust:

$$-\frac{x_i}{RT} \nabla \mu_i = \frac{N_i - y_i N_K}{c_N D_{iK}} + \sum_{j=1, j \neq i}^N \frac{y_j N_i - y_i N_j}{c_N D_{ij}}$$

The molar flux of the dust species can then be removed by selecting an appropriate reference frame. As the dust particles have infinite mass compared with the gas particles, solid particles will not be measurably affected by gas particle diffusion. Consequently, the diffusive molar flux with respect to the solid particle reference frame is:

$$J_i = N_i - y_i N_K$$

If the solid particles are in motion, this can be better handled as a change of reference frame for the control volume. Making this substitution yields:

$$-\frac{y_i}{RT} \nabla \mu_i = \frac{J_i}{c_N D_{iK}} + \sum_{j=1, j \neq i}^N \frac{y_j J_i - y_i J_j}{c_N D_{ij}}$$

When limited to an isothermal binary gas system, the resulting matrix can be inverted to determine the diffusive flux in terms of the driving force. As solved for by Thorstenson and Pollock (Thorstenson and Pollock 1989):

$$J_i = -D_{iK} \frac{D_{ij} P \frac{\nabla x_i}{RT} + (D_{ij} + D_{jK}) x_i \frac{\nabla P}{RT}}{D_{ij} + x_i D_{jK} + x_j D_{iK}}$$

In the limit of a dilute tracer in a solvent j :

$$J_i = -D_{iK} \left(\frac{D_{ij}}{D_{ij} + D_{iK}} P \frac{\nabla x_i}{RT} + \frac{D_{ij} + D_{jK}}{D_{ij} + D_{iK}} x_i \frac{\nabla P}{RT} \right)$$

From this, there are two contributions to the diffusive flux, one that is dependent upon the concentration gradient and another that is dependent upon the pressure gradient. From this, it is apparent that, even during advective flows, species with higher or lower Knudsen diffusivities can be enriched in porous media. That is, effusion may take place.

Applying another approximation, isobaric conditions, the expression reduces further. In the limit of large Knudsen coefficients – that is macroscopic pore size – or at high pressure – the dusty-gas model approaches Fick’s Law with the MS diffusion coefficient. However, in the limit of a dilute tracer for an arbitrary pore size, the DGM then approaches:

$$J_i = -D_{iK} \frac{D_{ij} \frac{P}{RT} \nabla x_i}{D_{ij} + D_{iK}} = -\frac{D_{ij} D_{iK}}{D_{ij} + D_{iK}} \nabla c_i$$

This expression also resembles Fick’s Law, but with some correction for the pore dimensions. To illustrate the impact of the DGM on different gases, Figure 2.3 depicts the resulting diffusivity for dilute tracer gases in nitrogen at one atmosphere and 293 K.

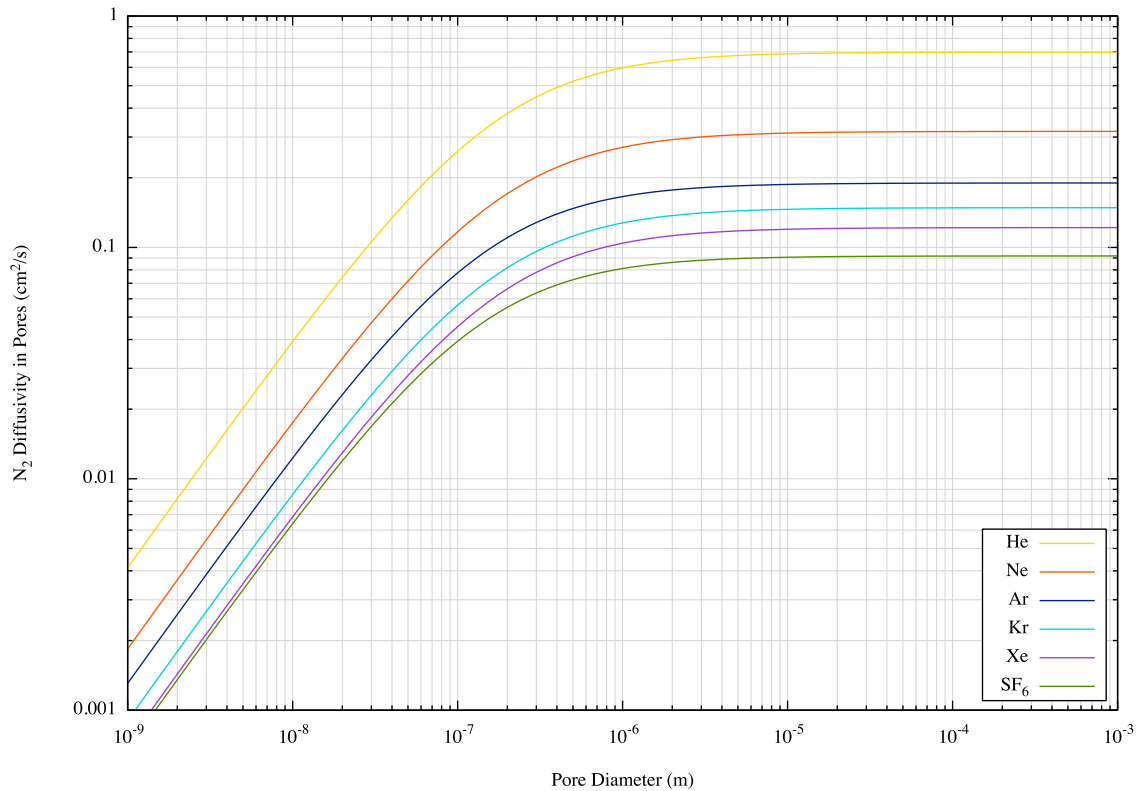


Figure 2.3 Effect of Pore Diameter on Diffusivity in Nitrogen

The most prominent feature in Figure 2.3 is the knee that occurs around $1 \mu\text{m}$. Below 50 nm , the Knudsen diffusivity is the predominant. Conversely, nitrogen collisions dominate above $10 \mu\text{m}$. The location of this knee is dependent upon pressure and temperature, but is not expected to be significantly different in underground geological conditions from the atmospheric conditions depicted here.

While each gas is adversely affected, not all gases are affected the same. This can be viewed as the difference between the reduced mass of the binary gas pair and the gas-solid pair. Because neon and argon have similar molecular weights to nitrogen, the efficiency of their collisions with nitrogen was the greatest. When Knudsen diffusivity comes into play, the efficiency of these collisions is greatly diminished.

In contrast, the heavy gases, particularly sulfur hexafluoride, already had poor efficiency in their collisions with nitrogen. While interactions with the solid phase are still relatively less effective than with nitrogen, the decrease is less severe. Consequently, the gases krypton, xenon, and sulfur hexafluoride are expected to behave more similarly in micropores than they do with nitrogen.

While it has already been stated that the previous form is only valid for a binary mixture of gases, it is approximate to model air as a singular gas species. The primary components of air – nitrogen and oxygen – are both diatomic and have similar molecular weights. Consequently, the reduced mass, collision cross-section, and collision integral are expected to be similar. Of course, a more detailed approach would recognize that, even all nitrogen molecules are not the same. Each isotopologue – a compound that differs only in its isotopic compositions – theoretically has a distinct diffusivity with

every other isotopologue. This approach would be excessively complex, as accurate coefficients for every pair are not well known.

The diffusivity in air can be estimated using the MS approach by weighting each major component by its molar fraction. Coupled with the DGM, the diffusivity of a dilute tracer in a stagnant mixture will then be:

$$\frac{1}{D_i} = \frac{1}{D_{iK}} + \sum_{j \neq i}^n \frac{y_j}{D_{ij}}$$

With an awareness of the assumptions necessary the molar flux of the gas within a pore space will be modeled as:

$$J_i = -D_i \nabla c_i$$

Where D_i represents a Fickian diffusivity. This form is sometimes known as the Bonsaquet Equation (Zalc, Reyes and Iglesia 2004). Assuming that the solid material is in the same reference frame as the control volume, the net molar flux is equal to the diffusive flux. With thoughtful experimental design, the conditions necessary for this approximation are achievable. Clearly, based on the trace quantities of radioxenon expected, the dilute tracer requirement is satisfied in the field. The primary advantage of the assumptions necessary for a Fickian diffusivity is that analytical solutions to the transport equations can be found.

The DGM has so far considered elastic interactions the solid particle surfaces. It is proposed that elastic interactions with liquid phase surfaces follow similar kinetics. While not as tightly bound as solids, liquids are nevertheless very dense and tightly bound compared with the gas phase. Following the same logic of an infinite mass compared

with the gas particles, the gas is indifferent to whether the interfacial surface is solid or liquid. By this reasoning, the presence of an unsaturated liquid phase would manifest itself as a reduction in the effective Knudsen pore diameter. This hypothesis will be tested.

2.7. SORPTION EQUILIBRIA

So far, the DGM has considered elastic collisions with solid and – as a proposal – liquid surfaces. Implicit in this is that the net flux is zero on interfacial surfaces. However, not all collisions are elastic. If a gas particle collides with a liquid phase and enters, it is known as absorption. Similarly, if the gas particle collides with a solid surface and adheres, it is known as adsorption. In either case, gas particles will exit the gas phase, resulting in an interfacial flux. These processes, collectively known as sorption, are also reversible. That is, adsorbed or absorbed quantities of the gas species may return to the gas phase.

In thermodynamic equilibrium, the net interfacial flux is completely balanced and equal to zero. For two phases to be in equilibrium, all of their intensive thermodynamic properties must also be in equilibrium. This includes the temperature, pressure, and chemical potential. While temperature and pressure can be readily controlled and measured, the chemical potential is more problematic. To model the chemical potential, the concept of fugacity is utilized, which is the tendency of a material to flee a phase. For an ideal gas mixture, the fugacity f_i of a gas species is the partial pressure (Smith, Van Ness and Abbott 2001).

$$f_i^g = y_i P = p_i$$

At the pressures and temperatures of concern for geological transport, significant deviations from ideal gas behavior are not expected. However, the fugacity of the condensed phase is not as easily defined. Fortunately, Henry's Law can approximate the fugacity in the limit of a dilute solution:

$$\mathcal{H}_i \equiv \lim_{x_i \rightarrow 0} \frac{f_i}{x_i}$$

The value of the Henry's law coefficient is dependent on the chemical identity of the solute and solvent, as well as temperature and pressure. As the gas phase concentration of our tracer species will be small, the adsorbed or absorbed phase is not expected to deviate from Henry's law. By equating the fugacity of the two phases, the equilibrium concentrations can be found:

$$f_i^a = f_i^l = f_i^g = y_i P = \mathcal{H}_i^l x_i^l = \mathcal{H}_i^a x_i^a$$

In the case of absorption, the Henry's Law coefficients are readily available from IUPAC solubility data series references: (Clever, Argon: IUPAC Solubility Data Series 1980) (Clever, Helium and Neon: IUPAC Solubility Data Series 1979) (Clever, IUPAC-NIST Solubility Data Series. 80. Gaseous Fluorides of Boron, Nitrogen, Sulfur, Carbon, and Silicon and Solid Xenon Fluorides in all Solvents 2005) (Clever, Krypton, Xenon and Radon: IUPAC Gas Solubility Data Series 1979). Rather than being defined in Henry's Law form, which are dependent on the units of measurement, these references provide the equilibrium relationship as mole fraction solubility:

$$X_i = \frac{x_i}{y_i} = \frac{P}{\mathcal{H}_i}$$

Therefore, mole fraction solubility is inversely proportional to Henry's Law without the dependency on the equation of state for either fluid phase. However, care should be taken when consulting other references as Henry's Law coefficients are tabulated in a variety of inconsistent ways. Figure 2.4 depicts the mole fraction solubility of the noble gases and saturated fluorides in water over a range of temperatures:

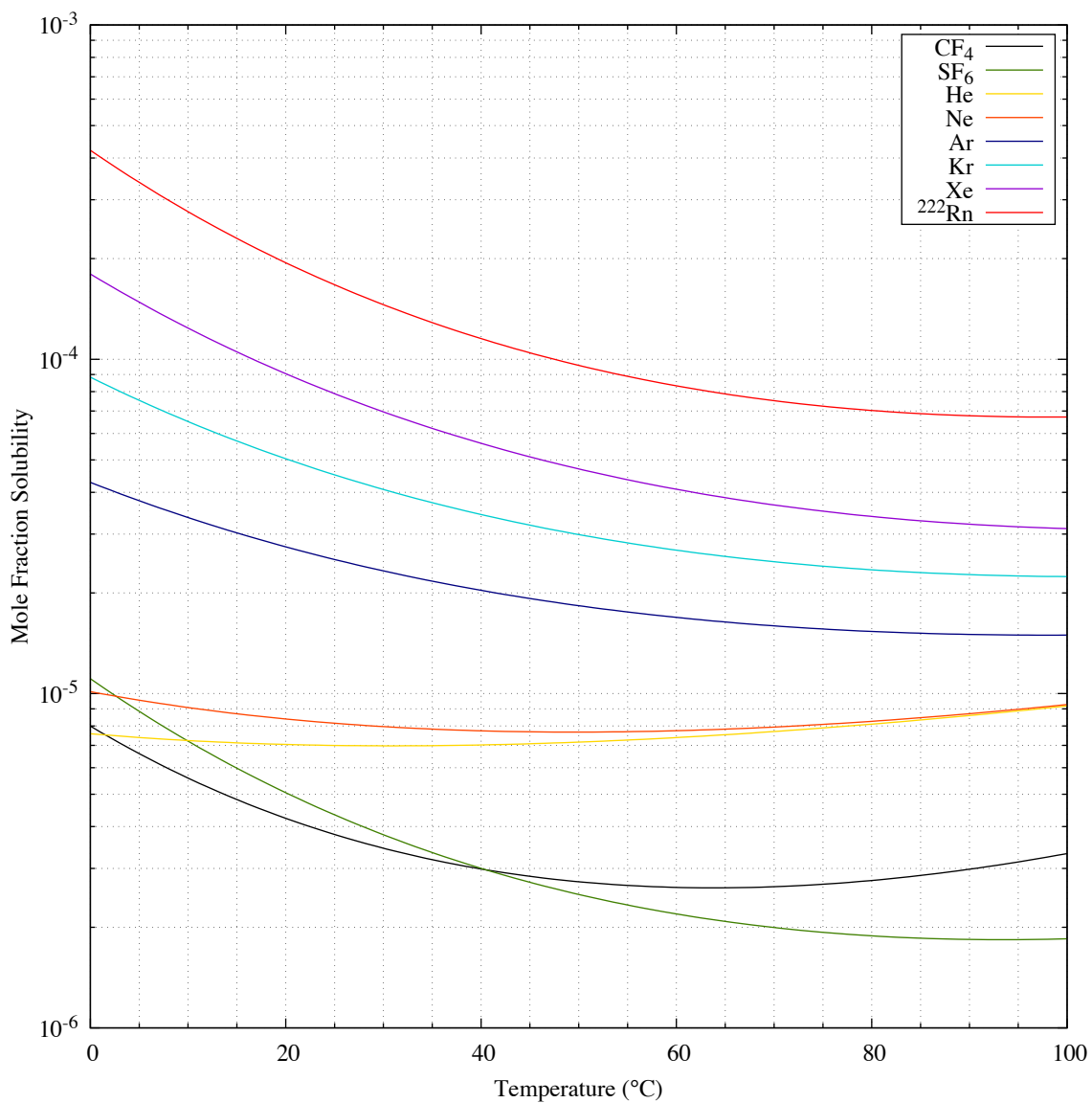


Figure 2.4 Solubility of Saturated Fluoride and Noble Gases in Liquid Water

One trend is immediately clear, the heavier noble gases are far more soluble than the lighter noble gases. However, the saturated fluorides both have minor solubility in comparison despite being similar in mass to xenon and krypton. Molecular weight alone cannot explain this trend.

In addition to increasing in molecular weight, the number of electrons also increases. Because of the Pauli exclusion principle, these electrons cannot be in the same quantum orbitals. This has two consequences. First, the outermost electrons are in higher principal quantum number states and are, on average, further from the nucleus. Secondly, with each increasing period, a growing number of electrons lie between the outermost shell and the nucleus, counteracting the positive nuclear charge with dispersed negative electronic charge. The net effect is that the outermost electrons reside in a much-diminished electric field despite the increased nuclear charge. Because of the reduced effective electric field, the outermost electrons are less tightly bound and the polarizability of the noble gases increases with each period. Because water has a strong permanent dipole, the strength of the intermolecular forces increases with polarizability, resulting in higher solubility (Israelachvili 2011).

In contrast, the polarizability of carbon tetrafluoride and sulfur tetrafluoride are limited by their symmetry. With tetrahedral and octahedral symmetry, the ordinarily polarized carbon/sulfur to fluorine bonds are perfectly balanced, resulting in no net permanent dipole. Because of this, like the noble gases, they are found in the gas phase at ambient temperatures and pressures, despite their relatively large molecular weights.

However, carbon and fluorine reside in the second period, with sulfur in the third period. These electrons are tightly bound – comparable to neon – and are less susceptible to induced dipole moments. Finally, both fluorides are large in volume compared with a singular noble gas atom. As larger molecules disrupt the liquid phase more significantly, they are more difficult to solvate.

The same intermolecular force arguments apply to surface adsorption of a gas. Numerous adsorption isotherm models are available, however, as the limit the surface coverage is small compared with the number of available sites, Henry's Law is similarly applicable. As the noble gases interact with the surface through dispersion forces, also known as physisorption, the number of sites is immense. Figure 2.5, taken from Fanale and Cannon, demonstrates the linearity of Krypton and Xenon adsorption even at partial pressures of 100 torr onto shale.

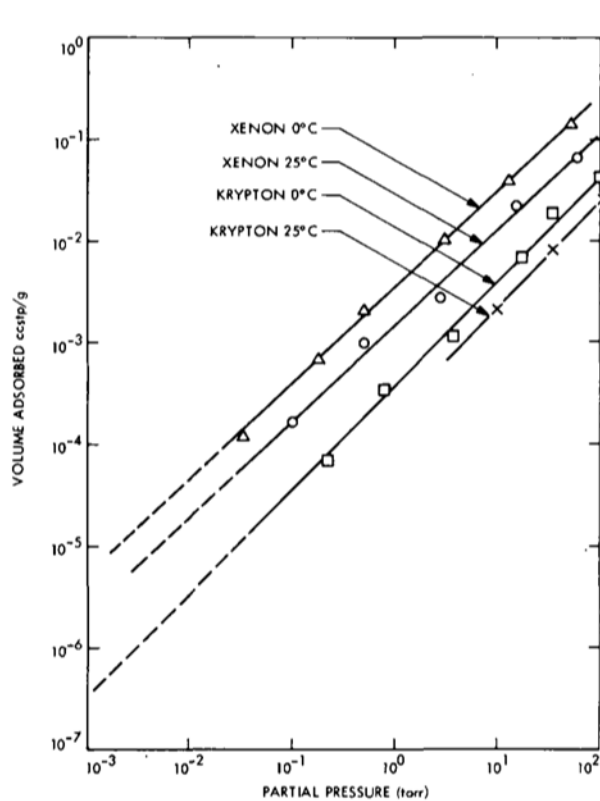


Figure 2.5 Kr and Xe Adsorption on Shale (Fanale and Cannon 1971)

Unlike the gas and liquid phases, the adsorbed phase has an immeasurably small volume. While it can be expressed as an areal concentration, measuring this is also laborious. Instead, the surface area is presumed to be a proportional to the quantity of the

sorbent expressed as mass, the proportionality of which is encompassed by the isotherm. Therefore, the adsorbed phase gravimetric concentration a_i is related to the gas phase partial pressure by:

$$a_i = K_i p_i = K_i c_{i,g} \frac{RT}{P}$$

As the Henry's Law isotherm is valid in the limit of low concentrations, measurements of adsorption obtained at higher pressures can be used to approximate adsorption at trace concentrations relevant to both this work and UNEs.

Also as depicted in Figure 2.5, adsorption is stronger for xenon than krypton. This is consistent with the increased polarizability over xenon over krypton by virtue of its larger atomic radius and number of electrons. The linearity out to 100 torr supports the physisorption model – that is, surface sites are not limiting. Consequently, this effect is expected to be universal to all porous media, though the gravimetric concentration will vary with the specific surface area of the substrate. As the quantity of experimental data on xenon adsorption on geological materials is very limited, additional data is necessary to confirm the magnitude of this effect on alternative materials.

2.8. SORPTION KINETICS

Of course, the previously discussed equilibrium relationships require equilibrium. As the gas phase is known to be non-uniform, this cannot strictly be true. However, provided the kinetics of adsorption occur on a time scale much faster than the gas phase transport, this is approximately true.

First, the rate of adsorption onto a surface is presumed to be proportional to the rate of collisions striking the surface. Since the rate of collisions with the surface is proportional to partial pressure, the expression for adsorption rate is assumed to be of the form:

$$N_a = k_a p_i$$

As only particles moving slowly enough will be captured by the surface, the constant k_a decreases with increasing temperature.

Conversely, the likelihood of a particle adsorbed to the surface having sufficient energy from gas of solid phase transfer is assumed to be proportional to the surface concentration.

$$N_d = k_d a_i$$

In this case, the desorption constant would increase with increasing temperature. The net flux of the gas between the gas and solid surface must then be:

$$N_{i,ad} = N_a - N_d = k_a p_i - k_d a_i$$

In general, these rate constants are not measurable directly. However, at equilibrium, it is known that the net flux must be zero. Combining this expression with Henry's Law confirms

$$K_i = \frac{k_a}{k_d} = \frac{a_i}{p_i}$$

There are other isotherms that will not follow the kinetics laid out here, but as references indicate the validity of Henry's Law for trace noble gases undergoing adsorption, they are omitted.

In addition, there is the possibility of both advective and diffusion motion within the adsorbed layers. The adsorbed gas layer follows much of the same properties of the three dimensional gas, but in two dimensions (Myers and Prausnitz 1965). However, the relative magnitude of its importance is limited to the magnitude line integrals on adjacent control surfaces, much as gas transport is limited by the surface integrals of flux on adjacent control volumes. Thereby, these effects are of little importance unless the media is fully in Knudsen flow and gas-gas surface area is negligible.

2.9. ABSORPTION KINETICS AND TRANSPORT

The kinetics of absorption at the surface of the liquid phase are completely analogous to adsorption kinetics. Because the aqueous solutions of noble gases also obey Henry's Law under relevant conditions, the flux between the gas and liquid phases must be:

$$N_{i,ab} = k_a p_i - k_d c_{i,l}$$

However, as the solubility is expressed as in terms of mole fraction, a few adjustments are necessary to determine the liquid phase concentration in volumetric terms. First, the mole fraction in the gas phase is calculated as the molar concentration of the species divided by the total molar concentration of the gas.

$$y_i = c_{i,g} \frac{RT}{P}$$

The molar volumetric concentration of the species in the liquid can similarly be found by dividing the mole fraction in the liquid by the total molar concentration of the solvent; as the mole fraction solubility is well below parts per thousand, this is sufficiently accurate. The molar density of the solvent can be found by dividing the mass density by the molecular weight:

$$c_{i,l} = x_i \frac{\rho_l}{m_l}$$

Combining with the definition of the mole fraction solubility provides the following relation between the gas and liquid phase molar concentrations:

$$c_{i,l} = X_i \frac{RT}{P} \frac{\rho_l}{m_l} c_{i,g}$$

Complicating matters is that only a small fraction of the total liquid volume is on the surface of the liquid. To access the inner regions of a liquid filled pore, an adsorbed molecule must diffuse through the liquid medium. Whether or not the inner volume is accessible to the tracer gas depends upon the gas-liquid surface area, pore depth, and liquid diffusivity.

In the absence of advective flows, diffusion processes dominate the gas-liquid mass transfer. To conserve material, the mass fluxes must be balanced at the interface. Therefore:

$$-D_g \nabla c_g = N_g = -N_l = -D_l \nabla c_l$$

However, because gas phase diffusivity is orders of magnitude greater than liquid phase diffusivity, the concentration gradient in the gas phase is negligible compared with

the liquid phase and can be modeled as a constant boundary condition. The mass transfer is thus liquid-flux limited.

On a microscopic level – that is omitting porous media obstructions – the material balance results in Fick's Second Law within the liquid:

$$\frac{\partial c_{i,l}}{\partial t} = D_{iL} \nabla^2 c_{i,l}$$

Applying the boundary condition that the liquid phase concentration at the interface is in equilibrium with the gas phase according to the mole fraction solubility X_i :

$$c_{i,l}(x = 0) = X_i \frac{RT}{P} \frac{\rho_l}{m_l} c_{i,g}$$

The second boundary condition is the zero flux condition between the liquid phase and the solid phase. Strictly speaking, it is possible for an adsorbed layer to form on the surface of the solid in the liquid phase. However, this possibility will be handled by another means.

The steady state solution must be the equilibrium concentration throughout. However, the important feature is the transient response. As the exact pore dimensions are not known, the pores are assumed to be approximately rectilinear with a pore dimension comparable to the Knudsen pore diameter. Given these criteria, the transient response must be of the form:

$$c_{i,l}(x, t) = X_i \frac{RT}{P} \frac{\rho_l}{m_l} c_{i,g} \left(1 - \sum_{n=0}^{\infty} a_n e^{-\frac{(2n+1)^2 \pi^2}{4d_k^2} D_{iL} t} \sin\left(\frac{(2n+1)\pi}{2L} x\right) \right)$$

While the coefficients to the transient series can be found by performing eigenfunction expansion on the initial conditions, the initial conditions are neither known

nor necessary here. The important factor is the transient response time. Selecting the slowest moving eigenvalue, the pores will respond on a time scale of τ :

$$\tau = \frac{4d_K^2}{\pi^2 D_{iL}}$$

From the work of Wise and Houghton, it is estimated the diffusivity of xenon in 20°C water is $0.6 \times 10^{-5} \text{ cm}^2/\text{s}$ (Wise and Houghton 1968). Assuming that the capillary pores are approximately one millimeter, the largest eigenvalue is approximately 675 seconds or 0.18 hour. While this is not always negligible, it is dramatically faster than both radioactive decay and gas transport to the surface. Similarly, if on a laboratory scale, the response of the system is much slower than 675 seconds, the absorption process into the capillary pores can be assumed to rapid with changes in gas phase concentration.

2.10. COMBINED THREE-PHASE MODEL

So far, from kinetic theory and the dusty gas model, equations representing the gas phase concentration and gas-gas interfacial flux have been derived. Restricting the model to the vadose zone, in the absence of percolating liquid, the liquid-liquid interfacial flux is zero. By selecting the frame of reference to be that of the solid phase, the solid-solid interfacial flux is similarly zero.

Henry's Law isotherms have related the solid and liquid phase concentrations to the gas phase concentration through partial pressure at equilibrium. While exact representations of the gas-liquid and gas-solid fluxes have not been found, To conserve material, the surface integral of the gas phase onto the liquid or solid phases must be

equal and oppose to the surface integral of the liquid or solid phases receiving the material. While exact values of the adsorption and desorption rates are not known, they must be commensurate

Finally, while the liquid-solid flux has not been discussed in great detail, it is assumed to be equivalent to the gas-solid flux. Despite the solid surface being coated with the liquid phase, Henry's Law may very well still be accurate because the gas phase concentration is exceedingly low. As the fugacity of all three phases must be identical at equilibrium, the surface area of the solid phase to the gas phase will not be truncated by the degree of saturation.

With expressions for the molar flux on all intra- and inter-facial surfaces, and equilibria relations between the adsorbed, aqueous, and gaseous phases, the control volume model can be completed. Representing the gaseous phase:

$$\begin{aligned} \frac{\partial}{\partial t} \int_{\varepsilon(1-S)V} c_{i,g} dV \\ = - \int_{\varepsilon(1-S)V} N_{i,gg} \cdot dA - \int_{\varepsilon SV} N_{i,gl} \cdot dA - \int_{(1-\varepsilon)V} N_{i,gs} \cdot dA + \int_{\varepsilon(1-S)V} r_i(c_{i,g})dV \end{aligned}$$

And the liquid phase, presuming there is stagnant liquid-liquid surfaces:

$$\frac{\partial}{\partial t} \int_{\varepsilon SV} c_{i,l} dV = - \int_{\varepsilon SV} N_{i,lg} \cdot dA + \int_{\varepsilon SV} r_i dV$$

The solid phase balance will now be modified to use the gravimetric concentration. It will be assumed there is negligible solid-solid advective transport or

interfacial connectivity such that surface diffusion and spreading pressure can be neglected.

$$\frac{\partial}{\partial t} \int_{(1-\varepsilon)V} \rho_s a_i dV = - \int_{(1-\varepsilon)V} N_{i,gs} \cdot dA + \int_{(1-\varepsilon)V} r_i dV$$

Summing the material balance of the three phases together:

$$\frac{\partial}{\partial t} \left(\int_{\varepsilon(1-S)V} c_{i,g} dV + \int_{\varepsilon SV} c_{i,l} dV + \int_{(1-\varepsilon)V} \rho_s a_i dV \right) =$$

In doing so, all but the gas-gas interface surface integrals factor out. Acknowledging there are three distinct phases located in three distinct regions, the molar concentration can be thought of as a piecewise function, appearing as expected within the appropriate region, and zero elsewhere. Doing so allows the volume integral to be performed over the entire REV, with each phase weighted appropriately by the porosity and saturation.

$$\begin{aligned} & \frac{\partial}{\partial t} \left(\int_V (\varepsilon(1-S)c_{i,g} + \varepsilon S c_{i,l} + (1-\varepsilon)\rho_s a_i) dV \right) = \\ & - \oint_V \varepsilon(1-S) N_{i,gg} \cdot dA + \int_V r_i \left((1-S)c_{i,g} + \varepsilon S c_{i,l} + (1-\varepsilon)\rho_s a_i \right) dV \end{aligned}$$

Doing so allows the surface integral to also be performed over the entire REV. This closes the surface, allowing it to be converted to a volume integral through the divergence theorem.

$$\frac{\partial}{\partial t} \left(\int_V (\varepsilon(1-S)c_{i,g} + \varepsilon S c_{i,l} + (1-\varepsilon)\rho_s a_i) dV \right) =$$

$$- \int_V \nabla \cdot \varepsilon(1-S)N_{i,gg} dV + \int_V r_i \left((1-S)c_{i,g} + \varepsilon S c_{i,l} + (1-\varepsilon)\rho_s a_i \right) dV$$

While this form is adequate for finite volume methods, it is more convenient analytically by differentiating by volume.

$$\frac{\partial}{\partial t} (\varepsilon(1-S)c_{i,g} + \varepsilon S c_{i,l} + (1-\varepsilon)\rho_s a_i) =$$

$$-\nabla \cdot \varepsilon(1-S)N_{i,gg} + r_i (\varepsilon(1-S)c_{i,g} + \varepsilon S c_{i,l} + (1-\varepsilon)\rho_s a_i)$$

Applying the Henry's Law relationships, the liquid and adsorbed phase concentrations will be expressed as a function of the gas phase concentration. As the gas phase concentration is of primary importance, the subscript will be dropped after dividing through by the gas phase fractional volume:

$$c_i = (1-S)c_{i,g}$$

So that:

$$\frac{\partial}{\partial t} \left(1 + \frac{RT}{P(1-S)} \left(S X_i \frac{\rho_l}{m_l} + \left(\frac{1}{\varepsilon} - 1 \right) \rho_s K_i \right) \right) c_i =$$

$$-\nabla \cdot N_i + r_i \left(1 + \frac{RT}{P(1-S)} \left(S X_i \frac{\rho_l}{m_l} + \left(\frac{1}{\varepsilon} - 1 \right) \rho_s K_i \right) \right)$$

Of course, this substitution cannot be made for saturated media, as the gas phase contribution is zero. The coefficient of the gas phase concentration is, by one convention, known as the retardation factor. This terminology was adapted as it retards the

breakthrough of a tracer curve in advective transport (Bear 1972). Following the convention of Bear, the retardation factor R_d would be:

$$R_f = 1 + \frac{RT}{P(1-S)} \left(SX_i \frac{\rho_l}{m_l} + \left(\frac{1}{\varepsilon} - 1 \right) \rho_s K_i \right)$$

However, in other texts, the symbol R is used as the ratio of the stationary phase to the mobile phase (Crank 1975), providing no terminology for the symbol. In the Crank notation:

$$R_c = \frac{RT}{P(1-S)} \left(SX_i \frac{\rho_l}{m_l} + \left(\frac{1}{\varepsilon} - 1 \right) \rho_s K_i \right)$$

Finally, a similar concept is applied to in chromatography. According to IUPAC (Ettre 1993), the retention factor is designated to be the stationary phase fraction over the mobile phase. The retention factor is consistent with the nameless ratio introduced by Crank. Additional terms have been used in similar areas, including partition ratio, capacity ratio, capacity factor, and mass distribution ratio. Confusingly, IUPAC also defines the retardation factor as the retarded distance traveled by a species versus the solvent. As the retarded distance is inversely proportional to the retarded arrival time, this definition is the reciprocal of the retardation factor mentioned by Bear and other geological contexts.

Consequently, as the retardation factor is not accurate terminology in all contexts, it shall not be used. Of these terminologies, the most apropos and useful in this context is the volumetric capacity factor, κ . Here, it will be defined as the total apparent volume of the species divided by the gas phase volume of the species:

$$\kappa_i = 1 + \frac{RT}{P(1-S)} \left(SX_i \frac{\rho_l}{m_l} + \left(\frac{1}{\varepsilon} - 1 \right) \rho_s K_i \right)$$

The mathematical definition is identical to the definition of retardation factor provided by Bear, but removes the contradictory connotations of either a retarded arrival time or retarded position.

Of course, the importance of this factor depends on its magnitude. There is insufficient data to draw conclusions on the adsorption contribution at this time, but the capacity factor as a function of water saturation can be readily calculated. Figure 2.6 shows this contribution at atmospheric pressure and at 0°C and 20°C.

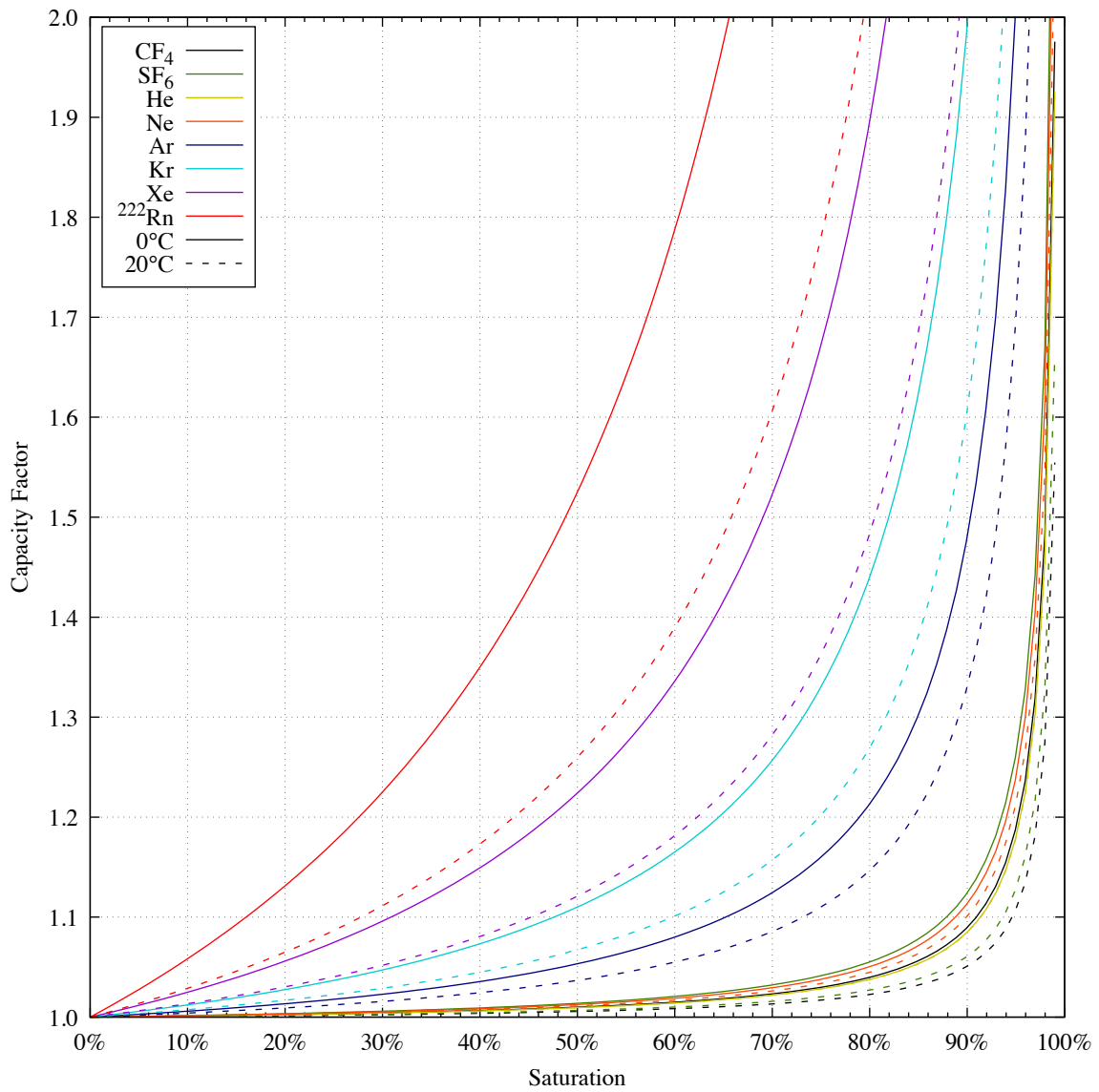


Figure 2.6 Capacity Factor vs. Water Saturation

For the heavier noble gases, Kr, Xe, and Rn, the capacity factor begins to become significant at 50% saturation or less. In contrast, the light noble gases, He and Ne, and the saturated fluorides, CF₄ and SF₆, do not have an appreciable contribution until nearly 90% saturation. At 90% saturation, the connectivity of the remaining pores is suspect and

gas transport will be greatly disrupted. Therefore, they are effectively insoluble for purposes of modeling gas transport in the vadose zone.

As will be shown, the primary effect in diffusive transport is the increase in apparent volume over pore volume, which has secondary effect of increasing the transport rate. This is the reverse phenomenon as encountered in advective transport. Choosing this terminology reduces the material balance to:

$$\frac{\partial}{\partial t} \kappa_i c_i = -\nabla \cdot N_i + r_i(\kappa_i c_i)$$

An expression for the molar flux must then be substituted. Recalling the isothermal and isobaric conditions for a dilute tracer, the molar flux of a species was defined as:

$$N_i = -D_i \nabla c_{i,g}$$

Before making the substitution directly, it must be acknowledged that this model was developed for the coordinate system within a pore space. As the pores are not parallel to REV coordinates, they are not orthogonal. Consequently, from the perspective of the REV, the tortuosity reduces the magnitude of the gradient. Written in orthogonal coordinates:

$$N_i = -\frac{1}{q} D_i \nabla c_i$$

However, when evaluating the divergence, the dot product of the molar flux and interfacial area must be taken. As only the gas phase volumes contribute, the divergence must be reduced by the porosity and saturation. In addition, as the second derivative must

then be taken in space, the tortuosity factor must be applied a second time. The divergence of the gas-phase flux in REV space is thereby:

$$\nabla \cdot N_i = -\frac{\varepsilon(1-S)}{q^2} D_i \nabla^2 c_i$$

Because the diffusivity in the pores adjusted for the REV space is ubiquitous, it will be referred to as the effective diffusivity, \mathfrak{D}_i , throughout this text.

$$\mathfrak{D}_i = \frac{\varepsilon(1-S)}{q^2} D_i$$

In terms of the effective diffusivity and volumetric capacity, the material balance is now:

$$\frac{\partial}{\partial t} \kappa_i c_i = \mathfrak{D}_i \nabla^2 c_i + r_i(\kappa_i c_i)$$

Finally, returning to the radioactive decay term. For a singular species, it is clear that the total quantity of the species is proportional to the gas phase concentration times its capacity factor. This can be extended to all species:

$$\frac{\partial}{\partial t} \kappa_i c_i = \mathfrak{D}_i \nabla^2 c_i - \lambda_i \kappa_i c_i + \sum_{j \neq i}^N f_{i,j} \lambda_j \kappa_j c_j$$

As there may be radioactive decay into or out of the balance of a species, there are N coupled inhomogeneous equations for N radioactive species. As neither laboratory nor field experiments have utilized species within decay chains, the inhomogeneous terms will be dropped from further discussion. In addition, as isothermal and isobaric conditions have already been specified, the capacity factor will be constant with time. Dividing throughout by the capacity factor:

$$\frac{\partial c_i}{\partial t} = \frac{\mathfrak{D}_i}{\kappa_i} \nabla^2 c_i - \lambda_i c_i$$

This is the reactive-diffusive transport equation for gas transport for stagnant adsorbed and absorbed phases. The porosity and tortuosity are dependent only on the media, though diffusivity, capacity, and reactivity are dependent on the chemical species.

2.11. DOUBLE POROSITY MODEL AND THE FRACTURE-MATRIX INTERFACE

The reactive-diffusive equation as constructed relies on the smoothly varying porosity, tortuosity and saturation. As is often the case, the geological media may have discontinuous fractures surrounded by a relatively uniform matrix of porous media. In the absence of the porous media, the advective-diffusive model (ADM) is sufficient. This model simply states that the total molar flux of a species is the summation of the advective and diffusive components.

The advective component is simply the molar concentration carried by the bulk velocity v . In general, the diffusive component should be found using the MS approach for a multicomponent mixture. However, in the limit of a dilute tracer, the diffusive flux is approximately Fickian:

$$N_i = J_i + c_i v = -D_i \nabla c_i + c_i v$$

Combining the ADM with the material balance yields the advective-diffusive-reactive equation:

$$\frac{\partial c_i}{\partial t} = D_i \nabla^2 c_i - \nabla \cdot (c_i v) - \lambda_i c_i + \sum_{j \neq i}^N f_{i,j} \lambda_j c_j$$

As shown by Lowrey, advective transport induced by barometric pumping is the dominant form of transport within the fractures and also has significant effects within the matrix (Lowrey 2013). Because porosity, tortuosity, and sorption are not as significant in the fracture, the efficacy of transport is much greater in this region.

The double-porosity model is significant to this research as it designates the boundary conditions for which to solve the reactive-diffusive equation within the matrix. At the fracture-matrix interface, to conserve material, the inner product of the flux and interfacial areas must be equal from each perspective:

$$N_{i,f} \cdot A_f = N_{i,m} \cdot A_m$$

Assuming an isotropic media, the fracture or matrix areal density is the total areal density multiplied by the corresponding porosity. Because the porosity in the fracture is nearly unity, the areal density in the fracture is effectively the total areal density. For simplicity, the advective component of the fracture into the matrix will also be neglected. Having already discussed the effect of tortuosity in the context of the REV, the flux into the matrix from the fractures perspective must then be:

$$-D_i \nabla c_{i,f} = -\frac{\varepsilon(1-S)}{q} D_i \nabla c_{i,m}$$

The combined effect of the porosity, tortuosity, and saturation reduce the impact of the concentration gradient; consequently, the concentration gradient in the matrix must be far steeper than in the fracture. To a first approximation, the concentration gradient normal to the interface is zero. Therefore, the boundary condition at the fracture-matrix

interface is approximately that of a fixed concentration. In mathematical parlance, this is a Dirichlet boundary condition.

An analogous approximation will be made for laboratory scale diffusion tests. At the interface of regions packed and devoid of porous media, the boundary condition will be approximately the fixed concentration of the voided region.

2.12. PERIODIC OR IMPERMEABLE BOUNDARIES

A second boundary condition is necessary to solve the differential equation as it second order with respect to position. For two fractures separated by a porous medium, it is possible to solve for the concentration profile using two Dirichlet boundary conditions. However, it can be shown that for two periodically spaced fractures of similar concentration, there must be a point between them where the concentration gradient equals zero.

A second scenario where the concentration gradient may approach zero is when the matrix intersects either an impermeable or saturated media – for example, the water table. In this case, the effective diffusivity into this third region is minimal compared with the diffusivity in the matrix. In the same manner by which the fracture concentration gradient normal to the matrix was assumed to be zero, the matrix concentration gradient in the vicinity of the impermeable boundary is also zero. Boundary conditions of this type are known as Neumann conditions. Because of the dual utility of the Neumann condition for periodic and impermeable boundaries, this solution will be discussed at length.

2.13. INITIAL AND TIME-VARYING BOUNDARY CONDITIONS

For the purposes of this research, the initial condition will be presumed to be negligible tracer species in the matrix prior to exposure. While time varying boundary conditions are certainly expected in a UNE event – i.e. delayed radionuclide sources and advective transport will appear as time-varying boundary conditions to the matrix. However, provided with an adequate model for matrix transport, the response to time-varying boundary conditions can be systematics found through application of Duhamel’s principle.

2.14. DIFFUSIVE TRANSPORT OF A STABLE TRACER IN A FINITE MATRIX

In the absence of radioactive decay – or where the radioactive decay occurs on a timescale where it is irrelevant such as for ^{85}Kr – transport within the matrix is governed by:

$$\frac{\partial c_i}{\partial t} = \frac{\mathcal{D}_i}{\kappa_i} \nabla^2 c_i$$

While this equation can be solved for a variety of geometries, most significantly planar, cylindrical, and spherical, here and throughout this work, planar geometry will be assumed for the fractures. Thereby, the derivatives in all but the x -direction are presumed to be zero. By the previous discussion of the double-porosity model and periodic/impermeable boundaries, the solution is subjected to the boundary conditions:

$$c_i(0, t) = c_0$$

$$\left. \frac{\partial c_i}{\partial x} \right|_{x=L} = 0$$

While solvable in this form, it is pragmatic to put the equation into non-dimensional form. To do so, the logical choice is to scale the position by the distance to the no-flux boundary:

$$\chi = \frac{x}{L}$$

After accounting for this, the equation and time can be made non-dimensional by substituting the dimensional time with the Fourier modulus:

$$Fo = \frac{\mathfrak{D}_i}{\kappa_i} \frac{t}{L^2}$$

Performing these substitutions yields the normalized equation and boundary conditions:

$$\frac{\partial c_i}{\partial Fo} = \frac{\partial^2 c_i}{\partial \chi^2}$$

$$c_i(0, Fo) = c_0$$

$$\left. \frac{\partial c_i}{\partial \chi} \right|_{\chi=1} = 0$$

The solution to this system is routine. Assuming an equilibrium solution equal to the fixed boundary concentration throughout the matrix can satisfy the inhomogeneous boundary condition. The resulting homogeneous equation can be solved by separation of variables, which results in the Fourier series of eigenfunctions. Applying the homogeneous boundary conditions necessitates the cosine component to have zero coefficients while the sine component is restricted to wavenumbers where:

$$k_n = \frac{(2n + 1)\pi}{2}$$

Using the orthogonality of the Fourier series to expand the transformed initial condition results in the complete solution:

$$c(\chi, Fo) = c_0 \left(1 - 2 \sum_{n=0}^{\infty} \frac{\sin(k_n \chi)}{k_n} e^{-k_n^2 Fo} \right)$$

In dimensional coordinates, the solution is:

$$c(x, t) = c_0 \left(1 - 2 \sum_{n=0}^{\infty} \frac{\sin\left(k_n \frac{x}{L}\right)}{k_n} e^{-k_n^2 \frac{\mathcal{D}_i}{\kappa_i} \frac{t}{L^2}} \right)$$

2.15. DIFFUSIVE TRANSPORT OF A REACTIVE TRACER IN A MATRIX

In contrast, where radioactive decay is non-negligible, the reactive-diffusive equation can be made non-dimensional in the absence of extensive parameters. Defining the diffusive decay length as:

$$L_\lambda = \sqrt{\frac{\mathcal{D}_i}{\kappa_i \lambda_i}}$$

Applying this as the characteristic length in place of the distance to the no-flux boundary yields the following non-dimensional length ξ and time τ :

$$\xi = \frac{x}{L_\lambda} = x \sqrt{\frac{\kappa_i \lambda_i}{\mathcal{D}_i}}$$

$$\tau = \lambda_i t$$

Doing so places the differential equation in a non-dimensional form:

$$\frac{\partial c_i}{\partial \tau} = \frac{\partial^2 c_i}{\partial \xi^2} - c_i$$

As opposed to the stable tracer solution method, the no-flux boundary solution is now located at a variable position:

$$\phi = \frac{L}{L_\lambda} = L \sqrt{\frac{\kappa_i \lambda_i}{\mathcal{D}_i}}$$

This quantity represents the ratio of reaction rate to diffusion rate. Consequently, this quantity is analogous to the Thiele Modulus applicable to catalytic activity in porous media (Thiele 1939). The resulting normalized boundary conditions are:

$$c_i(0, \tau) = c_0$$

$$\left. \frac{\partial c_i}{\partial \xi} \right|_{x=\pm\phi} = 0$$

For mathematical reasons, the solution is assumed to be symmetric. If it is not, the solution in the negative coordinate space can be disregarded. As with the stable tracer solution, the solution to the reactive transport will be assumed to have two components, a steady-state contribution that satisfies the inhomogeneous boundary condition and the transient response to the modified initial conditions. The steady-state contribution on a finite domain can be found to be:

$$c_i(\xi) = c_0(\cosh |\xi| - \tanh(\phi) \sinh |\xi|)$$

From this, it is evident that the steady-state concentration profile varies with the Thiele Modulus. However, the hyperbolic tangent rapidly approaches unity at a Thiele Modulus of approximately two. Consequently, for moderate values of ϕ over two, the steady state concentration profile reduces to:

$$c_i(\xi) = c_0 e^{-|\xi|}$$

From this, it is evident that, after a few decay lengths, the concentration is approximately zero. Rather than strictly enforcing the no-flux condition at ϕ , it is more pragmatic to apply the infinite boundary conditions. The unsteady contribution to the reactive-diffusive system is then subject to the following homogeneous boundary conditions, albeit with a complex transformed initial condition:

$$\frac{\partial c_i}{\partial \tau} = \frac{\partial^2 c_i}{\partial \xi^2} - c_i$$

$$\lim_{\xi \rightarrow \pm\infty} c_i(\xi, \tau) \rightarrow 0$$

$$c_i(\xi, 0) = -c_0 e^{-|\xi|}$$

In the infinite domain, the solution is efficiently found through the use of Fourier integral transforms. As there are multiple conventions used, the Fourier transform used here will be defined:

$$\mathcal{F}_\xi[f(\xi, \tau)] = F(\omega, \tau) = \frac{1}{\sqrt{2\pi}} \int_{-\infty}^{\infty} f(\xi, \tau) e^{-i\omega\xi} d\xi$$

Applying this transform to the partial differential equation results in the ordinary differential equation:

$$\frac{dF}{d\tau} = -(\omega^2 + 1)F$$

The solution to this equation is readily found to be:

$$F(\omega, \tau) = F(\omega, 0) e^{-(\omega^2 + 1)\tau}$$

Where:

$$F(\omega, 0) = \frac{1}{\sqrt{2\pi}} \int_{-\infty}^{\infty} e^{-|\xi|} e^{-i\omega\xi} d\xi = \sqrt{\frac{2}{\pi}} \frac{1}{1 + \omega^2}$$

The resulting solution must then be:

$$\mathcal{F}^{-1} \left[\sqrt{\frac{2}{\pi}} \frac{e^{-(\omega^2+1)\tau}}{1 + \omega^2} \right] = \frac{e^{-\tau}}{\pi\sqrt{2}} \int_{-\infty}^{\infty} \frac{e^{-\omega^2+i\omega\xi}}{1 + \omega^2} d\omega$$

Unfortunately, the resulting integral is not readily found in the tables consulted. Instead, the convolution theorem is applied. The convolution theorem states that the product of two Fourier transforms is the convolution of their functions.

$$\mathcal{F}[f * g] = \mathcal{F}[f]\mathcal{F}[g]$$

The convolution of the Fourier integral transform is defined as (Farlow 1993):

$$f * g = \frac{1}{\sqrt{2\pi}} \int_{-\infty}^{\infty} f(\xi - \chi)g(\chi)d\chi$$

Here, χ is simply a placeholder variable for integration. Letting g be the initial condition:

$$g(\chi) = -c_0 e^{-|\chi|}$$

The function f is then the solution to the differential equation for a point source.

$$f(\xi, \tau) = \mathcal{F}^{-1}[e^{-(\omega^2+1)\tau}] = \frac{e^{-\tau}}{\sqrt{2\pi}} \int_{-\infty}^{\infty} e^{-\omega^2\tau+i\omega\xi} d\omega$$

This integral, unlike the previous, is verifiable from tables.

$$f(\xi, \tau) = \frac{e^{-\frac{\xi^2}{4\tau}\tau}}{\sqrt{2\tau}}$$

This function is identical to the kernel of the Green's function. Evaluating the convolution with the initial value function results in the literal Green's function:

$$c_i(\xi, \tau) = f * g = \frac{1}{\sqrt{2\pi}} \int_{-\infty}^{+\infty} g(\chi) \frac{e^{-\frac{(\xi-\chi)^2}{4\tau} - \tau}}{\sqrt{2\tau}} d\chi$$

Substituting the initial condition transformed by the steady-state solution:

$$c_i(\xi, \tau) = -c_0 \frac{e^{-\tau}}{2\sqrt{\pi\tau}} \int_{-\infty}^{+\infty} e^{-|\chi| - \frac{(\xi-\chi)^2}{4\tau}} d\chi$$

As the initial condition is not smooth at the origin, it is pragmatic to separate the integral into two domains. Collecting the exponential terms:

$$c_i(\xi, \tau) = \frac{-c_0}{2\sqrt{\pi\tau}} \left(\int_{-\infty}^0 e^{-\left(\tau - \chi + \frac{(\xi-\chi)^2}{4\tau}\right)} d\chi + \int_0^{+\infty} e^{-\left(\tau + \chi + \frac{(\xi-\chi)^2}{4\tau}\right)} d\chi \right)$$

As the exponent of these integrals is quadratic, they can be greatly simplified by completing the square.

$$c_i(\xi, \tau) = \frac{-c_0}{2\sqrt{\pi\tau}} e^{-|\xi|} \left(\int_{-\infty}^0 e^{-\left(\frac{|\xi|-|\chi|}{2\sqrt{\tau}} + \sqrt{\tau}\right)^2} d\chi + \int_0^{+\infty} e^{-\left(\frac{|\xi|-|\chi|}{2\sqrt{\tau}} - \sqrt{\tau}\right)^2} d\chi \right)$$

In this form, the integrals are recognizable as a variant of the error function. The error function is defined by (Riley, Hobson and Bence 2004):

$$erf(z) = \frac{2}{\sqrt{\pi}} \int_0^z e^{-\chi^2} d\chi$$

To match this form, a further variable substitution is made:

$$\eta = \frac{|\xi| - |\chi|}{2\sqrt{\tau}} \pm \sqrt{\tau}$$

$$d\eta = -\frac{\chi}{|\chi|} \frac{d\chi}{2\sqrt{\tau}}$$

This conveniently matches the time dependent coefficient outside the integral. Making the substitution and further breaking the integrals apart into those in agreement with the definition of the error function:

$$c_i(\xi, \tau) = \frac{-c_0}{\sqrt{\pi}} e^{-|\xi|} \left(\int_0^{\frac{|\xi|}{2\sqrt{\tau}} + \sqrt{\tau}} e^{-\eta^2} d\eta - \int_{-\infty}^0 e^{-\eta^2} d\eta - \int_0^{+\infty} e^{-\eta^2} d\eta + \int_0^{\frac{|\xi|}{2\sqrt{\tau}} + \sqrt{\tau}} e^{-\eta^2} d\eta \right)$$

The improper integrals balance exactly as the integrand is an even function. The remaining definite integrals are then expressed in terms of the error function:

$$c_i(\xi, \tau) = \frac{-c_0}{2} e^{-|\xi|} \left(\operatorname{erf} \left(\frac{|\xi|}{2\sqrt{\tau}} + \sqrt{\tau} \right) + \operatorname{erf} \left(\frac{|\xi|}{2\sqrt{\tau}} - \sqrt{\tau} \right) \right)$$

However, this is only the transient portion of the solution. Adding in the steady state solution:

$$c_i(\xi, \tau) = \frac{c_0}{2} e^{-|\xi|} \left(2 - \operatorname{erf} \left(\frac{|\xi|}{2\sqrt{\tau}} + \sqrt{\tau} \right) - \operatorname{erf} \left(\frac{|\xi|}{2\sqrt{\tau}} - \sqrt{\tau} \right) \right)$$

This can be written in a slightly more compact form using the error function complement:

$$c_i(\xi, \tau) = \frac{c_0}{2} e^{-|\xi|} \left(\operatorname{erfc} \left(\frac{|\xi|}{2\sqrt{\tau}} + \sqrt{\tau} \right) + \operatorname{erfc} \left(\frac{|\xi|}{2\sqrt{\tau}} - \sqrt{\tau} \right) \right)$$

This is the complete solution to the transient reactive-diffusion equation where the Thiele Modulus is greater than approximately two. It can alternatively be expressed in dimensional coordinates:

$$c_i(x, t) = \frac{c_0}{2} e^{-\sqrt{\frac{\kappa_i \lambda_i}{\mathcal{D}_i}} |x|} \left(\operatorname{erfc} \left(\frac{|x| \sqrt{\kappa_i}}{2\sqrt{\mathcal{D}_i t}} + \sqrt{\lambda_i t} \right) + \operatorname{erfc} \left(\frac{|x| \sqrt{\kappa_i}}{2\sqrt{\mathcal{D}_i t}} - \sqrt{\lambda_i t} \right) \right)$$

While the form of this solution appears unusual, it is comparable to the Ogata-Banks solution to advective-diffusive transport for stable tracers in an infinite media (Ogata and Banks 1961). What is unusual here is that the infinite approximation is valid in finite media. In the limit of a small decay constant, this solution collapses into:

$$c_i(x, t) = c_0 \operatorname{erfc} \left(\frac{|x| \sqrt{\kappa_i}}{2\sqrt{\mathcal{D}_i t}} \right)$$

This is identical to the solution attainable by solving the diffusion equation on an infinite domain without reactivity. Therefore, the solution to a stable tracer in infinite media will be omitted. It is concluded that, when the distance to the no-flux boundary exceeds approximately two decay lengths, the system becomes insensitive to increased matrix size. That is, the system is effectively infinite after a finite distance due to radioactive decay.

While the definition of the apparent diffusivity requires knowledge of the geological parameters, it logically must be less than the diffusivity in unobstructed air. Utilizing diffusivities estimated by the methods of Bird, Stewart, and Lightfoot at 20°C and half-lives as tabulated by the NNDC, the following decay lengths in air are calculated (Bird, Stewart and Lightfoot 2002) (Tuli 2005):

Table 2.2 Diffusive Decay Length of Noble Gas Radionuclides in Air

Nuclide	Half Life (h)	$D_{i,Air}$ (cm ² /s)	L_{λ} (m)
³⁷ Ar	838.8	0.191	9.13
⁸⁵ Kr	94003.2	0.150	85.56
^{131m} Xe	286.4	0.124	4.29
^{133m} Xe	52.6	0.124	1.84
¹³³ Xe	125.8	0.124	2.85
¹³⁵ Xe	9.1	0.124	0.77

The tracer with the longest radioactive diffusion length is ⁸⁵Kr. While argon has a significantly higher diffusivity, the very long half-life dominates and it has a characteristic decay length of 85.56 m. Consequently, in all but the largest matrices, ⁸⁵Kr will have a small Thiele Modulus and the Fourier Modulus governs transport.

In comparison, the argon and xenon radionuclides have a decay length of 10 m or less in air. ¹³⁵Xe has the shortest length of less than 1 m. Even without further reducing the decay length due to porosity, tortuosity, saturation, and capacity, these lengths are likely to be well exceeded in geological media. Consequently, the Thiele Modulus will well exceed two and the system will behave as though it is infinite.

2.16. FRACTURE-MATRIX FLUX

While a radioactive tracer ceases to be sensitive to system dimensions for a large Thiele Modulus, the flux experienced by a radioactive tracer is still depending upon intrinsic transport properties. Similarly, a stable tracer in a finite matrix will fill according to its intrinsic transport properties, but the total flux is capped. As per section 2.6, the diffusive flux of a dilute tracer in a stagnant matrix follows a Fickian relationship:

$$J_i = -D_i \nabla c_i$$

Here it appears the flux is linearly dependent on the diffusivity. However, the concentration profile in the matrix is also affected by diffusivity as well as capacity and reactivity factors. With the analytical solutions from the previous section, the concentration gradient can be readily found through differentiation.

From section 2.14, the concentration profile in a finite matrix for a stable tracer follows:

$$c_i(\chi, Fo) = c_0 \left(1 - 2 \sum_{n=0}^{\infty} \frac{\sin(k_n \chi)}{k_n} e^{-k_n^2 Fo} \right)$$

As the Fourier Modulus is constant with position, the derivative in the x-direction is trivial:

$$\frac{\partial c_i}{\partial x} = \frac{d\chi}{dx} \frac{\partial c_i}{\partial \chi} = -\frac{2c_0}{L} \sum_{n=0}^{\infty} \cos(k_n \chi) e^{-k_n^2 Fo}$$

As at the interface, the x-coordinate is zero, the solution to the flux is:

$$J_i = D_i \frac{2c_0}{L} \sum_{n=0}^{\infty} e^{-k_n^2 Fo} = D_i \frac{2c_0}{L} \sum_{n=0}^{\infty} e^{-k_n^2 \frac{\mathfrak{D}_i t}{\kappa_i L^2}}$$

As discussed in section, this only represents the flux in the pores. As the pores only make up a fraction of the space, and as the pores are not orthogonal to the fracture-matrix surface, the surface normalized flux is:

$$\frac{J_i \cdot A}{|A|} = 2c_0 \mathfrak{D}_i \sum_{n=0}^{\infty} e^{-k_n^2 \frac{\mathfrak{D}_i t}{\kappa_i L^2}}$$

While the coefficient to this expression is independent of the capacity factor, the exponent is not. Consequently, the net effect of the capacity is to reduce the rate as which the flux diminishes.

This can be more clearly seen in the infinite media case, but still utilizing a stable tracer. Here:

$$c_i(x, t) = c_0 \operatorname{erfc} \left(\frac{|x| \sqrt{\kappa_i}}{2\sqrt{\mathcal{D}_i t}} \right)$$

The derivative in the x-direction is then:

$$\frac{\partial c_i}{\partial x} = -\frac{c_0 \sqrt{\kappa_i}}{\sqrt{\pi \mathcal{D}_i t}} e^{-\frac{x^2}{4\mathcal{D}_i t}}$$

Evaluating at the interface, the flux is then:

$$\frac{J_i \cdot A}{|A|} = c_0 \sqrt{\kappa_i \mathcal{D}_i} \left(\frac{1}{\sqrt{\pi t}} \right)$$

It has been placed in this form so as to separate the constant and time dependent portions. Finally, for the reactive case:

$$c_i(\xi, \tau) = \frac{c_0}{2} e^{-|\xi|} \left(\operatorname{erfc} \left(\frac{|\xi|}{2\sqrt{\tau}} + \sqrt{\tau} \right) + \operatorname{erfc} \left(\frac{|\xi|}{2\sqrt{\tau}} - \sqrt{\tau} \right) \right)$$

Finding the derivative with respect to x:

$$\frac{\partial c_i}{\partial x} = \frac{d\xi}{dx} \frac{\partial c_i}{\partial \xi} = -\frac{c_0 e^{-|\xi|}}{2L_\lambda} \left(\operatorname{erfc} \left(\frac{|\xi|}{2\sqrt{\tau}} + \sqrt{\tau} \right) + \operatorname{erfc} \left(\frac{|\xi|}{2\sqrt{\tau}} - \sqrt{\tau} \right) - \frac{2 \cosh(\xi)}{\sqrt{\pi \tau}} e^{-\left(\frac{\xi^2}{4\tau} + \tau\right)} \right)$$

Fortunately, when evaluating the gradient at the interface, the opposing error function components complement each other, resulting in a constant value of two. The flux in the pores is then:

$$\frac{J_i \cdot A}{|A|} = c_0 \sqrt{\kappa_i \mathcal{D}_i} \left(\sqrt{\lambda} + \frac{e^{-\lambda t}}{\sqrt{\pi t}} \right)$$

Here, there is both a constant and time-dependent contribution to the fracture-matrix flux. As it is hard to conceptualize what this means, functions for flux in each of the three cases will be plotted on a log-log scale. As one application of this theory is to explain the spurious $^{37}\text{Ar}:^{127}\text{Xe}:\text{SF}_6$ ratios observed at the Nevada Nuclear Security Site (Olsen, et al. 2016), these species provide an ideal example of this theory.

Figure 2.7 illustrates the response of each of these tracers assuming a porosity-tortuosity-saturation factor of 0.2. The SF_6 was plotted both in the infinite and the finite case of 1 m. The stable tracer in the finite case nearly follows the infinite case until it begins to reach capacity, at which point the flux rapidly trails off. Additionally, the ^{127}Xe was plotted both with a capacity factor of 1.0 and 1.5 as indicated by the solid and dotted lines, respectively.

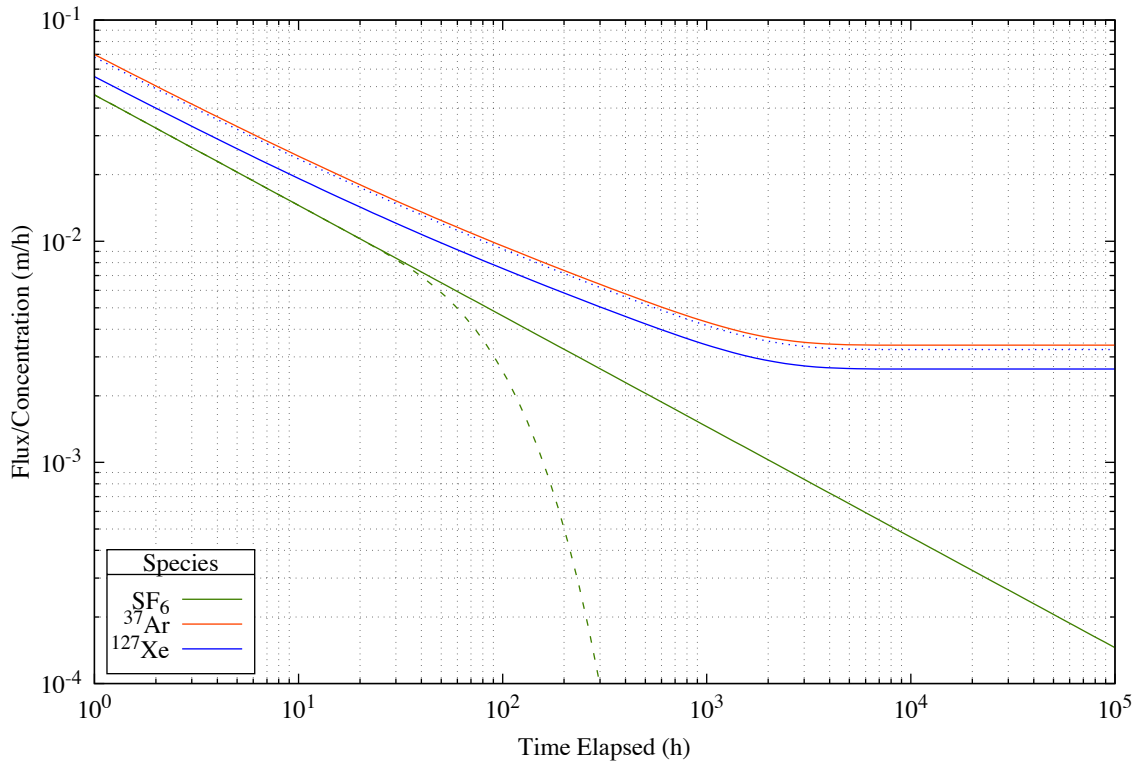


Figure 2.7 Theoretical Flux of ³⁷Ar, ¹²⁷Xe, and SF₆ undergoing Sorption and Decay

Essentially, the capacity factor acts to shift the flux to the right – that is higher concentration gradients persist longer. In addition, due to radioactive decay, a steady-state flux into the matrix is reached a time that is a function of half-life. As the half-lives of ³⁷Ar and ¹²⁷Xe are similar – 35.0 and 36.3 days respectively – this occurs at a similar location here. This is not always the case. For a stable tracer, the capacity factor will similarly push the flux response to the right, allowing additional material to transport, and more quickly, prior to reaching capacity at a later point in time.

Provided the theory discussed here is proven verifiable and a capacity factor of 1.5 is attainable, this has significant impact for the quantity of radioactive noble gases

reaching the surface. Aqueous solubility alone does not appear capable of reaching this capacity except in near saturation conditions.

Therefore, the dilute tracer transport model will be confirmed by measuring the diffusivity of these species in wet and dry porous media through application of gas chromatography-mass spectrometry. In addition, adsorption isotherms will be measured on a variety of geological substrates to determine if adsorption can account for the apparent increased capacity factor.

3. Gas Chromatography-Mass Spectrometry on Permanent Gases

Prior to engaging in a study in diffusivity, preliminary work was necessary to determine how the concentration of the relevant species will be quantified. Because the selection of tracer gases was dictated by field-tests, the quantitative method was required to support these gases. Furthermore, in a desire to maintain prototypical conditions, the tracer gases were limited to trace concentrations. While this ensures diffusion is approximately Fickian and Henry's Law is valid for sorption, it does limit the methods of detection suitable.

3.1. SELECTION OF QUANTITATIVE METHOD

The noble gases provide a unique challenge due to their monatomic existence. In the absence of molecular bonds, the noble gases lack rotational and vibrational modes commonly used in microwave or infrared spectroscopy. While excitation of electronic modes is possible, such as in atomic emission spectroscopy, this was not considered, as the technology is comparably expensive and was not available to demonstrate as proof of concept.

In contrast to molecular spectroscopy, mass spectroscopy depends only upon the molecular weight of the analyte and its fragments. Because the noble gases are found in a monatomic state, no fragmentation can occur and this technique yields spectra corresponding to isotopic abundances. As transport theory predicts a slight fractionation

of the isotopes by molecular weight, mass spectrometry has this as an additional advantage.

Complicating the quantitative method is that the other field-test tracer gas of concern is sulfur hexafluoride. While SF₆ can be readily quantified by infrared absorbance, and has high sensitivity in gas chromatography using electron capture detectors, it is also highly sensitive to mass spectrometry. Minimum detection limits as low as 5.2 ppt have been reported in optimized systems (Jong, et al. 2014).

Finally, while radioactive tracers are suitable for the noble gas tracers and the Nuclear Engineering Teaching Laboratory has experience in preparing these tracers (C. M. Egnatuk 2012) (Haas, Biegalski and Foltz-Biegalski 2009), no such experience is available in producing radioactive SF₆. When attempting to extend these methods to SF₆, two difficulties arise.

First, there is a lack of desirable radioisotopes of its elemental constituents. Fluorine is a monoisotopic element, existing only with the atomic weight of 19 amu. Activation through neutron capture results in ²⁰F, but with a half life of only 11.1 seconds, it is unsuitable for tracer experiments conducted over a period of hours.

Sulfur exists predominantly as the isotope ³²S. A significant fraction (4.25%) exists as ³⁴S and could theoretically be activated by neutron capture to ³⁵S, which has an acceptable half-life of 87.2 days. Alternatively, ³⁵Cl undergoes a (n,p) reaction to form ³⁵S (Leddicotte 1962). However, ³⁵S is a pure beta emitter, which is less desirable than gamma radiation for a tracer experiment due to the limited range of beta rays.

Second, while SF₆ is very inert, this is the result of steric hindrance and it is not the favored thermodynamic product. The effects of ionizing radiation on SF₆ have not been studied extensively, but it is likely to decompose to S₂F₁₀, SF₄, and F₂, all of which are exceedingly toxic and corrosive. While transmutation of ³⁴S or ³⁵Cl to ³⁵S in elemental form is possible, synthesis of SF₆ through fluorination requires F₂ as a reagent and yields SF₄ and S₂F₁₀ byproducts (Cotton and Wilkinson 1972). The toxicity and corrosiveness of the reagents and byproducts far outweighs the limited usefulness of a pure beta-emitting tracer.

Consequently, mass spectroscopy is the only suitable method of detection for trace quantities of both the noble gases and sulfur hexafluoride. Unfortunately, unlike gamma-ray or molecular spectroscopy, mass spectroscopy requires physically withdrawing samples from a system while methods relying on photons can be conducted using inline techniques. Because a physical sample must be withdrawn and processed by the GC-MS – which takes approximately 5 minutes for a permanent gas sample – the subsequent diffusion tests were engineering around this constraint.

3.2. DESCRIPTION OF THE GAS CHROMATOGRAPHY-MASS SPECTROMETRY SYSTEM

As mass spectroscopy was chosen for its versatility and potential to provide isotopic measurements, a more detailed description of mass spectroscopy and its variants is necessary. Mass spectroscopy encompasses all analytical techniques that aim to separate a sample into constituent components based on molecular mass. All mass

spectrometers have three components in common: an ion source, a mass analyzer, and a detector.

3.2.1. Ion Sources

Ion sources include electron impact ionization (EI), positive or negative chemical ionization (CI), and inductively coupled plasma (ICP), among others. Electron ionization was the method chosen, which can be summarized as the bombardment of a vaporized target at ultrahigh vacuum with electrons. Some of these electrons collide with the target species, transferring typically 70-eV of energy and liberating one or more electrons from the target. Thus, while the target is bombarded with electrons, the resulting ions are generally cations.

A potential disadvantage of EI is that this process generally breaks molecular bonds in the process. For complex organic molecules, the resulting fragment spectra may be exceedingly complex to analyze. Here, the fact that the noble gases are monatomic and that fluorine is monoisotopic is an advantage. The noble gases cannot fragment and fragments of SF₆ appear at regular intervals consistent with the mass of ¹⁹F. It is possible to doubly ionize a noble gas target. Mass spectra of various chemical species are generally available from the National Institute of Standards and Technology (NIST). Figure 3.1 depicts the resulting EI mass spectrum for atmospheric xenon.

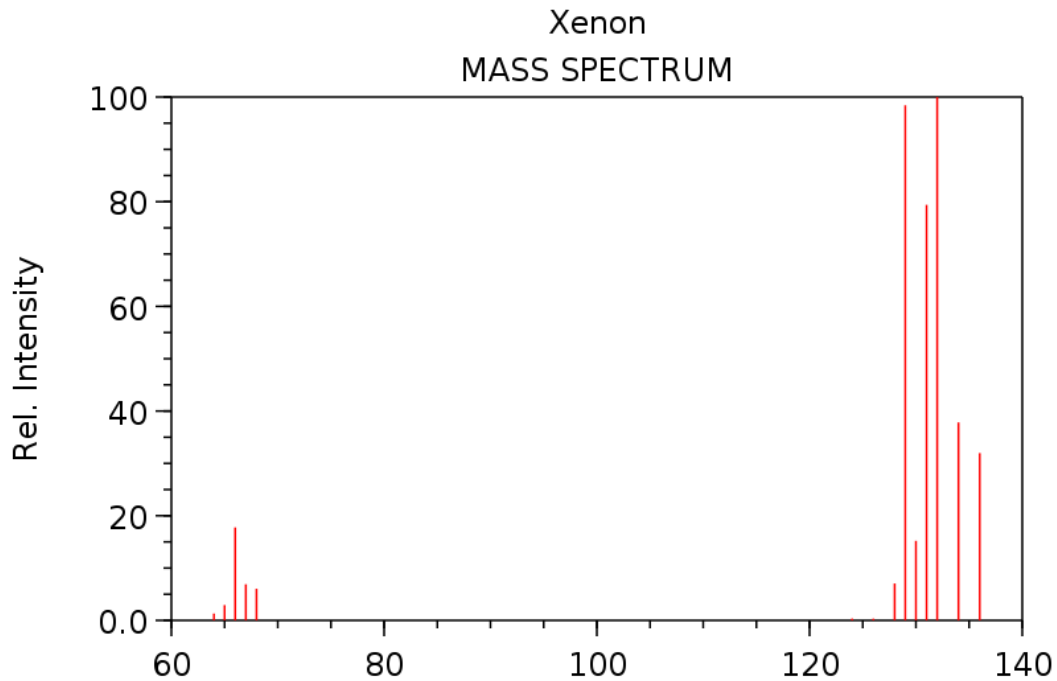


Figure 3.1 Atmospheric Xenon Mass Spectrum (Stein 2014)

The higher mass-to-charge peaks are indicative of the single ionization peaks. Because xenon is monatomic, these are directly proportional to isotopic abundances. The relative intensity of these peaks can be compared against the isotopic abundances listed in Table 3.1. Additional noble gas tracer species are listed for reference using data as tabulated the Knolls Atomic Power Laboratory (Baum, et al. 2010).

The peaks located at approximately 65 amu are the double ionization peaks. These peaks are lower in intensity as the likelihood of an electron removing two electrons on impact is less. In addition, because many mass analyzers are only capable of integer amu resolution, odd numbered nuclides that have been doubly ionized do not fit clearly into any integer mass channel. Consequently, the intensity of these doubly ionized species is generally split amongst adjacent channels peak range.

Table 3.1 Stable Argon, Krypton, and Xenon Weights and Isotopic Abundances

Isotope	Weight	Abundance
³⁶ Ar	35.968	0.34%
³⁸ Ar	37.963	0.06%
⁴⁰ Ar	39.962	99.60%
⁷⁸ Kr	77.920	0.35%
⁸⁰ Kr	79.916	2.28%
⁸² Kr	81.913	11.58%
⁸³ Kr	82.914	11.49%
⁸⁴ Kr	83.912	57.00%
⁸⁶ Kr	85.911	17.30%
¹²⁴ Xe	123.906	0.10%
¹²⁶ Xe	125.904	0.09%
¹²⁸ Xe	127.904	1.91%
¹²⁹ Xe	128.905	26.40%
¹³⁰ Xe	129.904	4.07%
¹³¹ Xe	130.905	21.23%
¹³² Xe	131.904	26.91%
¹³⁴ Xe	133.905	10.44%
¹³⁶ Xe	135.907	8.86%

In CI, an ionized reagent gas is introduced in great excess to the quantity of the analyte target. In the same method as molecular diffusion, these ionized gas particles may collide with the sample molecules. While kinetic theory assumed only elastic collisions, where charged species are present, electrons may be transferred between the reagent gas and the target species. The central advantage of this method over EI is that the reagent gas has a lower kinetic energy and is less likely to fragment the targets – simplifying a

complex mass spectrum. However, as the noble gases are unlikely to ionize in these collisions and as the mass spectrum of SF₆ is easily distinguishable, CI techniques are unnecessary for this work.

Finally, ICP mass spectrometry is primarily used where the sample is a solid or otherwise nonvolatile even under ultra-high vacuum. As the name suggests, in ICP the sample is heated in argon plasma until the sample dissociates and ionizes under extreme temperatures. Again, as the tracer gases are already volatile at ambient conditions, ICP provides no advantages in quantifying noble gases or SF₆.

3.2.2. Mass Analyzers

A variety of mass analyzers are available with different purposes in mind. The model that is frequently referenced in is the sector type as it was the type used by the Calutron to separate ²³⁵U during the Manhattan Project. In this type, a charged particle is first accelerated by an electric field and then in a magnetic field. By the Lorentz force law, a charged particle moving in a magnetic field will be experience forces in the direction perpendicular to both the magnetic field and particle velocity. Consequently, the particle will travel a curved path dependent up on mass-to-charge ratio, m/z. Locating sensitive film or detectors at various positions in space can then produce the mass spectrograph.

The primary advantage of the sector type is high throughput over a small range of mass-to-charge ratio. For this reason, it remains in use for isotope-ratio mass spectrometry (IRMS). It however has two disadvantages, the first of which is significant

cost. The other disadvantage for this application is its limited dynamic range. While sufficient for any one he tracer gases, measuring all the tracers in one sample requires the ability to scan over a range of m/z covering ^{36}Ar through ^{136}Xe .

In contrast, the most common mass analyzer type that can support this range is the single-quadrupole mass analyzer (QMS). Again, an ion is first accelerated to enter the QMS. Instead of being subjected to a static magnetic field, the QMS applies a combination of AC and DC currents. Rather than following a curved path, only ions with the desired mass-to-charge ratio follow a straight-line path while the remainder deviate and collide with non-detecting surfaces. In contract with the sector type, varying the radio frequency of the electric current can rapidly change the range of this instrument.

For complex organic samples, multiple EI and QMS ion sources and mass analyzers may be arranged in series. Two in series is known as tandem while three is triple. However, as there are no fragmentation products of the noble gases and the chemical tracers are easily identifiable with the single mass analyzer, these were not necessary.

Additional mass analyzers include time-of-flight, which accelerates charged particles over a finite distance and calculates the mass-to-charge ratio as a function of arrival time. This type is particularly useful for sub-amu resolution and for measuring substances with molecular weights in excess of 1000 amu. However, as neither of these features is necessary for noble gases or chemical tracers, these devices were not chosen.

3.2.3. Gas Chromatograph

While not fundamentally a component of mass spectroscopy, many mass spectrometers are tied to secondary analytical technique such as liquid or gas chromatography. While seemingly superfluous here, many organic molecules have similar molecular weights, as they are composed of a few elements of similar atomic mass. If these substances can be separated first by a physical property – such as boiling point in ordinary gas chromatography – the substances arrival at the ion source can be separated in time. In tandem with the mass spectrum, the ion chromatograph can provide unambiguous identification of structural isomers. As will be discussed in the method development, the use of a molecular sieve gas chromatography column is capable of separating the permanent gases.

3.3. QUANTITATIVE METHOD DEVELOPMENT

Once identified as potential detection technique, the GC-MS method was demonstrated with guidance from Ian Riddington at the Mass Spectroscopy Facility with the Chemistry Department at The University of Texas. It was confirmed that, as expected, both Xe and SF₆ could be detected using Electron Ionization (EI) mass spectrometry with a single quadrupole mass analyzer (QMS). Also, it was demonstrated that SF₆ fragmented upon ionization to SF₅⁺, SF₄⁺, and so on.

Unfortunately, during attempts shuttling gas samples to and from the Pickle Research Campus and Welch Hall revealed xenon would permeate through the silicone septa of the 1.5-mL chromatography vials first attempted. Considering the additional

syringe operations, inconsistent permeation rates – possibly due to variations in the size of the punctures in the septa – and an inability to establish configuration management on a shared instrument led to the procurement of a GC-MS system for the Nuclear Engineering Teaching Laboratory, which is pictured in Figure 3.2.



Figure 3.2 The GC-MS at the Nuclear Engineering Teaching Laboratory

Even with under the best conditions for a dedicated local instrument, many experimental uncertainties remain. Some factors are external to instrument – such as the quantity of gas withdrawn and injected – while others are internal. These include level of vacuum, efficiency of the ion detector, mass analyzer calibration, and so forth. Two methods of calibration are applicable to gas chromatography-mass spectrometry: external and internal. Initially, the external method was attempted for expediency.

3.3.1. External Calibration

In the external method, various known quantities of the species of interest are injected and the response curve is fitted. Factors such as ionization current, detector voltage, and quantity injected can significantly alter the signal. However, in a properly tuned instrument for the sample to be analyzed, the intensity, I , of the response should be linear with little to no threshold. Therefore the slope m_i^j , also known as the response factor, encompasses the transport, ionization, selection, and detection efficiency of the compound i into the mass-to-charge channel j , while b^j represents the background concentration and electronic noise.

$$I^j = m_i^j c_i V + b^j$$

As this is an external method, the signal intensity is directly proportional to the concentration and volume injected.

To maximize the response factor for a sample of known mass-to-charge but unknown quantity, the mass spectrometer can be programmed to use Selected Ion Monitoring (SIM). In SIM mode, the mass analyzer is tuned to a discrete number of channels, rather than scanning over a broad band, which can increase signal strength substantially. As the application here is strictly a quantitative, SIM mode was utilized throughout.

To statistically estimate the calibration curve, a number of reference samples of SF₆ and Xe were prepared through dilution of a pure gas into gas chromatography vials. As noticed in the conceptual phase, xenon was observed to permeate through the silicone

septa, thereby requiring new dilutions to be performed with each calibration. Much larger, 40-mL chromatography vials replaced the 1.5-mL vials for two reasons. First, the response to 1% SF₆ and Xe at the Mass Spectrometry Facility was very strong. There is a desire to reduce the experimental concentrations used to as low as reasonably achievable to be representative of field test conditions and to ensure the validity of the Fickian diffusivity. To produce parts per million concentrations in a vial using a microliter syringe requires larger dilution volumes. And second, the septa surface area to vial volume ratio is vastly improved in the 40-mL vials, presumably dampening the effect of permeation.

To prepare the reference samples, research-grade gas is expanded into an evacuated gas transfer manifold. A gastight syringe is inserted into a septum on the manifold, the plunger drawn past the prescribed volume and after confirming there is a pressure response on the gage and then slowly inserted to the intended volume. The pressure is then allowed to equalize and is recorded prior to shutting the valve on the syringe. The syringe is then injected through the septum a gas chromatography vial, which was equalized to ambient temperature and pressure prior to sealing. Temperature is assumed to be constant and ambient throughout this process. The process is then repeated for any additional gases of interest. Assuming an ideal gas mixture and isothermal conditions, the molar fraction of the reference material i in the vial is then:

$$x_i = \frac{p_i V_i}{P_{atm} V_{vial} + \sum_i^n p_i V_i}$$

The nominal volume of the chromatography vials was 40mL; this has been confirmed by water displacement to ± 2.6 mL tolerance. Atmospheric pressure is measured using the same pressure transducer as used to measure the pressure of the reference material – reducing linear calibration error in pressure measurements. In addition, as the magnitude of the dilutions necessary is approximately 1000:1, the molar concentration in the vial is effectively:

$$c_i = \frac{p_i}{RT} \frac{V_i}{V_{vial}}$$

This process was repeated a variety of times prior to attempting each diffusion test. As the response of the instrument varied with each test, each calibration will not be detailed here. However, to illustrate the linearity of this method, Figure 3.3 is provided. While ions are present in a number of mass-to-charge channels, the concentration can be determined from a single ion channel – also known as the quant ion. Here, m/z of 127 is the ion SF_5^+ that represents SF_6 concentration while m/z of 132 is the ion $^{132}\text{Xe}^+$ and is representative of total xenon concentration.

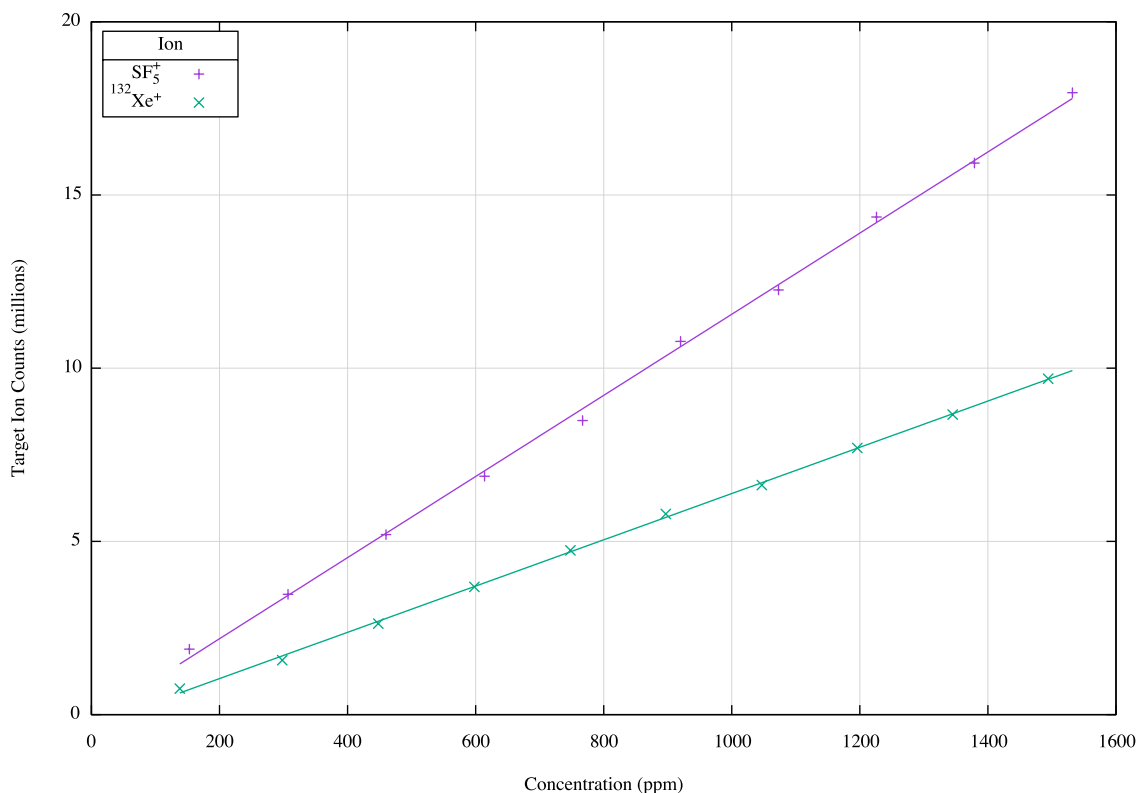


Figure 3.3 Linearity of Xe and SF₆ Target Ion Counts with Concentration

This figure demonstrates the linearity of the signal intensity with concentration out to fairly high concentrations of 1000 ppm or greater. In addition, the target ion counts are well into the millions for a 50- μL sample. Consequently, sufficient ion counts are available even at concentrations well below the range depicted here.

A number of tests were conducted by this method, notably the results presented at the INGE conference (Paul, et al. 2015). Provided the linearity is stable and the sample volumes consistent, this method can produce satisfactory results. Unfortunately, stability has proven to be a rarity. Figure 3.4 depicts the results presented at INGE, which were obtained as the best set of results after multiple attempts using the external method.

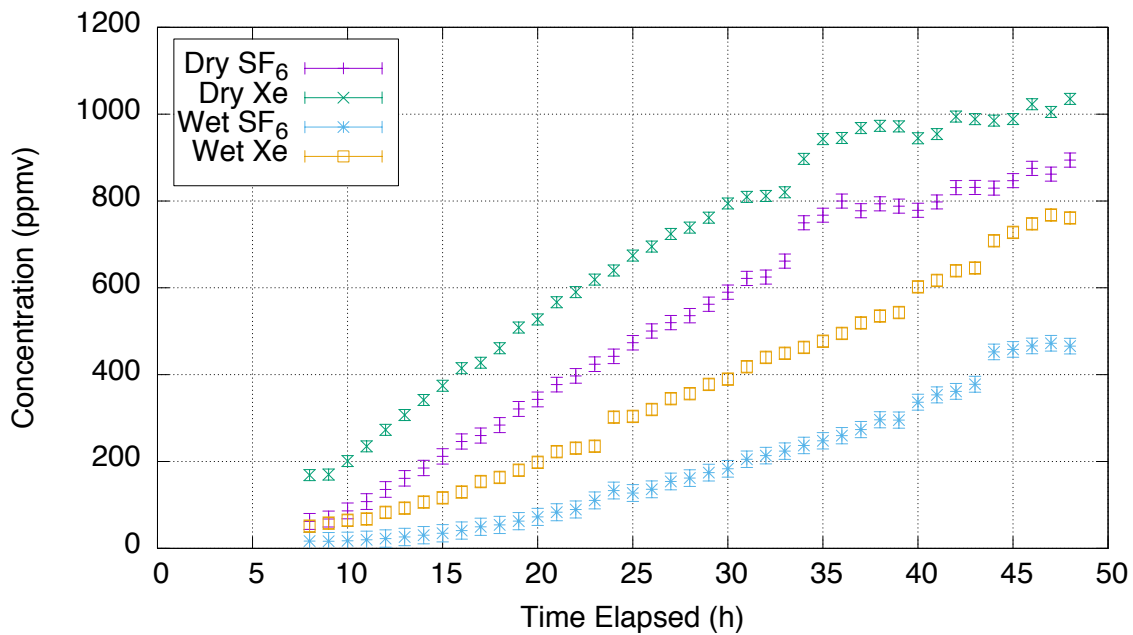


Figure 3.4 Concentration vs. Time Utilizing External Calibration

For reasons aside from the discontinuities, these results are of limited value in calculating transport properties. However, the discontinuities located at 24, 40, and 44 hours on the dry test as well as 33 hours on the wet test highlight the instabilities of the sample volume.

While the discontinuities, believed from syringe malfunctions, are clear to see, systematic error due to a drifting response factor is far more problematic. By taking samples at regular intervals, it is not apparent if the response factor is constant. During a separate diffusion test attempt utilizing this method, it is clear that the response factor is not constant. This is seen in Figure 3.5, where the response to both Xe and SF₆ spike after periods of inactivity.

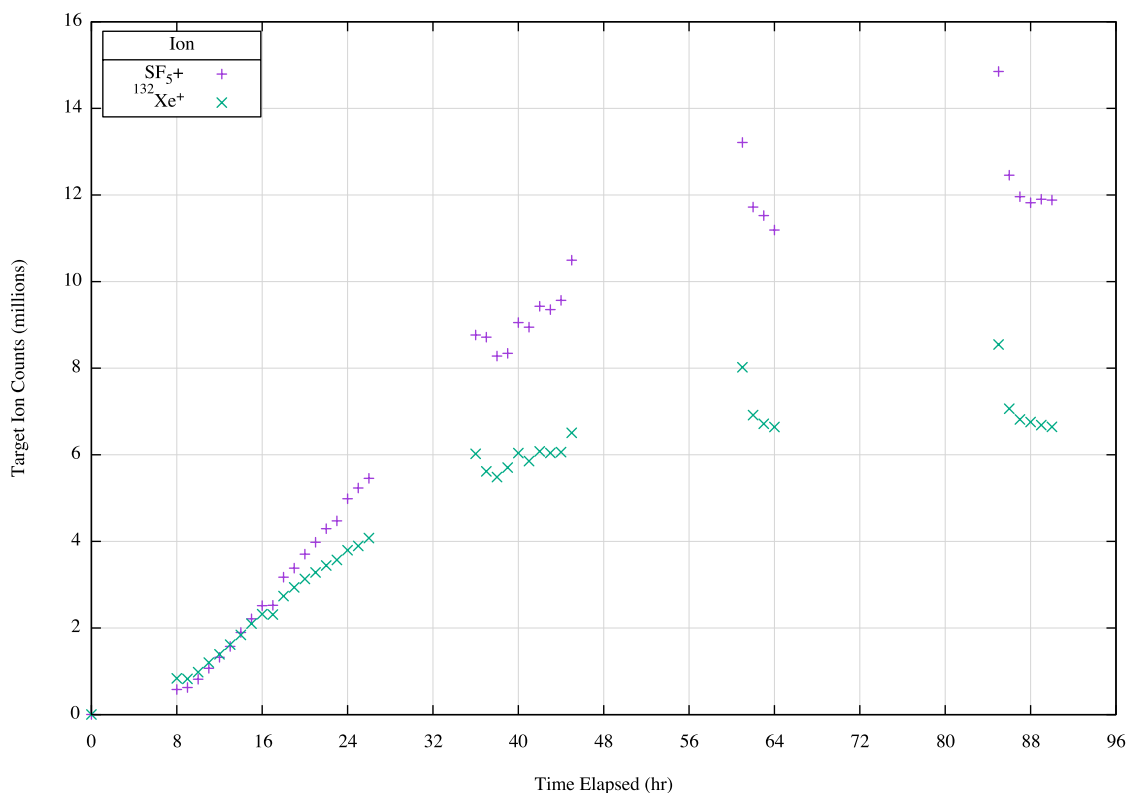


Figure 3.5 Discontinuities in Target Ion Counts during Irregular Sampling Intervals

It is suspected this is a result of accumulating gases within the mass spectrometer that quench the ionized species before reaching the detector. As the ion chamber is held at ultra high vacuum, the time to reach ultimate vacuum is diffusion limited – through Knudsen diffusion although the pore diameter is on the order of centimeters. It is possible for the time to reach ultimate vacuum after even a 50 μ L sample to take hours. Thus, after long periods of inactivity, the level of vacuum improves and more ions reach the detector improving the response.

This poses a significant problem in applying the external calibration method for diffusion tests. As the response factor is only valid at the same conditions at which the calibration points were measured, but yet the test is transient, it is unrealistic to

hold the conditions precisely the same. By taking samples at regular intervals, the systematic error is smoothly varying, but is nevertheless unknown. Fortunately, it is also apparent that the spike in sensitivity is correlated amongst the species. This can be exploited through use of an internal standard.

3.3.2. Internal Calibration

As noted, the GC-MS system was observed to be unstable where the frequency between samples varied. However, to confirm the suspicion that the response factor was also varying with time, albeit smoothly, the peak areas of nitrogen isotopologues weight 29 amu were monitored simultaneously to a future diffusion experiment. As nitrogen is a major background component of the air in the diffusion apparatus, if the system is stable, the m/z 29-peak area should be constant. Random error should be observed as a normal distribution around the mean. However, when plotting the results versus time, the following response was observed:

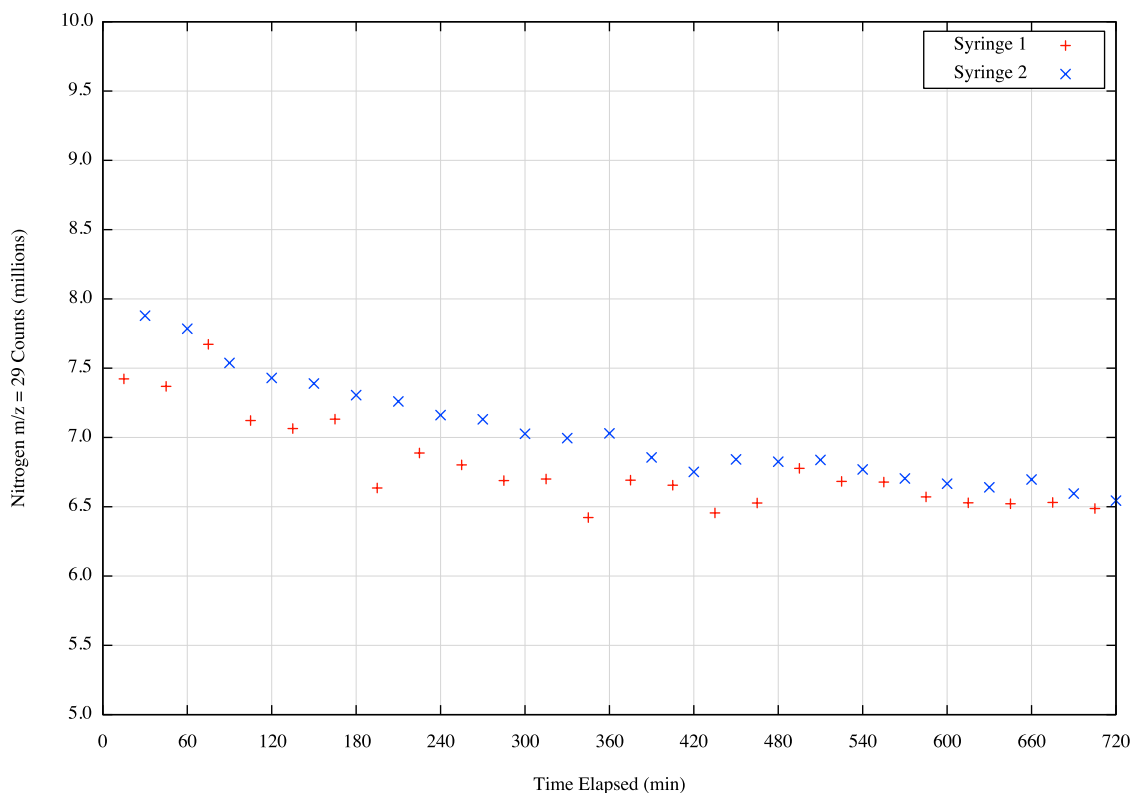


Figure 3.6 Nitrogen Internal Reference Intensity versus Time

Two features are prominent. First, both curves follow an exponential decay, indicating the nitrogen response factor is diminishing with time. This is consistent with the concept that ultimate vacuum is not reached between samples with a sample frequency of 15 minutes. Consequently, the results of an external calibration method will contain systematic bias towards lower concentrations with increasing time.

Second, the random error about the exponential decay is far greater in measurements from syringe number one. During the test, different syringes were used at the top and bottom locations; thereby it is likely this increased error is due a breakdown in the syringe seals. While the random error can be overcome with a large number of

samples, increasing the sample size will only exacerbate the unknown systematic error introduced by the diminishing response factor.

Primarily to resolve this systematic bias, but also to reduce the random error, the internal calibration method was utilized. In the internal calibration method, a sample with an unknown target species concentration is mixed with a reference species of fixed concentration. The quantity of the target species i is then proportional to the ratio of the target ion intensity divided by the reference ion intensity. The slope of this calibration is then known as the relative response factor:

$$I^{j:r} = m_i^{j:r} c_i + b^{j:r}$$

Because the sample volumes are identical for the target and reference species, the volume cancels out exactly. As the reference species will have a fixed concentration, the reference species concentration is lumped together in relative response factor. As with the external calibration method, there may be a threshold due to electronic noise, however this contribution is small for most concentrations.

As this method promises to reduce both systematic and random error, the logical next step is identifying a suitable reference ion. An ideal internal reference has chemical and physical properties which are similar if not identical to the target ion, but which can be distinguished by the detector. When using a mass spectrometer as the detector, the ideal internal standard is an isotope of the target. A second requirement of the internal standard is that it can be held at constant concentration throughout all of the samples.

The internal standard can be introduced to a fixed concentration by injecting it and allowing it to diffusive to equilibrium. However, as one area of concern is xenon

permeation, it is unclear that an introduced xenon standard would be held constant over an extended period of time. In addition, SF₆ enriched in sulfur isotopes was not available. Regardless, if an isotopically labeled internal reference is introduced, it adds to the complexity of the procedures to conduct the diffusion test and is less desirable.

3.3.3. Atmospheric Internal Reference

A search was then conducted for a suitable reference ion. A convenient internal standard would be one that is already diluted to a fixed concentration, thereby simplifying the procedures and reducing uncertainty. As the objective is to measure tracers through standard atmosphere, the search began with consistent atmospheric components. The following table lists the major components of dry air at sea level (United States Committee on Extension to the Standard Atmosphere 1962):

Table 3.2 Normal Composition of Clean, Dry Atmospheric Air Near Sea Level

Gas	Molar Fraction (%)
Nitrogen	78.084
Oxygen	20.9476
Argon	0.934
Carbon Dioxide	0.0314
Neon	0.001818
Helium	0.000524
Krypton	0.000114
Xenon	0.0000087

Argon, krypton, and xenon are potential target ions, therefore are not eligible reference ions when experimenting with these species. Both carbon dioxide and oxygen are undesirable due to their reactivity and solubility in water. This leaves nitrogen and neon as potential internal standards.

As a noble gas, the mass spectrum of neon consists of peaks proportional to isotopic abundance. Neon consists of three stable isotopes in abundances as follows:

Table 3.3 Atomic Weights and Abundances of Stable Neon Isotopes

Isotope	Weight	Abundance
^{20}Ne	19.992	90.45%
^{21}Ne	20.994	0.27%
^{22}Ne	21.991	9.25%

However, at the time neon was considered, a molecular sieve column was not available. Consequently, all of the permanent gases eluted at approximately the same time. A conflict arises in that the double ionization peak of $^{40}\text{Ar}^{++}$ has the same integer mass-to-charge ratio as $^{20}\text{Ne}^+$. Also, carbon dioxide has a double ionization peak at the same m/z ratio as $^{22}\text{Ne}^+$. Because of the relative abundance of CO_2 over Ne, the ^{22}Ne signal is dominated by the variable CO_2 signal. Figure 3.7 and Figure 3.8 are taken from NIST standard 70-eV EI mass spectra and illustrate the relative intensity of the double ionization peaks for Ar and CO_2 (Stein 2014).

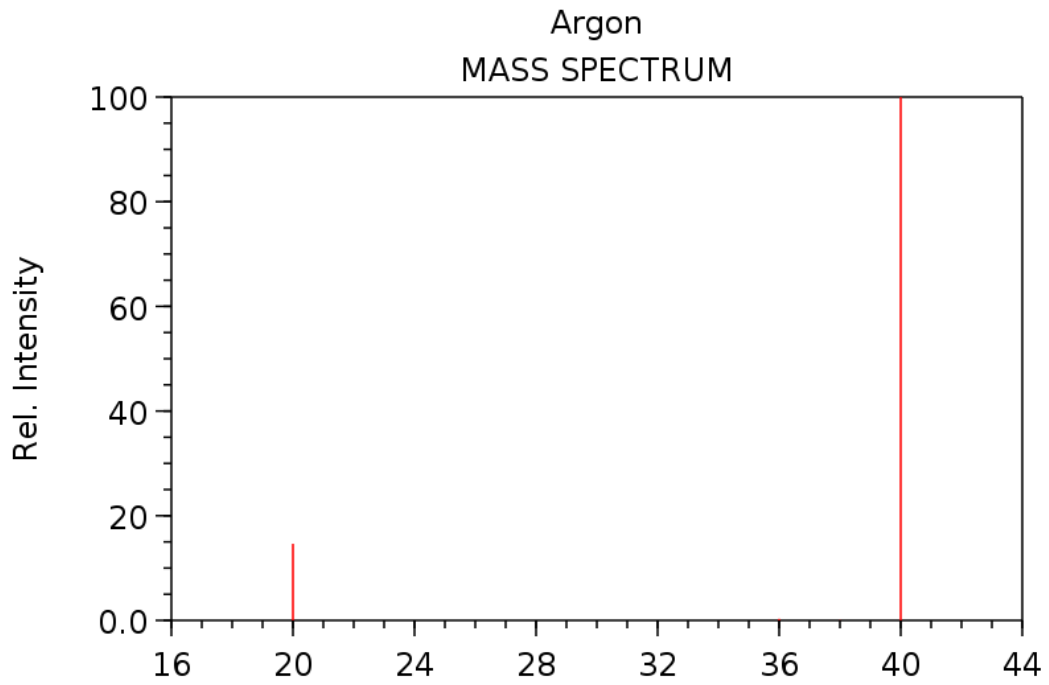


Figure 3.7 Atmospheric Argon Mass Spectrum (Stein 2014)

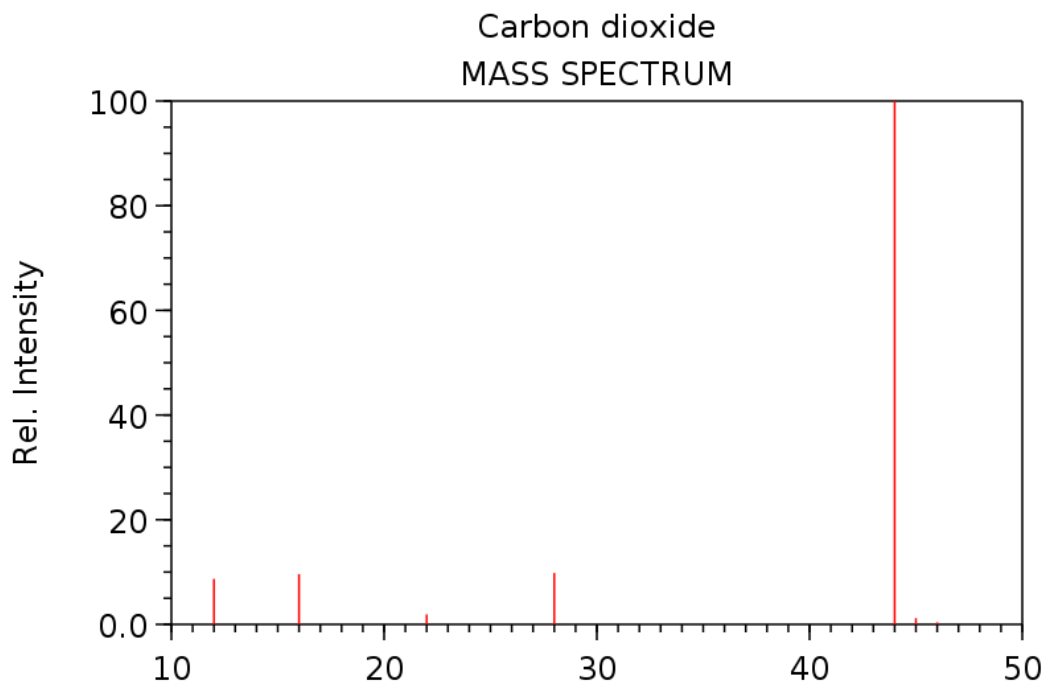


Figure 3.8 Atmospheric Carbon Dioxide Mass Spectrum (Stein 2014)

Because of this overlap, only the ^{21}Ne isotope is able to be observed independently where CO_2 and Ar are collating. Due to the scarcity of ^{21}Ne – only 49 ppb – and the high ionization energy of neon, the signal strength was insufficient for use as an internal standard.

The remaining choice is nitrogen. Nitrogen consists of predominantly ^{14}N , but there is a trace quantity of the isotope ^{15}N . However, unlike the noble gases, nitrogen exists in a diatomic form. The abundance of the diatomic bonds is assumed to have a binomial distribution in accordance with the isotopic abundances.

Table 3.4 Weights and Abundances of Stable Nitrogen Isotopologues

Isotopologue	Weight	Abundance
$^{14}\text{N}-^{14}\text{N}$	28.006	99.265%
$^{15}\text{N}-^{14}\text{N}$	29.003	0.733%
$^{15}\text{N}-^{15}\text{N}$	30.000	<0.002%

From the NIST electron ionization mass spectrum shown in Figure 3.9, nitrogen preferentially forms the molecular ion N_2^+ versus dissociation. This is representative of the strength of the nitrogen triple bond. However, there is a trace peak located at m/z 29 corresponding to the ^{15}N contribution. This is advantageous here as the nitrogen isotopologue $^{15}\text{N}-^{14}\text{N}$, with a molecular weight of 29 amu, has a mole fraction of 5720 ppm, which is utilizable when measuring components in the ppm range. In contrast, the mole fraction of $^{15}\text{N}-^{15}\text{N}$, having a molecular weight of 30 amu, is approximately 15.6 ppm and may be of potential interest where the former signal is too strong.

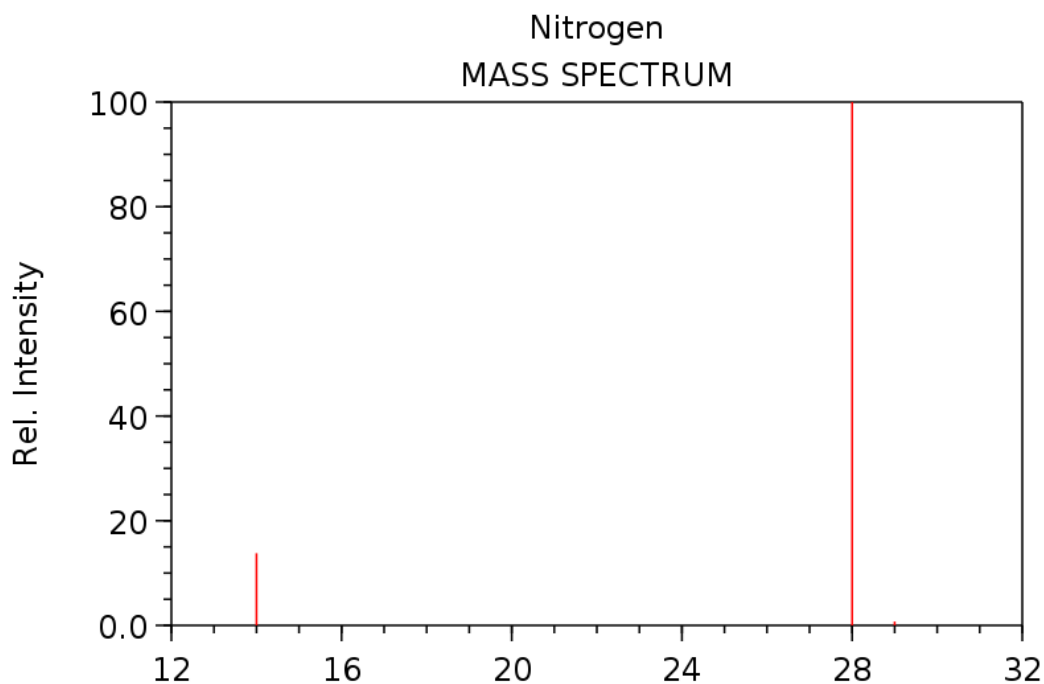


Figure 3.9 Atmospheric Nitrogen Mass Spectrum (Stein 2014)

If the internal standard is an isotopologue, the relative response factor is essentially unity. However, where an alternative chemical is used, the relative response factor varies with electron impact ionization cross-sections and transport efficiencies. It is essential that the relative response factor is a constant and highly linear. This can be confirmed by plotting the covariance matrix of the target ions intensity versus the reference ion intensity. Figure 3.10 depicts the covariance of various xenon isotopes versus $^{15}\text{N}^{14}\text{N}$.

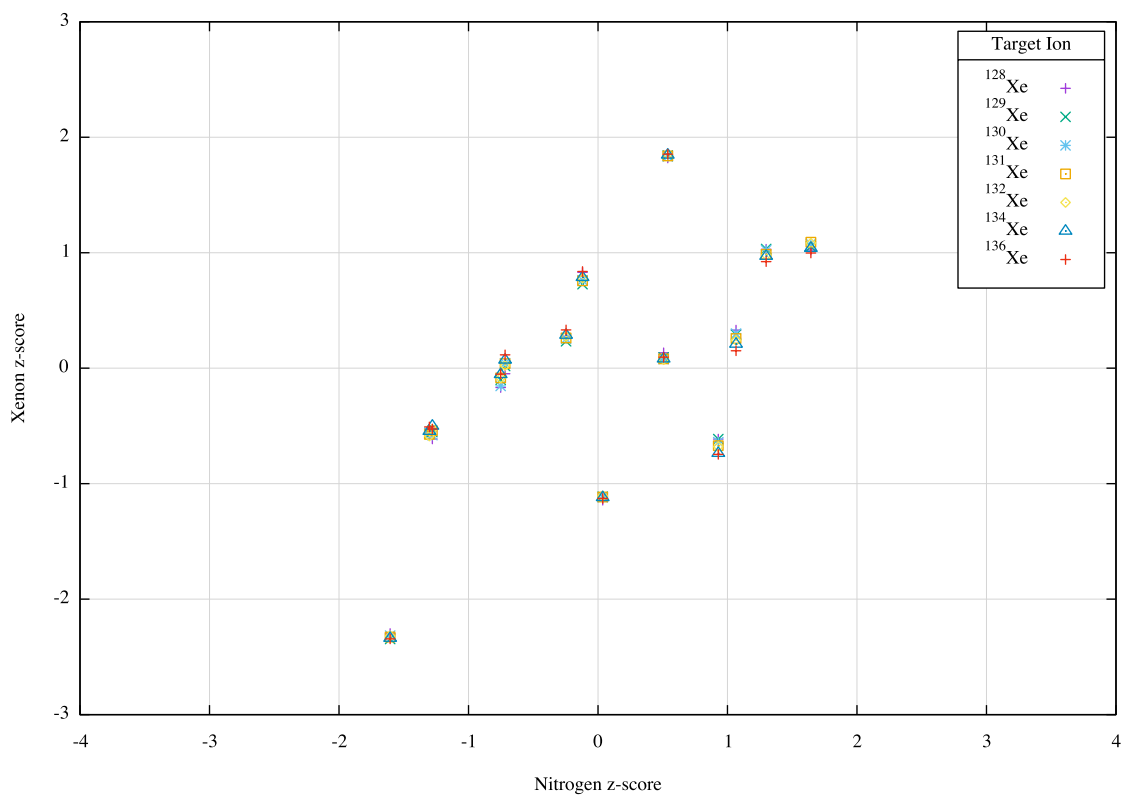


Figure 3.10 Covariance of Xenon Nuclides vs. ¹⁵N¹⁴N

While there was a positive correlation between target ion and reference ion, the correlation is not as strong as desirable. In contrast, the various xenon ions of this data set are far more correlated. Figure 3.11 shows the same data plotted instead against ¹³²Xe ions:

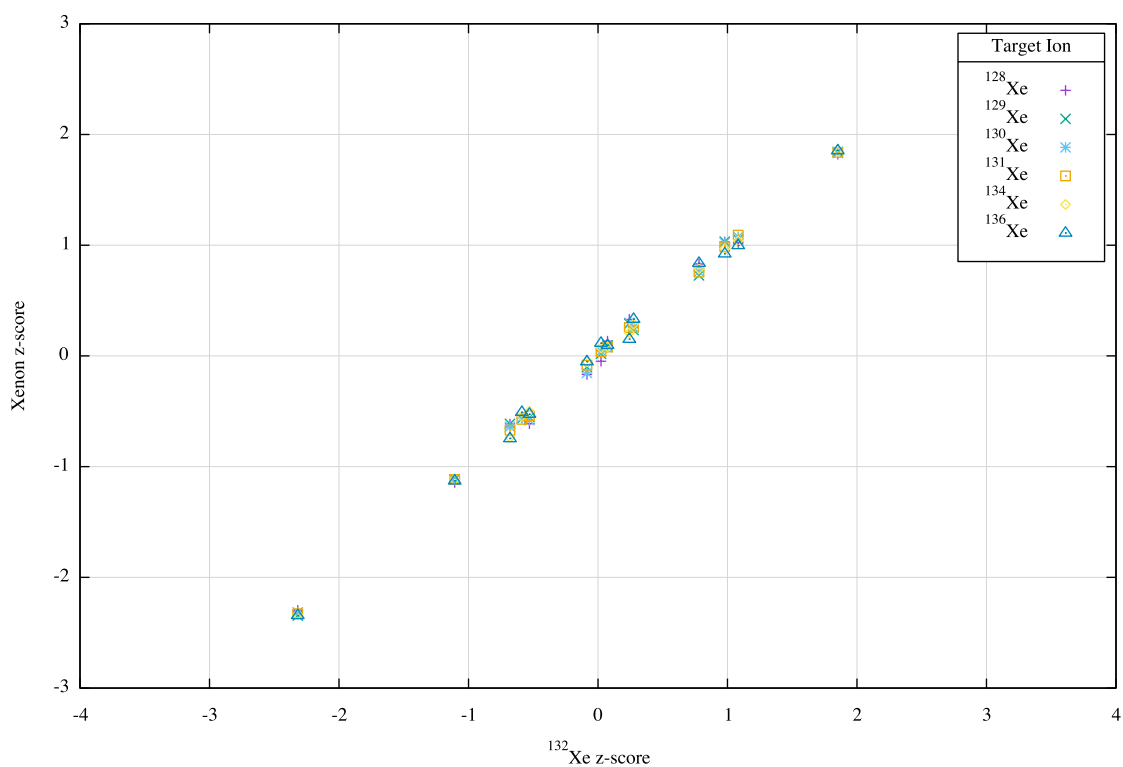


Figure 3.11 Covariance of Xenon Nuclides vs. ^{132}Xe

While this is an ideal correlation, it is not practical to use Xe in this case as it is unknown if permeation or sorption will alter the concentration of the reference during the course of the test. However, what this indicates is that the scattered distribution in the nitrogen covariance plot is likely random versus systematic error. It is proposed that the source of this error is small but random air inclusions entering the GC-MS, either retained in the needle between drawing the sample and injection, or during the brief period the septa is punctured.

While nitrogen isotopologues may not be the ideal internal standard, they do satisfy the chemical and physical requirements. Despite the correlation matrix not being narrowly distributed, it nevertheless improves precision over the external standard

method by removing systematic error, albeit introducing additional random error. Random error, unlike systematic error, can be accounted for through statistical models and increased number of samples. Some diffusion results discussed later in this text will subsequently utilize nitrogen as an internal reference.

Furthermore, utilizing an atmospheric internal standard is not always a matter of convenience. In open field tests, where it is not possible to spike the system with a synthetic reference, the use of trace atmospheric components is the only method by which the internal calibration method can be used.

3.3.4. Synthetic Internal Reference

Because the xenon isotopes are so well correlated, it was postulated that air inclusions in the syringe operations are inconsistent, leading to the excessive variance. Subsequently, the experimental procedure was modified to spike the column with a comparable amount of non-atmospheric reference gas. By using a synthetic reference material, air inclusions are immaterial where the target ion concentration greatly exceeds atmospheric abundance. Carbon tetrafluoride was selected as it is also a permanent gas, its ion fragments do not overlap with the intended target ions, and it is relatively insoluble in water. Figure 3.12 demonstrates the tighter correlation between xenon nuclides and carbon tetrafluoride.

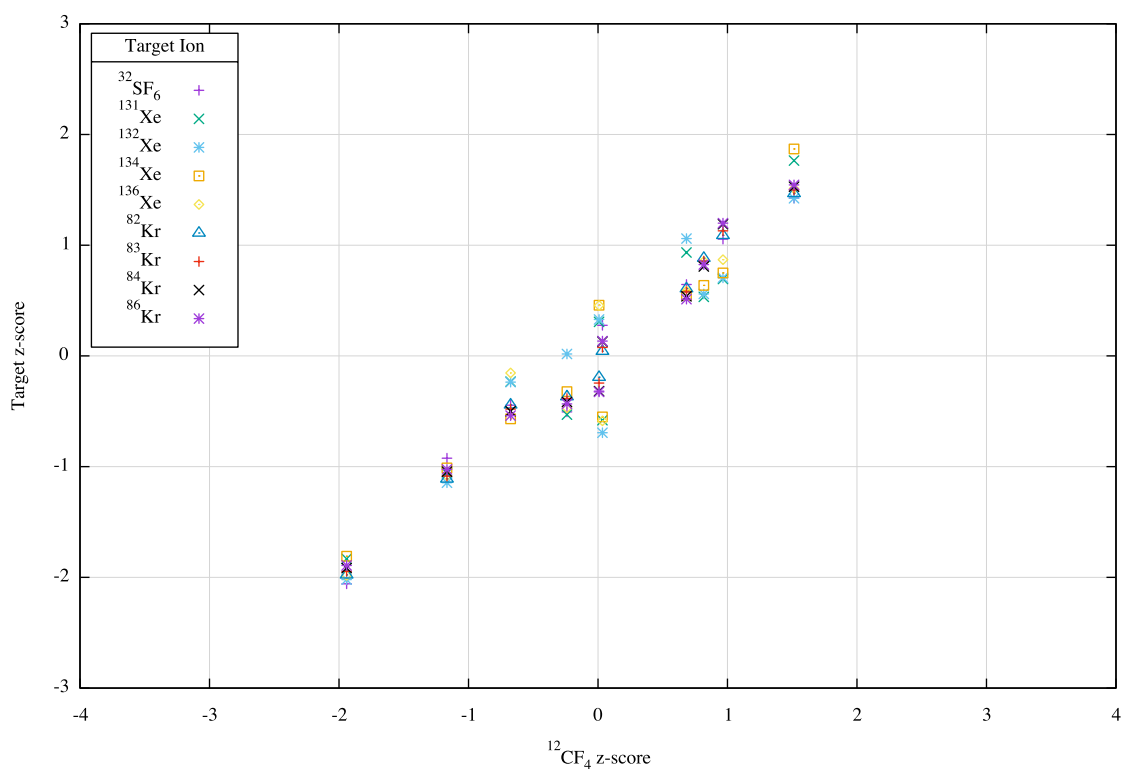


Figure 3.12 Covariance of Xe, Kr, and SF₆ vs. CF₄

While the covariance is not as ideal as an isotopic reference, it is nevertheless improved over the nitrogen reference. As carbon tetrafluoride is not found naturally in the atmosphere, it is thereby consistent with the hypothesis that the increases nitrogen variance was due to air inclusions. After this reference species was identified, it was utilized by injecting a small quantity of CF₄ into the column approximately one day prior to conducting the test to ensure a homogeneous distribution.

3.4. GAS CHROMATOGRAPHY VIA MOLECULAR SIEVES

While the mass-spectrometer is capable of separating compounds by mass, or at least the mass of the fragments. However, if two species have similar mass, the signal at the mass spectrometer will be convoluted. Furthermore, if the intensity of one species greatly exceeds that of another, the weaker signal may be dominated by noise.

While this was not typically a difficulty with the tracer gases mentioned to thus far – the overlap of $^{34}\text{SF}_5^+$ with ^{129}Xe being the only exception – the situation arose in support of field tests conducted in October 2016 at the Devine Test Site auxiliary to this research. There was a proposal to utilize acetylene – C_2H_2 – as a potential replacement for SF_6 as a tracer species. Because acetylene weighs 26 amu, it is near the nitrogen 28 peak. While the mass analyzer is excellent, the requirements of the test necessitated separation on part per trillion levels. Consequently, even low-level noise from the nitrogen peak can dominate the acetylene signal. Therefore it was desirable to separate the peaks in time.

In traditional gas chromatography, liquid samples are separated by their boiling points or vapor pressure. However, permanent gases cannot be separated by these properties at ambient temperatures. To permanent gases can be separated by cryogenic temperature or through strongly adsorbing and selective media such as molecular sieves. A molecular sieve is a material with microporous structure on the scale of chemical structures. Monatomic noble gases are able to penetrate these pores and have a very large specific surface area available to them for adsorption. SF_6 , on account of its hypervalency, is substantially larger and is unable to penetrate the micropores. It is

therefore swept away quickly by the carrier gas, despite its larger mass and usual adsorption affinity, while the smaller molecules are retained for a longer time.

A secondary purpose of the molecular sieve is to concentrate a larger sample volume for detection by the mass spectrometer. That is, a larger volume of a sample can be injected without the undesirable quenching effect of nitrogen, oxygen, and other atmospheric gases found in higher concentrations than the tracer. This is one aspect of the procedure reported to measure ppt quantities of SF₆ Jong et al (Jong, et al. 2014).

In this case, a 15-m molecular sieve type-5Å porous-layer open tubular (PLOT) column was procured and installed. The, type 5 Å is a reference to the size of the pores, 5 angstroms. To protect the mass spectrometer from potential particle entrainment from the molecular sieve, an additional 15 m of 0.25 mm ID dimethyl polysiloxane was installed between the plot column and the detector.

The molecular sieve had excessive separative power at ambient temperatures. However, molecular sieves performance is susceptible to poisoning by adsorption of water vapor. In an effort to minimize this effect and decrease the time of elution, the temperature of the GC was raised to 130°C while the column flow rate was increased to 19.3 mL/min of helium. A split ratio of 20:1 was used on the injector to best shape the peaks without a loss of intensity. Using these settings, the SF₆ eluted first, as expected due to its hypervalency, at approximately 1.4 min. Kr arrive at approximately 1.8 min and CF₄ at 2.2 min. Owing to its large adsorption affinity, Xe arrived last at 3.1 min. Figure 3.13 shows the chromatogram, split for each isotopologue, for these gases. This method was used successfully when utilizing CF₄ as an internal standard.

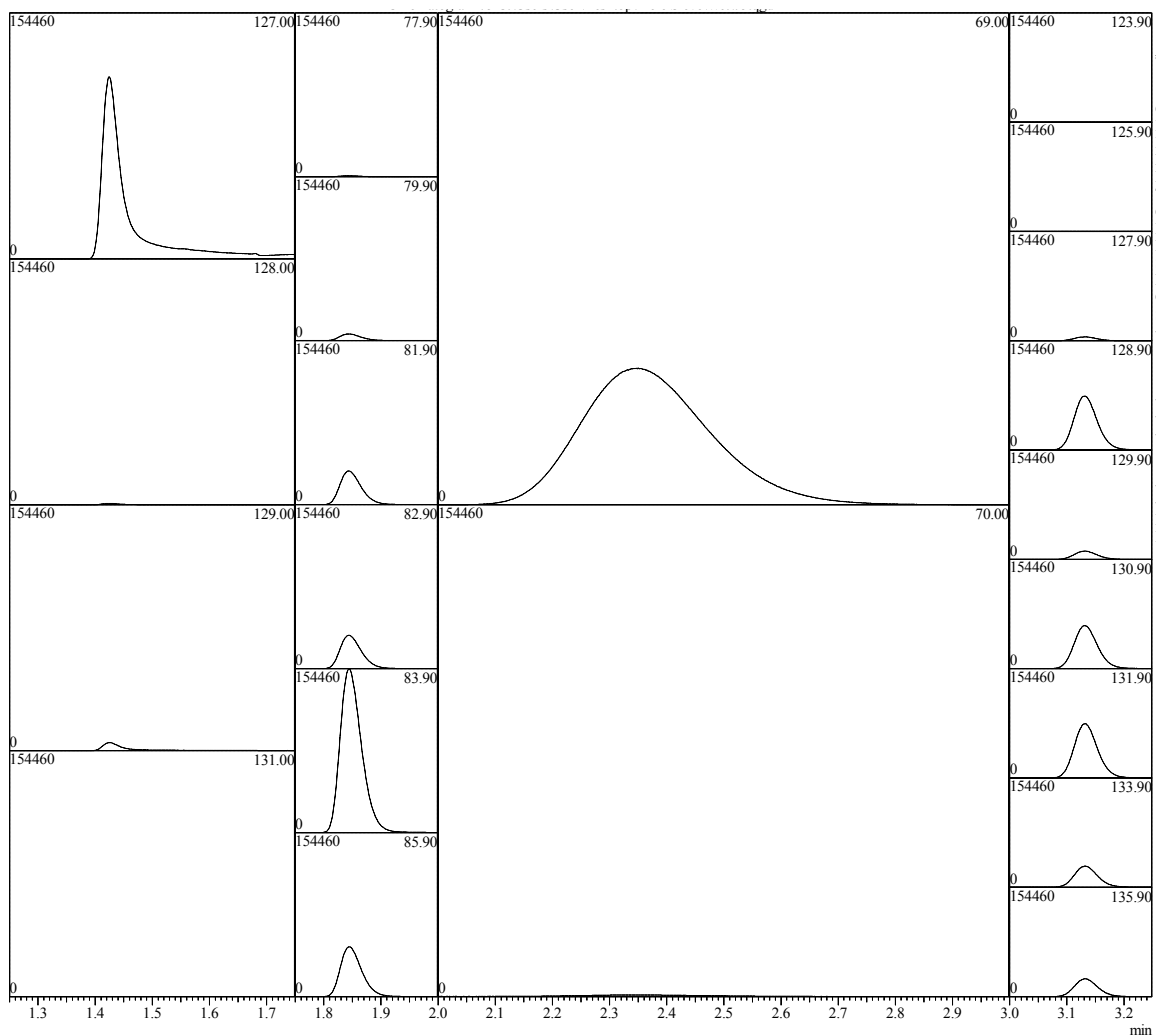


Figure 3.13 Selected Ion Monitoring Chromatogram using a Molecular Sieve

In addition to separating the peaks, enabling higher sensitivity, the peak shape is noticeable more Gaussian for all species but SF_6 . This enables better peak fitting when estimating the areas. As the carrier gas largely entrains SF_6 , its peak is noticeably tailing. This is evidence of a non-linear adsorption isotherm, i.e. some sites within the PLOT column are capable of adsorbing SF_6 and these sites are saturated. It is believed the attempts at quantifying SF_6 at parts per trillion levels did not encounter this difficulty, as there was insufficient analyte to saturate the column.

While the molecular sieve introduced additional error for SF₆, the relative quality of most data improved. In addition, the molecular sieve enables the measurement of low molecular weight gases, such as neon, that would otherwise be obfuscated by the double ionization peaks of heavier gases. As the primary objective is noble gas measurements, this is well satisfied when utilizing the molecular sieve with a CF₄ internal standard.

4. Quasi-Steady-State Diffusivity Measurements

To this point, the focus has been on the theory of transport in porous media, coupled with sorption processes, and the development of a quantitative method for the concentration of noble and inert gas tracers using gas chromatography-mass spectroscopy. As part of the quantitative method, it was shown that samples must be physically withdrawn from the test system and can be processed in about five minutes by GC-MS. While fast by some measures, the number of data points will nevertheless be finite. Therefore, unsteady transient methods cannot be captured effectively by GC-MS.

A pure steady-state system was considered for some time, which would enable repeatedly measurements of the same concentration gradient, enabling a reduction of random error. However, as the quantitative GC-MS method matured improved, elimination of random error became less necessary. In addition, constructing a steady-state diffusion bridge requires multiple mass flow controllers to be balanced in parallel, adding to complexity and cost. A deviation of a single torr may result in advective fluxes on the order of the diffusive flux.

In contrast, the quasi-steady-state approximation (QSSA) requires only passive components. The central premise of the QSSA is that the concentration gradient, while transient, responds quickly to changes in boundary conditions and quickly returns to a linear profile. The boundary conditions, while not controlled precisely, can be held approximately constant with respect to the diffusing medium by utilizing geometric advantages. Within the QSSA methods, the two-bulb apparatus is the most common

experimental design (Marrero and Mason 1972). This method was originally developed at the Clinton Laboratories – latter renamed Oak Ridge National Laboratory – for measuring the self-diffusion coefficient of uranium hexafluoride using isotopically labeled uranium and – coincidentally – a mass spectrometer (Ney and Armistead 1947)

4.1. TWO-BULB APPARATUS

The experimental system consists predominantly of two bulbs of relatively large volume connected by a restrictive bridge over which diffusivity will be estimated. Ordinarily, the bridge is made restrictive by using tube of a narrow diameter. However, extending this method to porous media, the use of a restrictive diameter is unnecessary as the porosity of the media provides this restriction intrinsically.

Consequently, there are three regions in the two-bulb apparatus: the two bulbs that are devoid of porous media, and the packed bridge. Compared with the double-porosity model, the bulbs represent the fractures while the packed bridge represents the matrix. Figure 4.1 depicts the two-bulb apparatus as constructed.

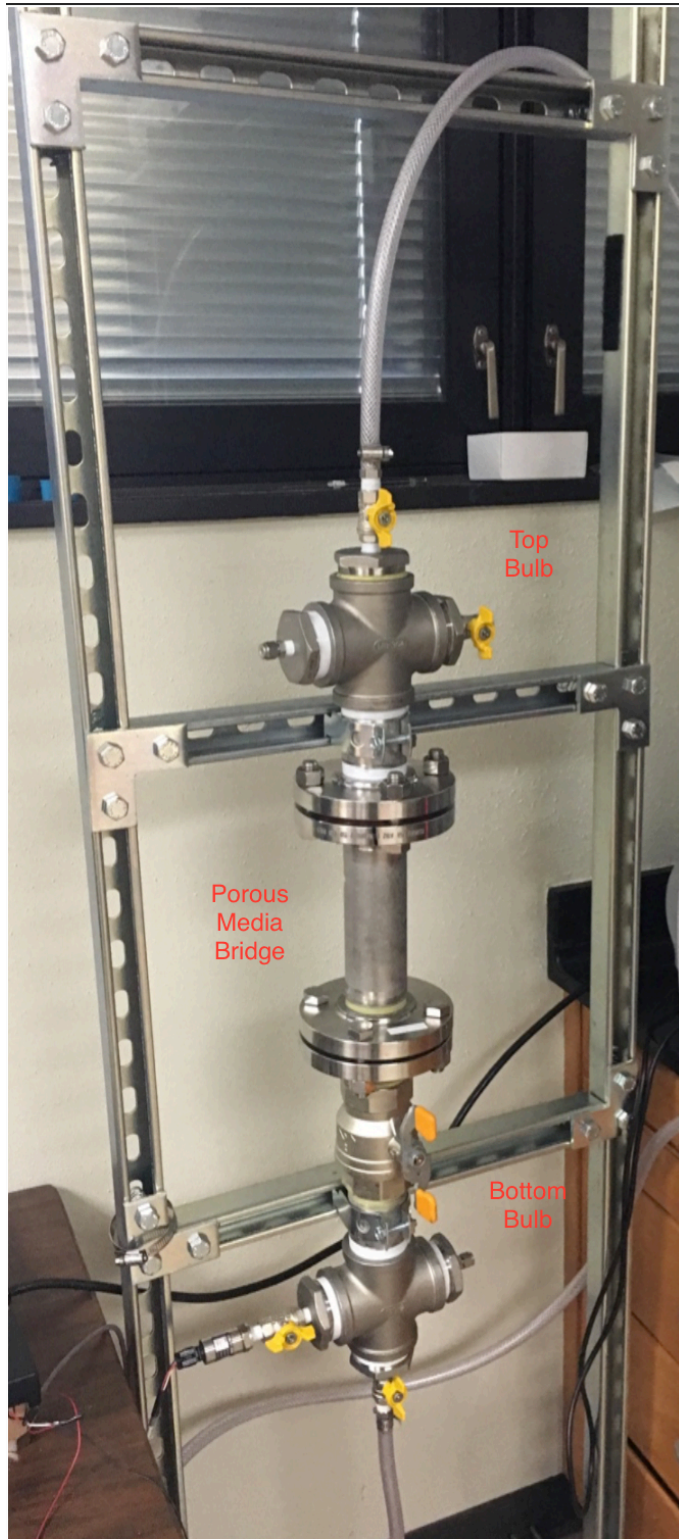


Figure 4.1 Two-bulb Diffusion Apparatus

As there are three distinct regions, the transport equation for this system is logically split into three distinct volumes, labeled V_1 and V_2 for the bulbs and V_b for the bridge. As this system is designed for stable tracers, reaction rates are assumed zero:

$$\frac{\partial}{\partial t} \int_{V_1} c_i dV = - \oint_{V_1} N_i \cdot dS$$

$$\frac{\partial}{\partial t} \int_{V_b} c_i dV = - \oint_{V_b} N_i \cdot dS$$

$$\frac{\partial}{\partial t} \int_{V_2} c_i dV = - \oint_{V_2} N_i \cdot dS$$

Because the system is heterogeneous, the diffusion coefficient is not constant. In the bulbs, the porosity and tortuosity are unity, while they are unknown within the bridge. To solve this system, matching boundary conditions will be required at the interfacial surfaces.

4.1.1. Concentration Profile in the Bridge

The concentration profile in the porous media is of primary importance. Following methods discussed in section 2.14, after accounting for adsorbed or absorbed phases, the differential transport equation is:

$$\frac{\partial c_i}{\partial t} = \frac{\varepsilon(1-S)}{q^2} \frac{D_i}{\kappa_i} \nabla^2 c_i$$

While the system overall is heterogeneous, within the packed media, the diffusion coefficient is assumed to be constant. In addition, because the cylindrical pipe is

impervious to the tracer, applying no flux conditions at the radial surfaces reduces the spatial complexity to one dimension, that which is along the longitudinal axis z . Using the effective diffusivity \mathfrak{D}_i :

$$\frac{\partial c_i}{\partial t} = \frac{\mathfrak{D}_i}{\kappa_i} \frac{\partial^2 c}{\partial z^2}$$

While the boundary conditions of this section are dependent upon conditions in the adjoining bulbs, the length of the system, L , is fixed. Applying Dirichlet boundary conditions at each end requires that the solution be of the form:

$$a_0 + a_1 z + \sum_{n=1}^{\infty} b_n \sin\left(\frac{n\pi}{L} z\right) e^{-\frac{n^2 \pi^2 \mathfrak{D}_i}{L^2 \kappa_i} t}$$

Where a_n and b_n are sets of unknown coefficients. The only assumption necessary is that the effective diffusion coefficient is positive and real valued.

In the quasi-steady state approximation, it is assumed the transient eigenfunctions decay away, leaving a linear concentration profile in the porous media. For this to be valid, the relaxation time in the bridge, τ_b , must be much faster than in the bulbs. While there are an infinite number of transient eigenvalues, only the slowest moving needs to be considered:

$$\tau = \frac{\kappa_i L^2}{\pi^2 \mathfrak{D}_i}$$

Designating the bottom bulb to be V_1 the top bulb to be V_2 , and the positive z direction to be from V_1 towards V_2 , the steady-state coefficients must be:

$$a_0 = c_i(0)$$

$$a_1 = \frac{c_i(L) - c_i(0)}{L}$$

The concentrations referenced here are consequently at the interface with the respective bulbs.

4.1.2. Interfacial Flux

Determining the relaxation time in the bulbs requires a somewhat different approach. Rather than solving these equations in differential form, they will be solved through integration. Assuming zero-flux conditions on all surfaces of the bulbs except on the interface with the bridge, the surface integral can be evaluated as:

$$\oint_{V_1} N_i \cdot dS = N_i \cdot A_1$$

Here, A_1 is the cross-sectional area connecting the bulb to the bridge. An equivalent expression is valid for the second bulb.

At quasi-steady state – that is where material is neither accumulating nor depleting from the bridge – the net influx must equal the net outflux. That is:

$$N_1 \cdot A_1 = -N_b \cdot A_b = -N_2 \cdot A_2$$

As the tracer is dilute, and the system is nearly isobaric and isothermal, the flux in the bridge will be modeled using the Fickian expression from section 2.6:

$$N_i = J_i = -D_i \nabla c_i$$

As only the longitudinal direction has a significant derivative, this flux can be made orthogonal to the apparatus coordinate system by dividing by the tortuosity:

$$N_i = -\frac{D_i}{q} \frac{\partial c_i}{\partial z}$$

However, as already discussed, where the QSSA is valid, the concentration profile is primarily linear. That is:

$$\frac{\partial c_i}{\partial z} = \frac{c_i(L) - c_i(0)}{L}$$

Evaluating the inner product of the flux with the interfacial area reveals:

$$N_1 \cdot A = -\mathcal{D}_i \frac{c_i(L) - c_i(0)}{L} A = -N_2 \cdot A$$

This has the effect of relating the flux in or out of the bulb to the relative concentration of the pair of bulbs.

4.1.3. Coupled Two-bulb System

Given the system has constant geometry; the volume integrals are not time dependent. Assuming the gas is relatively homogeneous within the bulb, the integral of concentration is the scalar product of the bulb concentration and bulb volume. Given the previous evaluation of the surface integral, there only remains a pair of first-order ordinary differential equations:

$$V_1 \frac{dc_1}{dt} = -N_1 \cdot A = \mathcal{D}_i \frac{c_2 - c_1}{L} A$$

$$V_2 \frac{dc_2}{dt} = -N_2 \cdot A = -\mathcal{D}_i \frac{c_2 - c_1}{L} A$$

As this is a system of first-order, linear, differential equations, it can be solved by finding the eigenvalues and associated eigenvectors. Rewriting in matrix-vector notation:

$$\frac{d}{dt} \begin{bmatrix} c_1 \\ c_2 \end{bmatrix} = \mathfrak{D}_i \frac{A}{L} \begin{bmatrix} -\frac{1}{V_1} & \frac{1}{V_1} \\ \frac{1}{V_2} & -\frac{1}{V_2} \end{bmatrix} \begin{bmatrix} c_1 \\ c_2 \end{bmatrix}$$

Solving for the eigenvalues and eigenvectors of a 2x2 matrix is routine. The first eigenvalue is a null value and represents the equilibrium concentration c_∞ . As is consistent with kinetic theory, this solution has a unitary eigenvector, meaning the same equilibrium concentration must be reached in both bulbs.

The second eigenvalue is more complex. It is the product of the matrix coefficient and the reduced volume – analogous to the reduced mass. The associated eigenvector is the proportional to the volume of the opposing bulb. This is necessary to conserve material, as a small change in concentration in a larger volume will induce a large change in a smaller volume.

The resulting solution is then:

$$\begin{bmatrix} c_1(t) \\ c_2(t) \end{bmatrix} = c_\infty \begin{bmatrix} 1 \\ 1 \end{bmatrix} + c_0 \begin{bmatrix} -V_2 \\ V_1 \end{bmatrix} e^{-\mathfrak{D}_i \frac{A}{L} (\frac{1}{V_1} + \frac{1}{V_2}) t} = c_\infty \begin{bmatrix} 1 \\ 1 \end{bmatrix} + c_0 \begin{bmatrix} -V_2 \\ V_1 \end{bmatrix} e^{-\frac{t}{\tau}}$$

The objective of the two-bulb test is to measure the unknown eigenvector coefficients and the non-zero eigenvalue. Because the eigenvalue is composed of a considerable number of parameters, the following definition of the bulb relaxation time will be utilized:

$$\tau = \frac{1}{\mathfrak{D}_i} \frac{L}{A} \frac{V_1 V_2}{V_1 + V_2}$$

For the quasi-steady state approximation to be valid, the bridge relaxation time must be much smaller than the bulb relaxation time. As the bridge is cylindrical, the inner diameter, d , will be used to find the cross-sectional area. Comparing the slowest moving bridge relaxation time to bulb relaxation time:

$$\kappa_i \frac{Ld^2}{4\pi} \left(\frac{1}{V_1} + \frac{1}{V_2} \right) = \frac{\tau_{bridge}}{\tau_{bulbs}} \ll 1$$

All of the components of the effective diffusivity coefficient save the volumetric capacity, factor out. That is, the sorbent capacity is a transient phenomenon and has no bearing on steady state transport. However, with sufficiently large bulbs, the quasi-steady state approximation is valid for sorbent gases.

One limitation of the above approach is that assumes the magnitude of a perturbation is equivalent in all three regions, thus only the relaxation time is necessary. This is true for the experiment with one notable exception, the initial development of the concentration profile. As the initial condition in the bridge is zero throughout, it may take multiple bridge relaxation periods before the linear profile is appropriate. This can be observed in the experimental results as there is a breakthrough time for the low-concentration bulb. After this point, the magnitude of the perturbations on the bulbs and bridge is comparable and the QSSA above is appropriate.

4.2. EXPERIMENTAL APPARATUS

The previous equations are essential to the design of the test system. However, in addition to meeting the QSSA, considerations must be made to the time constraints of the

GC-MS method. As concentrations can only be measured approximately every 15 minutes – allowing for some time to correct for adverse situations during a trial – the test must last long enough to record a satisfactory number of data points. As there are two bulbs from which samples must be drawn, approximately 20 valid data points were desired from each bulb to allow for effective statistical averaging of random error about the mean.

Thereby, the system was designed to have statistically significant measurements over a period of approximately 10 hours. While the GC-MS can detect the tracers at a wide range of concentrations, as the two concentrations converge, the random electronic noise limits the usefulness of this data. Consequently, points measured where there are larger deviations from equilibrium have more statistical significance. As the system decays exponentially, the statistical significance lasts for approximately three time periods. From a design perspective, this imposes the requirement that the relaxation time of no shorter than 3 hours.

To minimize the potential viscous flows induced by injecting a large quantity of a diluted tracer, the tracer was instead diluted within an isolated chamber of the apparatus. Using a quarter-turn ball valve of similar diameter to the connected bulb and bridge allowed for diffusion without undue restriction.

In addition to the geometry, there were additional material design considerations. As the apparatus must not oxidize or undergo galvanic corrosion in the presence of water, stainless steel 310 pipe and pipe fittings were selected throughout. Where stainless steel was unavailable, such as for the valve, nickel-coated brass was chosen for galvanic

compatibility. The pipe threads were sealed using Rector-Seal No. 5 liquid thread sealant. Poor seals were obtained using polytetrafluoroethylene (PTFE) tape, even tape specifically designated for use with stainless steel systems.

While custom components could have been procured, a satisfactory geometry was found using commercially available 2-inch nominal pipe. The bulbs were constructed of 4-way crosses as this increased the volume at the ends while maintaining a constant axial cross-section throughout. Table 4.1 highlights the critical parameters of the apparatus:

Table 4.1 Geometric Parameters of the Two-bulb Apparatus

Parameter	Dimensions
Length	23.0 cm
Inner Diameter	5.25 cm
Volume (bulb 1)	749 cm ³
Volume (valve)	395 cm ³
Volume (bridge)	498 cm ³
Volume (bulb 2)	751 cm ³

While operationally desirable, a limitation of ball valve is that it has a significant void-space volume. As the diffusivity in this void space is large compared with the porous media, this results in a large initial transient as the tracer gases rapidly transport into this space. However, as this time is comparable to the breakthrough time of the bridge, this provided little impact to estimation of the eigenvalues. It does result in an asymmetry in the bulb volumes though.

Utilizing parameters in Table 4.2, the relaxation time of the bridge is approximately one-ninth the relation time of the bulbs. Thus, for perturbations of a similar magnitude, the bridge will reach to a linear profile approximately nine times faster than the bulbs.

$$\frac{\tau_{bridge}}{\tau_{bulb}} = 0.111$$

Because the effective diffusion coefficient in the media is unknown, the bulb decay time is not directly calculable. However, it is bounded by the unobstructed gaseous diffusion coefficient. Using the nitrogen diffusivity correlations at 20°C reported in the Journal for Physical Chemistry Reference Data (Marrero and Mason 1972), 0 lists the minimum possible characteristic times in the unobstructed case:

Table 4.2 Unobstructed Two-bulb Apparatus Time Constants

Gas	Diffusivity (cm ² /s)	τ (min)
Ar	0.190	42.3
Kr	0.148	54.1
Xe	0.122	66.0
SF ₆	0.092	87.5

For each of the diffusivities trials conducted here, the bridge was packed with 10-30 Ottawa sand, which is nearly pure silica sand. As a rough estimate, the effective diffusivity in the porous media used here will be approximately one-tenth to one-quarter of this. Consequently the relaxation time of the bulbs is expected to be between four and ten times these values.

4.3. LINEAR TRANSFORMATION OF CONCENTRATION TO ION COUNT RATIO

Ordinarily, in analytical chemistry, it is the objective to determine the quantity or concentration of a substance in absolute terms. This requires repeated calibrations against a range of prepared standards. However, as the solution to the two-bulb system is linear and homogeneous with concentration, a linear transformation of ion count ratio is

sufficient without the need to explicitly determine the relative response factor. Using the same notation as used in section 3.3.2, the ratio of target ion to internal reference follows:

$$I^{j:r} = m_i^{j:r} c_i + b^{j:r}$$

Solving for an unknown concentration c_i :

$$c_i = \frac{(I^{j:r} - b^{j:r})}{m_i^{j:r}}$$

Substituting this into the two-bulb solution:

$$\begin{bmatrix} I_1^{j:r}(t) \\ I_2^{j:r}(t) \end{bmatrix} = I_\infty^{j:r} \begin{bmatrix} 1 \\ 1 \end{bmatrix} + I_0^{j:r} \begin{bmatrix} -V_2 \\ V_1 \end{bmatrix} e^{-\frac{t}{\tau}}$$

It is shown that both the background concentration and relative response factor are identically balanced. Consequently, rather than performing a set of serial dilutions prior to each experiment and determining the exact concentration, it is sufficient to record only the difference in signal intensity from the initial condition. As the concentration in the bulb is initially known – the volume of the bulb and the quantities of the tracers injected are known – this is sufficient to ensure the concentrations are within the range of linearity. Henceforth, the ion-count ratio will be considered to be numerically equivalent to the measured concentration.

4.4. MAXIMUM LIKELIHOOD ESTIMATE OF EIGENVALUES AND EIGENVECTORS

While seemingly straightforward, fitting the above convergent two-bulb system to experimental data is more precarious than anticipated. The initial method of Ney and

Armistead measured the isotopic enrichment at only one end and, in absence of adsorption or absorption, the equilibrium concentration can be calculated from the initial quantities. The eigenvalue can be found simply by plotting the linear response of one bulb on a semi log scale. While a simple least squares regression is not entirely accurate as the error on each point is inconsistent on a logarithmic scale, it nevertheless provides satisfactory results where the data is well correlated.

However, where a porous media of unknown porosity is present, or where sorption is significant, the equilibrium concentration is unknown. It was initially assumed that measurements could be taken after an extended period of time, thereby determining the equilibrium concentration experimentally. However, measurements taken from the apparatus the day following the test routinely fell either above or below the convergent data points from the day previous. It is likely a combination of systematic errors, including the period of inactivity for the GC-MS and potential permeation from the two-bulb apparatus.

While with a known equilibrium concentration, measurements obtained from each bulb can be fit to exponential curves independently, in the absence of extremely precise measurements of the equilibrium value, the exponential curves must be fit simultaneously to determine the unknown equilibrium value. While an exhaustive search was not conducted, no numerical algorithm was found to be readily available for this system. Consequently, a new approach was developed for this purpose.

Recalling the form of the two-bulb analytical solution:

$$\begin{bmatrix} c_1(t) \\ c_2(t) \end{bmatrix} = c_\infty \begin{bmatrix} 1 \\ 1 \end{bmatrix} + c_0 \begin{bmatrix} -V_2 \\ V_1 \end{bmatrix} e^{-\frac{t}{\tau}}$$

There are essentially four unknowns: c_∞ , c_0V_2 , c_0V_1 , and τ . There are the equilibrium concentration, the scalar components of the eigenvector, and the relaxation time/eigenvalue. Because the analytical model is nonlinear and inhomogeneous with time, an iterative approach must be taken to determine the unknowns. The method proposed is to make initial estimate of the equilibrium concentration, subtract it from the transient data set, and fit the transformed nonlinear but homogeneous data. Let the n th iteration of the transformed transient data set be defined by the n th equilibrium concentration estimate:

$$\begin{bmatrix} c_1^n(t) \\ c_2^n(t) \end{bmatrix} = \begin{bmatrix} c_1(t) \\ c_2(t) \end{bmatrix} - c_\infty^n \begin{bmatrix} 1 \\ 1 \end{bmatrix} = c_0 \begin{bmatrix} -V_2 \\ V_1 \end{bmatrix} e^{-\frac{t}{\tau}}$$

While any number of eigenvalue-eigenvector pairs may fit this solution for an arbitrary estimate of equilibrium concentration, the second aspect of this approach is that the error is minimized. Unfortunately, as the system is not perfectly symmetric, the eigenvectors are not identical and the data sets cannot be simultaneously fit to a singular function and cannot deliver a singular error value.

Instead, the two nonlinear functions will be fit using a maximum likelihood estimate. This yields the minimum error for the iterative curve fit. Rather than accepting the global minimum error, the equilibrium concentration will instead be constrained to values that produce identical eigenvalues for the component functions.

To make an estimate of the eigenvalues, a statistical model must be developed appropriate to the task. First, the error in the measurements is assumed to be

approximately normally distributed and of constant variance in intensity space for each measurement. While some error can be attributed to counting statistics, where the variance is proportional to the square root of the magnitude, experimental observations indicate the sample variance to be far greater than that explainable by counting statistics alone. Furthermore, errors in the measurements appear to be independent of concentration at the levels used here. Therefore, the statistical model for the error in each measurement is assumed to be:

$$y_i = Ae^{Bx_i} + \epsilon_i$$

where y_i is the observation, A and B are the exponential parameters, x_i is the independent variable and ϵ_i is the error. Rearranging:

$$y_i \left(1 - \frac{\epsilon_i}{y_i}\right) = Ae^{Bx_i}$$

This equation can be linearized with the independent variable by taking natural logarithm of each side:

$$\ln(y_i) + \ln\left(1 - \frac{\epsilon_i}{y_i}\right) = \ln(A) + Bx_i$$

As the fractional error is presumed to be small – as the observations would be of minimal use if this were not the case – the logarithm containing the fractional error will be expanded as a Maclaurin series:

$$\ln\left(1 - \frac{\epsilon_i}{y_i}\right) = 0 - \frac{\epsilon_i}{y_i} + \sum_{n=2}^{\infty} \frac{(-1)^n}{n!} \left(\frac{\epsilon_i}{y_i}\right)^n$$

Therefore, the error on the function can be approximated as:

$$\epsilon_i = -y_i(\ln(y_i) - \ln(A) - Bx_i)$$

Using this expression for error, the parameters A and B can be estimated using the maximum likelihood method.

With the assumption that the error is normally distributed – which is expected, as the observed error is the product of a number of random independent processes - the joint probability distribution of N events being observed is:

$$P(A, B) = \prod_{i=1}^N \frac{1}{\sqrt{2\pi\sigma^2}} e^{-\frac{\epsilon_i^2}{2\sigma^2}}$$

The variables A and B will be selected such that they maximize the joint probability of N observations. Rather than maximizing the distribution directly, it is more practical to maximize the logarithm of the joint distribution, which conveniently transforms the product to a summation.

$$Q(A, B) = \ln(P(A, B)) = -\frac{N}{2} \ln(2\pi\sigma^2) - \frac{1}{2\sigma^2} \sum_{i=1}^N \epsilon_i^2$$

For brevity, the following substitutions will be made. $a = \ln \hat{A}$ and $b = \hat{B}$ where the carat connotes the value is the estimated parameter. The maximum can then be found by finding the combination of parameters, a and b , such that the likelihood function has null partial derivatives. That is:

$$\frac{\partial Q}{\partial a} = \frac{1}{\sigma^2} \sum_{i=1}^N y_i^2 (\ln y_i - a - bx_i)^2 = 0$$

$$\frac{\partial Q}{\partial b} = \frac{1}{\sigma^2} \sum_{i=1}^N x_i y_i^2 (\ln y_i - a - bx_i)^2 = 0$$

As the variance is non-zero, it can be removed from the equations. Solving this pair of algebraic equations, the solution for the parameters is as follows:

$$\ln(\hat{A}) = a = \frac{\sum x_i^2 y_i^2 \sum y_i^2 \ln y_i - \sum x_i y_i^2 \sum x_i y_i^2 \ln y_i}{\sum y_i^2 \sum x_i^2 y_i^2 - (\sum x_i y_i^2)^2}$$

$$\frac{1}{\tau} = \hat{B} = b = \frac{\sum y_i^2 \sum x_i y_i^2 \ln y_i - \sum x_i y_i^2 \sum y_i^2 \ln y_i}{\sum y_i^2 \sum x_i^2 y_i^2 - (\sum x_i y_i^2)^2}$$

Having a method for minimizing the residual error on an exponential function, the second challenge is to fit two sets of data – the upper and lower bulbs – such that the eigenvalue is consistent. Defining the error on iteration n to be the difference between the eigenvalues of the scalar components:

$$\Delta B^n(c_\infty^n) = B_1^n(c_\infty^n) - B_2^n(c_\infty^n)$$

where B_1 and B_2 are determined by the MLE method described. The estimated equilibrium concentration satisfies the constraint when the difference is zero.

As the derivative of the function ΔB is unknown and dependent on the distribution of the experimental points, it is not possible to use the Newton-Raphson method. The secant method may produce unstable results, as the function is not guaranteed to be smooth. Since reliability is of greater importance than efficiency, the bisection root-finding method was employed.

Furthermore, because the system is dissipative, B must be negative and it is known that the equilibrium value is bound between any two given measurements. Therefore, the root must to be located between the concentration measurements of closest approach. A slight tolerance was applied to the initial bracket to preclude floating point

exceptions while taking logarithms. These methods were then coded into Octave/MATLAB and are recorded in Appendix A: Quasi-Steady-State Numerical Method.

4.5. NITROGEN STANDARD

A series of trials was conducted utilizing the naturally occurring ^{15}N in the ambient atmosphere, as per the method of section 3.3.3. In this case, the gas chromatography used was the original manufacturer supplied 5% diphenyl/95% dimethyl polysiloxane column of length 30 m and inner diameter 0.25 mm. Consequently, separation of the permanent gas peaks was not without cryogenic temperatures. This method relied solely on the mass spectrometer to separate the species. Consequently, with minimal interactions, the species eluted rather quickly, even with a volumetric flow rate of only 2.4 mL/min and a split ratio of 4:1. All peaks arrived at approximately 2.1 minutes.

Consequently, to avoid saturating the detector each tracer gas was tested in insolation. Trials were conducted using SF_6 , Xe, Kr, and Ar. In all cases 2.5 mL of the tracer gas at approximately 760 torr was injected into the bottom bulb. With an approximate bulb volume of 750mL, this equates to approximately 3300 ppm.

After allowing this chamber to equilibrate, a series of measurements were taken to establish the initial concentration. In all cases, the sample volume was nominally 50 μL . After the ball valve was opened, measurements were taken at the intervals as displayed

on the plots – generally 15 minutes. In all cases, these measurements reflect the ion-count ratio to the nitrogen m/z 29 peak, normalized against the initial high concentration bulb.

4.5.1. Results

The results for each of these tests are displayed most efficiently by plotting the current concentration over initial concentration versus time. As the least diffusive gas, this test was conducted over 14 hours. Figure 4.2 displays the results, which demonstrate the relatively smooth exponential decay to equilibrium. As predicted there is a large transient from the high concentration bulb as the gas rapidly diffuses into the bridge. In addition, there is a small breakthrough time of 30 minutes. As indicated, the curves were fit to data taken only after 60 minutes.

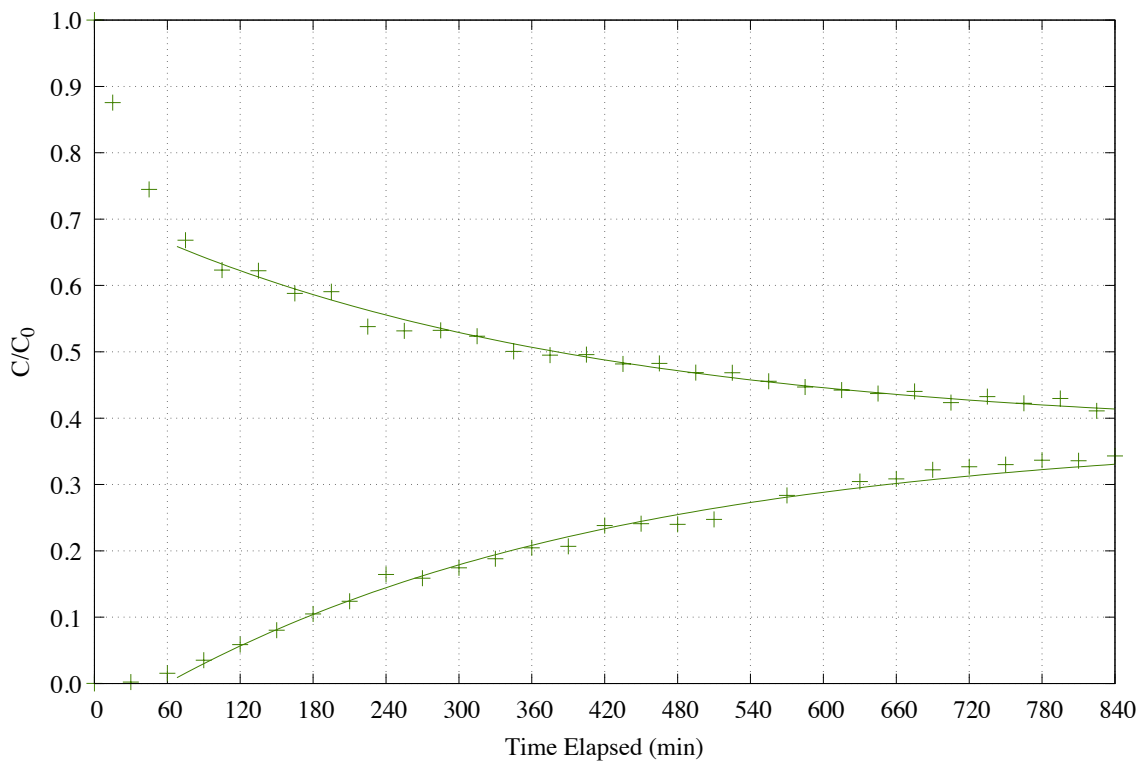


Figure 4.2 Sulfur Hexafluoride Trial

The validity of the QSSA approximation is apparent when viewing the same data on a semi-logarithmic plot – as shown in Figure 4.3. The slope is representative of the eigenvalue – which is the reciprocal of the relaxation time. The different y-intercepts are caused by the asymmetric in the bulb volumes and are commensurate with the eigenvector.

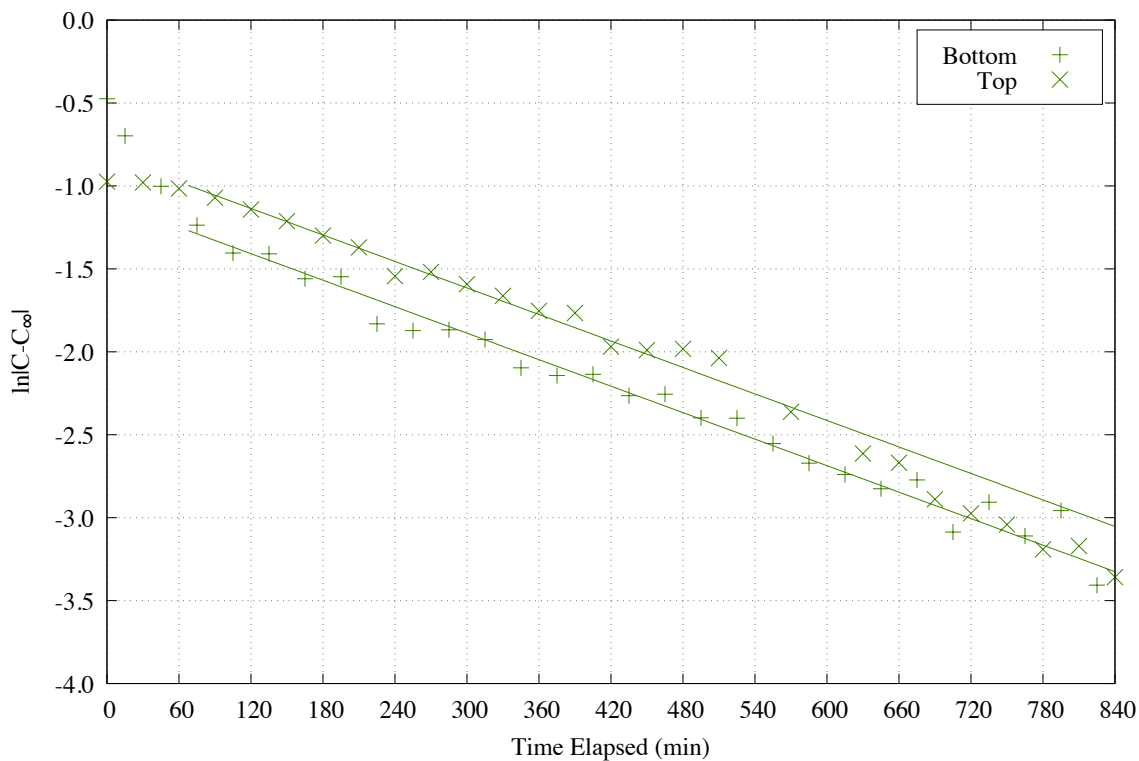


Figure 4.3 Semi-logarithmic Sulfur Hexafluoride Trial

As viewed of a semi-logarithmic scale, the quality of the data degrades after the third relaxation period. As the fit was weighted to minimize the error on a linear scale, points measured later in the test have less significance than those points earlier in the trial. The estimated relaxation time from this plot is 375.6 min, converging at 37.77% and with an asymmetric eigenvector of 1.313. The numerical results for this and the following single-gas trials will be compiled in the analysis.

The xenon trial had somewhat better agreement with theory than sulfur hexafluoride; these results are plotted in Figure 4.4. It is postulated that, having done

recent maintenance on the syringe and the septa, the nitrogen variance decreased, resulting in a very good qualitative fit.

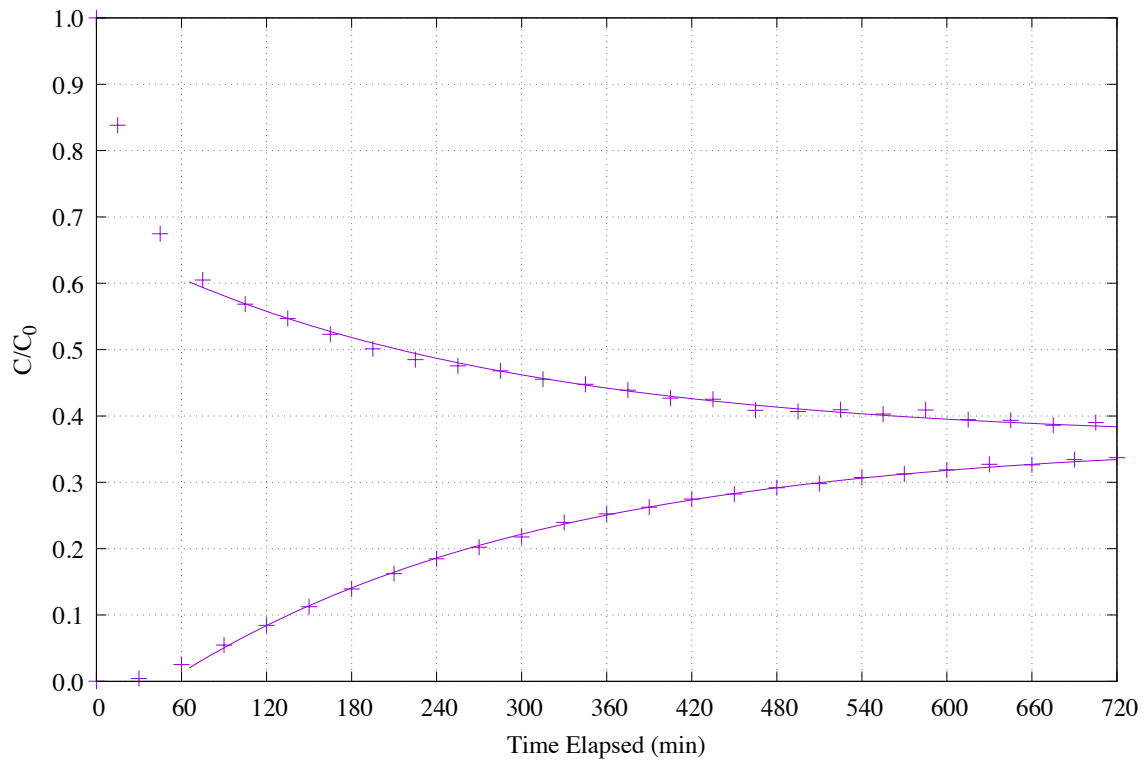


Figure 4.4 Xenon Trial

The improved fit is also clear on a semi-logarithmic scale. The data is plotted against the same fit parameters in Figure 4.5. Here, the relaxation time decreased to 264.9 min, the system converged at 36.35%, slightly lower than SF_6 , and the asymmetry was somewhat greater at 1.438.

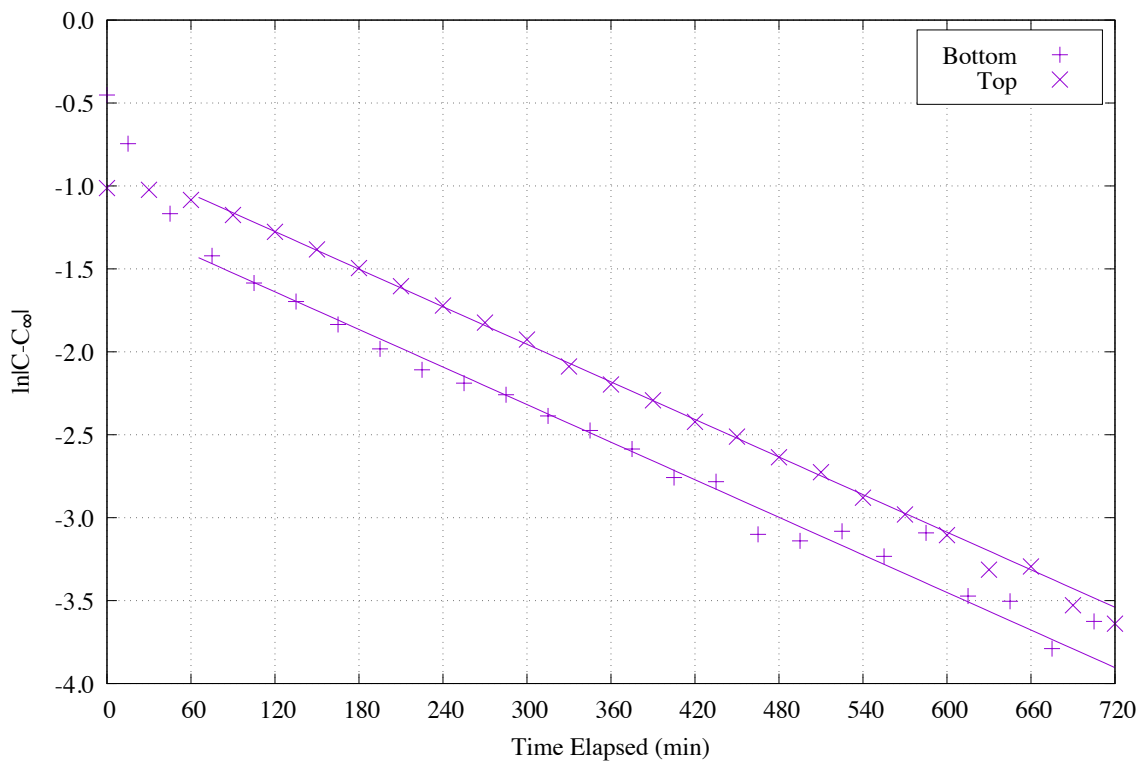


Figure 4.5 Semi-logarithmic Xenon Trial

In contrast to the xenon results, where the nitrogen method functions well, the krypton results highlight the vulnerability of this method to air inclusions. The deviance between the measured points and the two-bulb model, as shown in Figure 4.6, is far greater and inconsistent compared with the Xe and SF₆ trials.

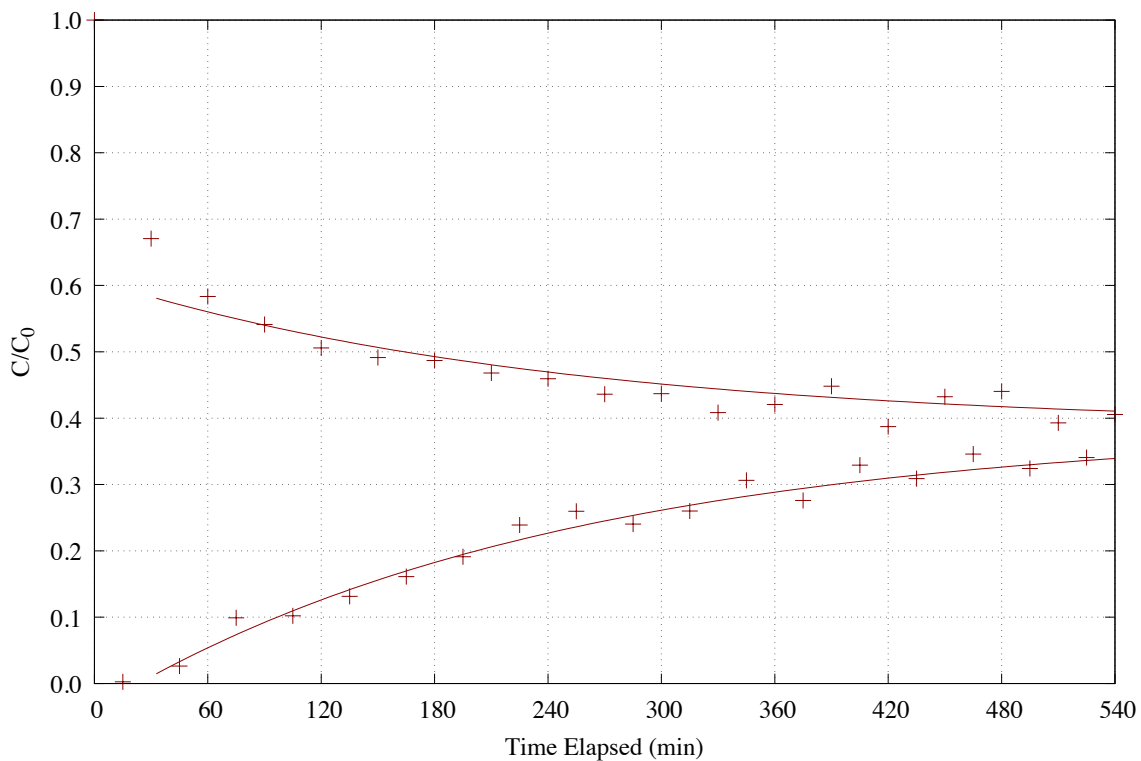


Figure 4.6 Krypton Trial

As two different syringes were used, the variance may not be identical between datasets if there is a systematic error. As it so happened, the lower concentration data had better agreement with the model. Here, the slope for the high concentration dataset is far too flat. It is conjectured the inclusion of excessive air caused the nitrogen counts to spike – resulting in a rapid decrease in the calculated krypton concentration.

Viewed on semi-logarithmic scale – see Figure 4.7 – the relaxation time is far too long at 245.0 min, roughly that of xenon. In addition, the asymmetry was far greater at 1.907. This is evident graphically by the large separation between the top and bottom

curves. It did converge at a reasonable value of 38.60%, but this value is the least adversely affected by erroneous points early in the trial.

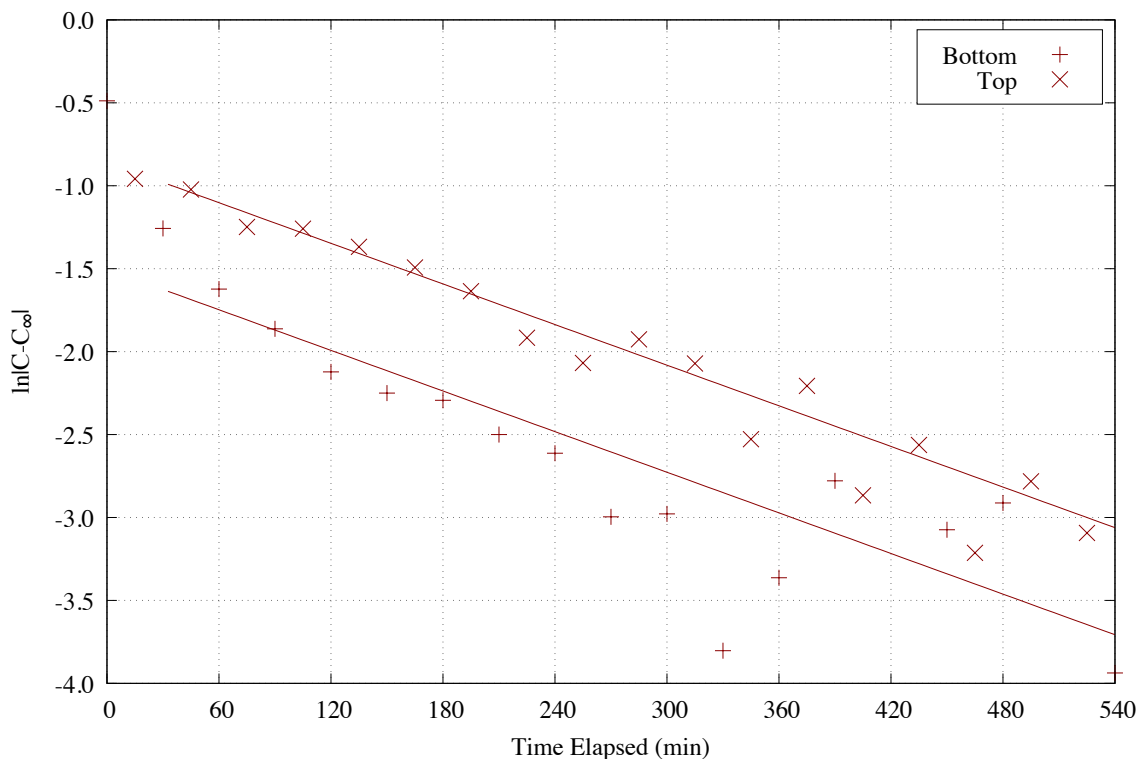


Figure 4.7 Semi-logarithmic Krypton Trial

Measuring the diffusivity of argon in air required a slight modification from the previously discussed species. As ordinary atmospheric air contains approximately 9302-ppm ⁴⁰Ar, it is not possible to significantly perturb the ⁴⁰Ar concentration throughout the apparatus without also increasing the pressure of bottom bulb significantly. However, because a mass spectrometer was used, it is possible to track the much more isotope ³⁶Ar. As its naturally occurring background is only 31 ppm, a similar 2.5-mL injection of enriched ³⁶Ar is sufficient to overcome the background levels. Of course, as ³⁶Ar has a

significantly lower reduced mass with nitrogen and oxygen, its diffusivity is also affected. The measured data as well as the model fits are shown in Figure 4.8:

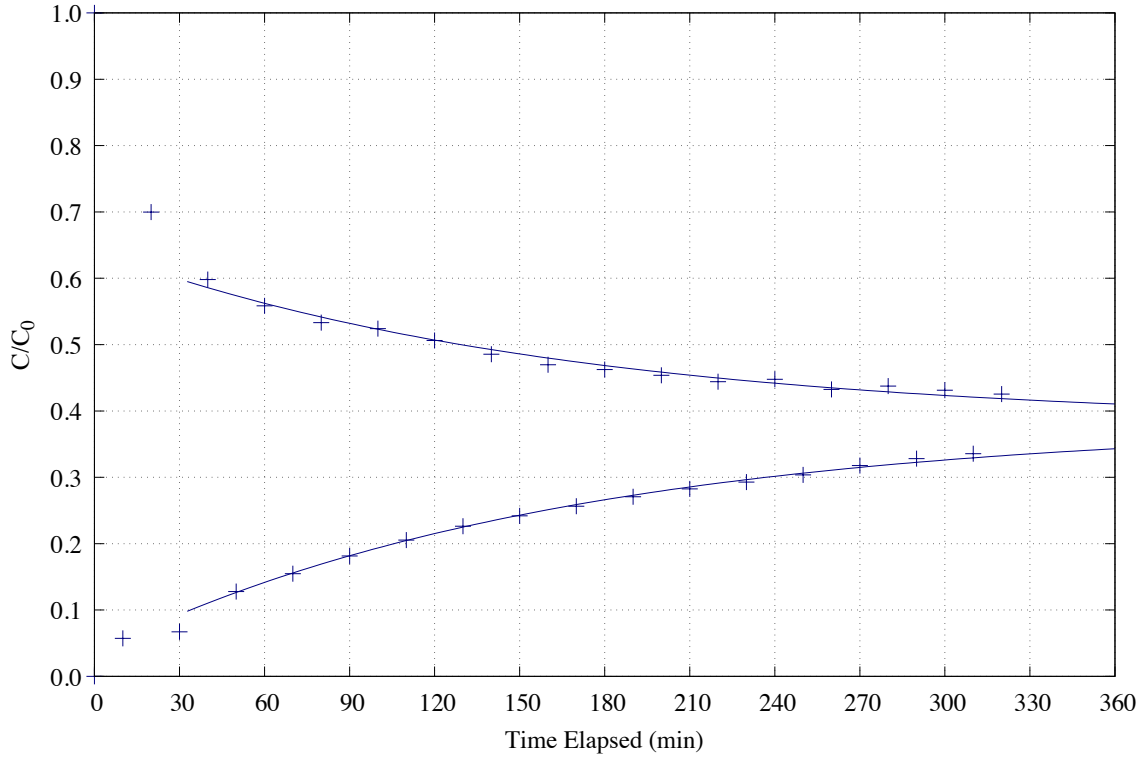


Figure 4.8 Argon Trial

As anticipated, the relaxation time of ^{36}Ar is significantly shorter than that of the other noble gases. The initial breakthrough period was exceedingly fast, making it difficult to ascertain where data should begin to be applied. Due to the brief duration of the trial, samples were collected on a 10-minute interval rather than the typical 15 minutes. Similarly, the data and model fits are plotted on a semi-logarithmic scale in Figure 4.9.

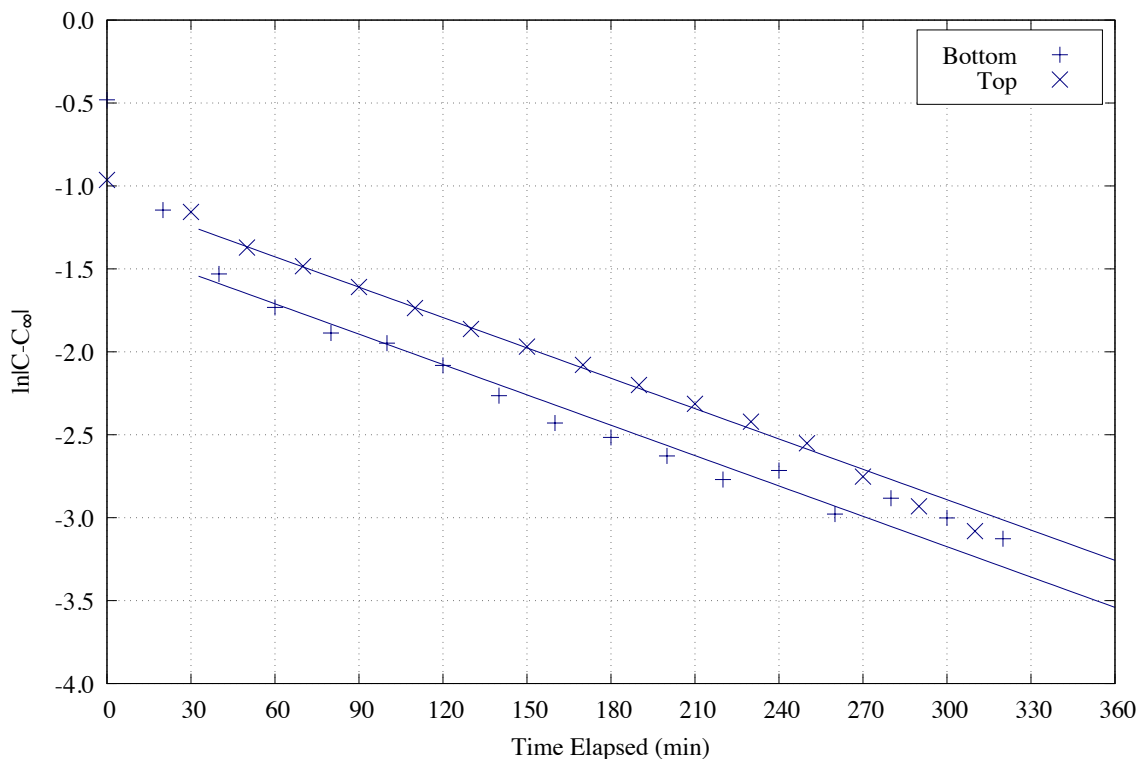


Figure 4.9 Semi-logarithmic Argon Trial

Again, the quasi-steady state model appears to be adequate for even this much more rapidly diffusing gas. The relaxation period observed was 163.9 min. The asymmetry was 1.328, and convergence was reached at 38.16%

4.5.2. Analysis

Of primary importance are the estimates for the eigenvalues/relaxation times, from which estimates of diffusivity can be made. However, the degree of asymmetry in the eigenvector – reported here as the ratio of the apparent volume of the larger bulb and valve over the top valve – also provides some indication as to the accuracy of the test. Finally, the ratio of the estimated equilibrium concentration over initial concentration has

additional value that will also be discussed. The compiled analytical parameters are reported in the following table:

Table 4.3 Two-bulb Results Utilizing ^{15}N

Gas	$\tau(\text{min})$	V_1/V_2	C_∞/C_0
^{36}Ar	163.9	1.328	0.3816
Kr	245.0	1.907	0.3860
Xe	264.9	1.438	0.3635
SF_6	375.6	1.313	0.3777

The most direct application of the relaxation time is to calculate the effective diffusivity without according for sorption effects. Rearranging the expression for relaxation time in section 4.1.3 to express diffusivity as a function of relaxation time and measurable parameters:

$$\mathfrak{D}_i = \frac{1}{\tau} \frac{L}{A} \frac{V_1 V_2}{V_1 + V_2}$$

As the media was dry, the saturation must be zero. Utilizing the system parameters from 0, the product of the diffusivity, porosity, and tortuosity can be found. These will then be compared to nitrogen diffusivities for the corresponding species – after adjusting ^{36}Ar for its reduced mass versus ^{40}Ar :

Table 4.4 Estimated Diffusivities and Porous Media Factors utilizing ^{15}N

Gas	$\tau(\text{min})$	$\frac{\varepsilon}{q^2} D_i (\text{cm}^2/\text{s})$	$D_{i,N_2} (\text{cm}^2/\text{s})$	$\frac{\varepsilon}{q^2}$
^{36}Ar	163.9	0.0490	0.194	0.252
Kr	245.0	0.0328	0.148	0.221
Xe	264.9	0.0303	0.122	0.249
SF_6	375.6	0.0214	0.092	0.233

From this table, it appears that the effect of porosity-tortuosity is not quite evenly applied to each species. However, as the krypton data is suspect, and argon and xenon values are very close and the best data sets, this is not sufficient evidence to suggest the porosity-tortuosity model is incorrect. The magnitude of the deviation in porosity-tortuosity for SF₆ from the well-behaved noble gases was less than 10%, and, given the dataset was not flawless, within reasonable bounds for error.

However, another possible explanation is that the procedure of flushing the apparatus between trials may have perturbed the unconsolidated porous media. With the intent of removing any adsorbed gases, the system has been drawn down to laboratory vacuum and, unexpectedly, the silica sand compacted under vacuum. The relaxation times observed prior to noticing this deviation were at least twice the reported values. After flushing the system with compressed air, the system restored to similar, though not exact values. From this, it was concluded that porosity-tortuosity should not be treated as a strict constant parameter in unconsolidated systems.

These observations show the largest deviation, particularly for krypton. To a first approximation, the asymmetric should be the volume of the bulb and valve of the lower bulb vs. the volume of the upper bulb. However, this ratio is 1.523, well above the observed eigenvector for each gas except krypton. In reality, the bridge has a non-zero capacity due to both pore spaces and adsorption. Any material stored near the ends of the bridge may act to increase the capacity of the bulb, driving the asymmetry closer to unity. With no clear means to calculate sorption from this, the only conclusion that can be made is that the krypton data is out of allowable limits.

This final parameter may contain the most significant data. Presuming the system is closed, and the combined quantity of the 50- μ L samples is negligible or at least comparable, each gas should converge to the same equilibrium fraction. Viewed from another perspective, the initial bulb volume divided by the equilibrium fraction yields an apparent volume, \tilde{V} . As the bulb volume is relatively well known, this can easily be calculated.

$$\tilde{V} = V_1 \frac{C_0}{C_\infty}$$

Xenon has in particular converged to a noticeably lower fraction of initial concentration. Omitting krypton, as the measurements were spurious, argon is presumably the most representative of the pore volume alone, based on polarizability and solubility trends. Differences in the apparent volume of xenon and sulfur hexafluoride versus argon are then, presumably, due to adsorption. Assuming a porosity of approximately 0.25, and a grain density of 2.65 g/cm³, there is then approximately 988 g of Ottawa sand packed in the column. Converting to units of mL at STP per g per torr, the estimates of the adsorption isotherms are shown in Table 4.5:

Table 4.5 Apparent Volumes and Adsorption using Nitrogen

Gas	C_∞/C_0	$\tilde{V}(\text{cm}^3)$	$\tilde{V}_i - \tilde{V}_{Ar}(\text{cm}^3)$	$K_i(\text{cm}^3\text{@STP/g/torr})$
³⁶ Ar	0.3816	1963		
Xe	0.3635	2061	98	1.21E-4
SF ₆	0.3777	1983	20	2.51E-5

While more precise measurements will be shown in chapter 5, these measurements are a plausible order of magnitude. Consequently, nearly 5% of the xenon

is plausibly adsorbed within the diffusion bridge compared with approximately 1% of the SF₆.

4.6. CARBON TETRAFLUORIDE STANDARD

To get a clearer picture, the analytical method and experimental procedure were revised a final time. To preclude changes in the structure of the unconsolidated media, the trials would be conducted simultaneously. As molecular sieve column was installed to separate the gas species and improve sensitivity. Finally, non-atmospheric internal standard, carbon tetrafluoride, was utilized to reduce the impact of sporadic air inclusions.

Using the revised procedures, the experiment was conducted three times, monitoring Xe, Kr, and SF₆ versus the CF₄ internal reference. Again, 50- μ L aliquots were used. As the test and results are very similar, they will be discussed in parallel.

4.6.1. Results

As there is significant quantity of data to list for the three trials with three tracer species, it is best expressed in graphical form. Figure 4.10 shows the measured data for each species and their respective model fits for the first trial.

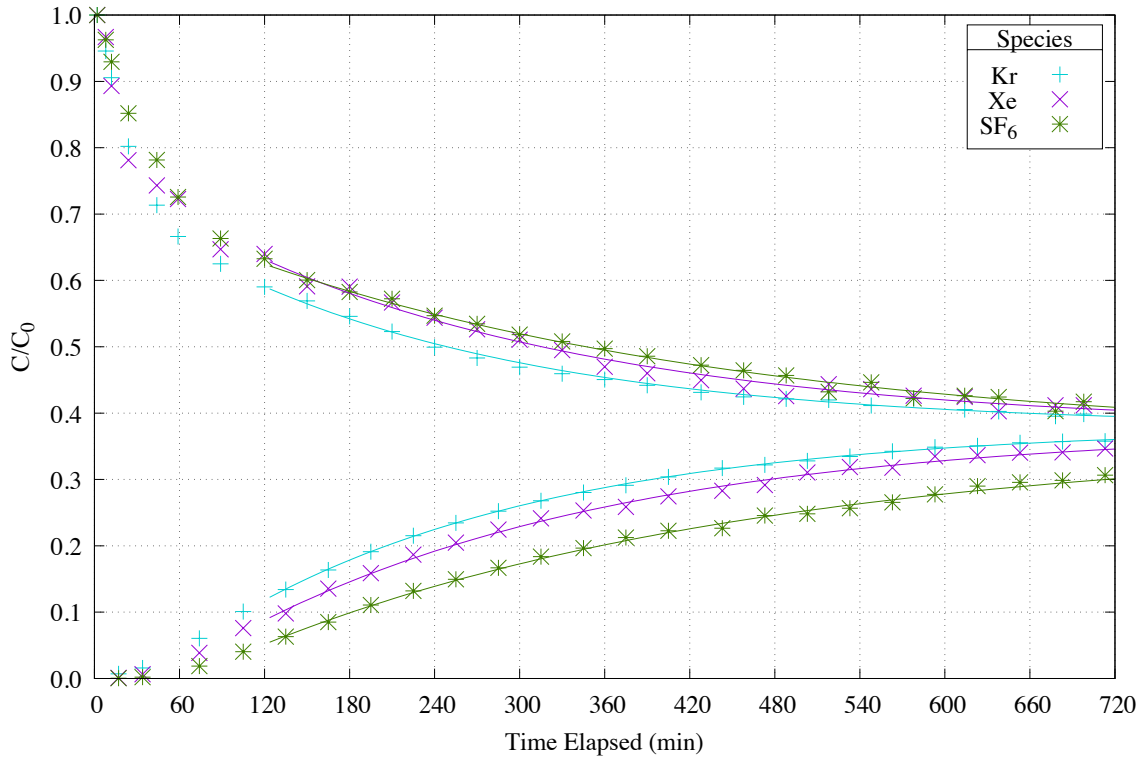


Figure 4.10 Trial 1: Concurrent Diffusion of Kr, Xe, and SF₆

The prominent difference between the three tracers species is the rate at which they reach their asymptotical concentration. Because the diffusivity of krypton is the greatest, it follows the narrowest path. Conversely, sulfur hexafluoride converges the most slowly and follows the outermost path. While the three tracer species converge at a similar concentration, it is not identical. Figure 4.11 and Figure 4.12 similarly show the data and model fits for the second and third trials of the same test.

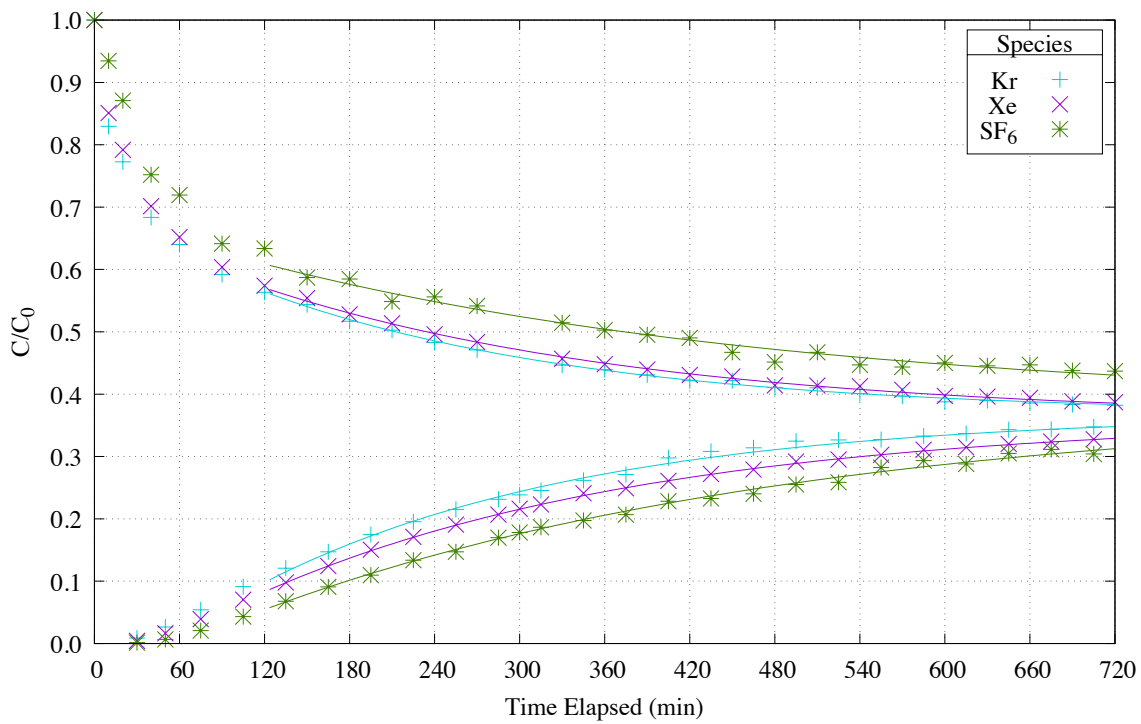


Figure 4.11 Trial 2: Concurrent Diffusion of Kr, Xe, and SF_6

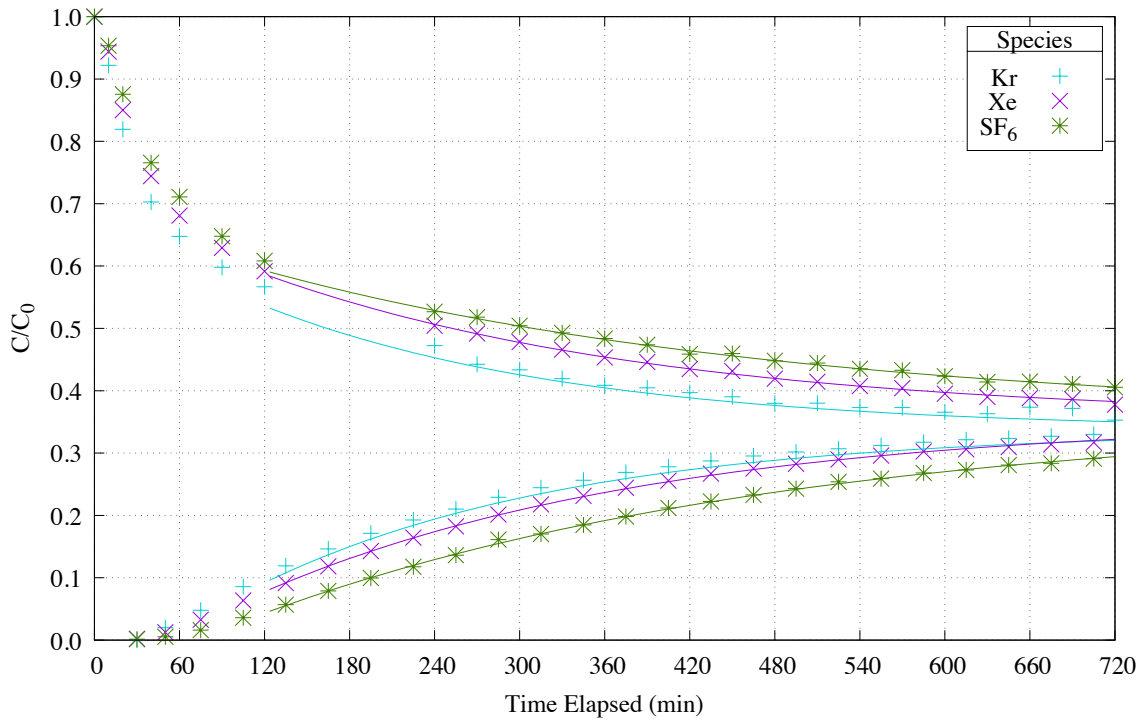


Figure 4.12 Trial 3: Concurrent Diffusion of Kr, Xe, and SF_6

Occasionally, syringe malfunctions resulted in brief omissions of data points, notable between 120 and 240 minutes on the third trial. While the quality of the curve fits was no better than in the well-performing nitrogen standard trials, this method proved to be far more resilient and recoverable after such malfunctions

4.6.2. Analysis

Having already discussed the implications of the key parameters in Section 4.5.2, the compiled relaxation time, asymmetry, and equilibrium fractions are listed in Table 4.6. For comparison purposes, the same parameters from the nitrogen tests are included as well.

Table 4.6 Eigenvalues and Eigenvectors from Concurrent Diffusion Trials

Gas	Trial	$\tau(\text{min})$	V_1/V_2	C_∞/C_0
Kr	1	229.6	1.238	0.3796
	2	232.9	1.385	0.3686
	3	222.5	1.232	0.3469
	Mean CF ₄	228.3	1.285	0.3650
	¹⁵ N	245.0	1.907	0.3860
Xe	1	269.2	1.138	0.3771
	2	278.6	1.331	0.3613
	3	281.8	1.197	0.3551
	Mean CF ₄	276.5	1.222	0.3645
	¹⁵ N	264.9	1.438	0.3635
SF ₆	1	359.0	1.156	0.3588
	2	387.7	1.448	0.3823
	3	376.7	1.345	0.3583
	Mean CF ₄	373.4	1.302	0.3706
	¹⁵ N	375.6	1.313	0.3777

Here, the mean SF₆ and Xe relaxation times are comparable, though not identical to the isolated cases. The mean Kr data was significantly shorter, as was expected. The strong asymmetry also was not present for these Kr trials.

As it has been noted that the effective porosity-tortuosity had not appeared to be a strict constant after flushing with compressed air, the effective diffusivity was calculated separately and then compared against the diffusivity with nitrogen to estimate the porosity-tortuosity. The results are listed in the following Table 4.7:

Table 4.7 Diffusivities Measured using Carbon Tetrafluoride

Trial	Gas	τ (min)	$\frac{\varepsilon}{q^2} D_i$ (cm ² /s)	$\frac{\varepsilon}{q^2}$
1	Kr	229.6	0.0400	0.270
	Xe	269.2	0.0341	0.280
	SF ₆	359.0	0.0256	0.279
2	Kr	232.9	0.0394	0.266
	Xe	278.6	0.0329	0.270
	SF ₆	387.7	0.0237	0.258
3	Kr	222.5	0.0413	0.279
	Xe	281.8	0.0326	0.267
	SF ₆	376.7	0.0244	0.265

While perhaps not a strict constant after flushing with compressed air, the variation the calculated porosity-tortuosity factor varied only slightly between the trials. Furthermore, there was no consistent trend of deviations from the mean amongst the tracer species. Therefore, no significant Knudsen or surface diffusion was detected in this media. The small variations, less than 5%, are more likely explainable by random experimental error than any selective transport mechanisms

In contrast to the trials conducted using nitrogen, the asymmetry in the eigenvector was much reduced. As the system geometry has not changed, this is more

likely evidence of a systematic bias in the nitrogen standard method. As the species were co-eluting prior to installation of the molecular sieve, there may have some slight non-linearity in the signal response at the ion detector. These values are compiled in Table 4.8.

Table 4.8 Asymmetry Measured using Carbon Tetrafluoride

Gas	Trial	V_1/V_2
Kr	1	1.238
	2	1.385
	3	1.232
	Mean CF ₄	1.285
	¹⁵ N	1.907
Xe	1	1.138
	2	1.331
	3	1.197
	Mean CF ₄	1.222
	¹⁵ N	1.438
SF ₆	1	1.156
	2	1.448
	3	1.345
	Mean CF ₄	1.302
	¹⁵ N	1.313

Similarly to the nitrogen reference trial, the xenon converged at a slightly lower point than the sulfur hexafluoride. Krypton also converged near but above the xenon equilibrium fraction. Sulfur hexafluoride continued to converge at a concentration less than the ³⁶Ar value, but above both heavy noble gases. Again, the fraction adsorbed ranged between 2% and 5% of total tracer quantities. The numerical values are listed in Table 4.9:

Table 4.9 Apparent Volumes and Adsorption using Carbon Tetrafluoride

Gas	C_∞/C_0	$\tilde{V}_i(\text{cm}^3)$	$\tilde{V}_i - \tilde{V}_{Ar}(\text{cm}^3)$	$K_i(\text{cm}^3\text{@STP/g/torr})$
Kr	0.3650	2052	89	1.11E-04
Xe	0.3645	2055	92	1.14E-04
SF ₆	0.3706	2021	58	7.22E-05

While these estimates provide a rough estimate of the adsorption isotherm, and additional evidence, this apparatus was designed to primarily measure the diffusivity. A more direct measurement of these quantities is warranted.

4.7. WET POROUS MEDIA

The previous sections have discussed the system in a dry environment. The presence of water retained in the pores presents an additional challenge as it introduces a third phase. Logically, the relaxation time will be extended as some of the pore volume is occupied by the liquid phase. This phase may also alter the tortuosity of the gas phase. In addition, water is in a vapor-liquid equilibrium at ambient conditions, thereby altering the composition of the air. Finally, the liquid phase is capable of absorbing the tracer gases, resulting in inconsistent apparent volumes for each species.

This trial was conducted using the same quantitative method as the previous trials with carbon tetrafluoride. The two-bulb test was repeated following the same procedures as the dry CF₄ trials, but with the addition of 50 mL of deionized water to the packed portion of the column. As the volume of sand in the column is approximately 500 mL, this represents 10% volumetric water content or, assuming 25% porosity, 40% saturation.

Even if the precise dry porosity were known, it would not be identical to the wetted system porosity as the surface tension of water distorts the packing of sand.

4.7.1. Results

The quality of the data utilizing a CF_4 internal standard was good despite the expected deleterious effect of humidity on the molecular sieve. The data and curve fits are shown in Figure 4.13.

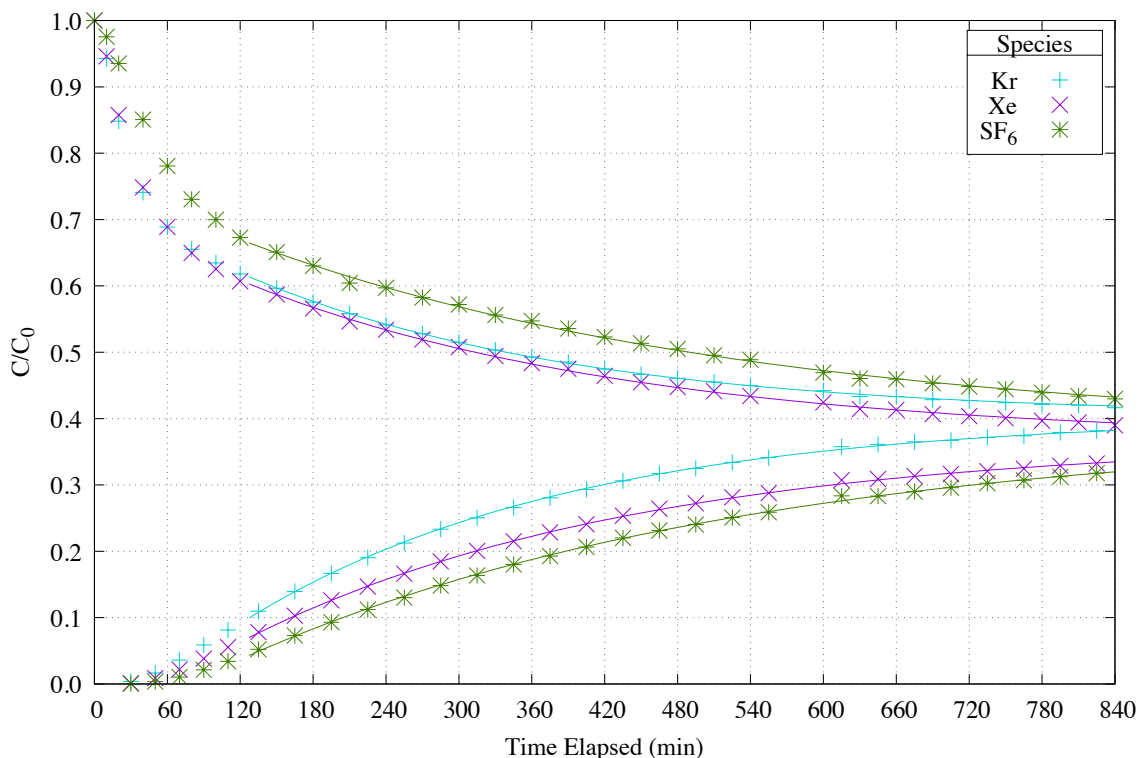


Figure 4.13 Two-bulb Wet Test Results

While similar to the dry trial results, the time of the test was extended to fourteen hours to accommodate the increased relaxation time. Some deviations had occurred early in the SF_6 as the shape of the SF_6 chromatographic peak had broadened under the influence of repeated humid injections. Thereby, the equilibrium fraction of SF_6 may be

slightly off, but no such deviation occurred for the well-formed chromatographic peaks of Kr or Xe. Consequently, there is a higher degree of confidence in the shift from Kr and Xe equilibrium fractions.

4.7.2. Analysis

Using the same analytical method as in the dry case, the eigenvalues obtained in the dry system were as follows in Table 4.10:

Table 4.10 Two-bulb Wet Result Eigenvalues and Eigenvectors

Species	$\tau(\text{min})$	V_1/V_2	C_∞/C_0
Kr	270.5	1.451	0.4039
Xe	323.6	1.191	0.3677
SF ₆	416.9	1.266	0.3810

In contrast with the dry results, the diffusivity ratios obtained here may deviate from comparable values with nitrogen. The diffusivity and effective porosity-tortuosity-saturation were calculated and tabulated in Table 4.11.

Table 4.11 Effective Diffusivity of Wet vs. Dry Trials

Trial	Gas	$\tau(\text{min})$	$\mathcal{D}_i \text{ (cm}^2/\text{s)}$	$\frac{\varepsilon(1-S)}{q^2}$
Dry	Kr	228.3	0.0352	0.237
	Xe	276.5	0.0290	0.239
	SF ₆	373.4	0.0215	0.234
Wet	Kr	270.5	0.0297	0.200
	Xe	323.6	0.0248	0.204
	SF ₆	416.9	0.0193	0.210

While the effective porosity-tortuosity-saturation factor was reduced by approximately 15%, this is a far from the expected 40% reduction due to saturation. At a

minimum, 50-mL of water was added to the bridge and was visually confirmed to have been retained. While the porosity was not precisely known, it was certainly less than 50% based on the dry effective diffusivities. It must be concluded that, while the water saturation decreased the effective diffusivity, it was not linearly so. There is likely a more complex interaction with tortuosity where the water preferentially adheres to tortuous paths that had play a less significant role in gas transport.

In addition to the liquid phase altering the geometry of the gas volume, the vapor phase of water will alter the gas phase diffusivity according to its humidity. If the full Stefan-Maxwell approach is utilized, water vapor becomes an additional component of the gas phase. But, as the tracer is dilute, the Fickian model was utilized. However, to find the effective diffusion coefficient in a homogeneous mixture, the diffusion coefficients must be weighted by their molar fractions. As described in section 2.6:

$$\frac{1}{D_i} = \frac{1}{D_{iK}} + \sum_{i=1, i \neq j}^N \frac{y_i}{D_{i,j}}$$

Because the molecular weight of water is significantly lower than that of nitrogen, oxygen, and argon, the Fickian diffusivity will increase with increasing water vapor content. Provided with an observed air diffusivity, the diffusivity of a dry air mixture can be approximately scaled with humidity as:

$$\frac{1}{D_i} = \frac{1}{D_{iK}} + \left(\frac{y_{N_2}}{D_{i,N_2}} + \frac{y_{O_2}}{D_{i,O_2}} + \frac{y_{Ar}}{D_{i,Ar}} + \dots \right) + \frac{y_{H_2O}}{D_{i,H_2O}} = \frac{1}{D_{iK}} + \frac{1 - y_{H_2O}}{D_{i,Air}} + \frac{y_{H_2O}}{D_{i,H_2O}}$$

Neglecting the Knudsen diffusion, if the diffusivity with water vapor is presumed to follow Graham's Law and is inversely proportional to the square root of the reduced mass, the effect of increasing humidity on the diffusivity is approximately:

$$D_i = \frac{D_{i,air}}{(1 - y_{H_2O}) + y_{H_2O} \sqrt{\frac{\mu_{i,H_2O}}{\mu_{i,air}}}}$$

Following this approach, Table 4.12 lists the molecular weights of the gas species and the root ratio of the reduced masses with air and water vapor:

Table 4.12 Reduced Mass Ratio of Tracer Species with Water Vapor and Atmosphere

Component	Molecular Weight	$\sqrt{\frac{\mu_{i,air}}{\mu_{i,H_2O}}}$
H ₂ O	18.00	
Air	28.94	
Ar	39.95	1.163
Kr	83.79	1.205
Xe	131.3	1.224
SF ₆	146.1	1.228

As the reduced mass ratio is greater than one, the diffusivity of the tracer species in pure water vapor is expected to be between 16% and 23% higher than in dry air. And, while there is a slight variation in the effect with the molecular weight of the tracer, the difference is negligible between xenon and sulfur hexafluoride. As the molecular weight of these components is already dramatically greater than air, the resulting reduced mass ratio is converging on the ratio of the molecular weights of air to water vapor – 1.268.

This likely contributes to the apparent reduced effect of water saturation. However, the magnitude of this effect is capped at the maximum water vapor content at

ambient temperatures. The vapor pressure of water can be expressed using Antoine's equation:

$$\log_{10}\left(\frac{P}{\text{bar}}\right) = A - \frac{B}{\frac{T}{K} + C}$$

Using coefficients calculated by NIST (Bridgeman and Aldrich 1964), Figure 4.14 illustrates the maximum water vapor content – i.e. 100% relative humidity – over a range of temperatures:

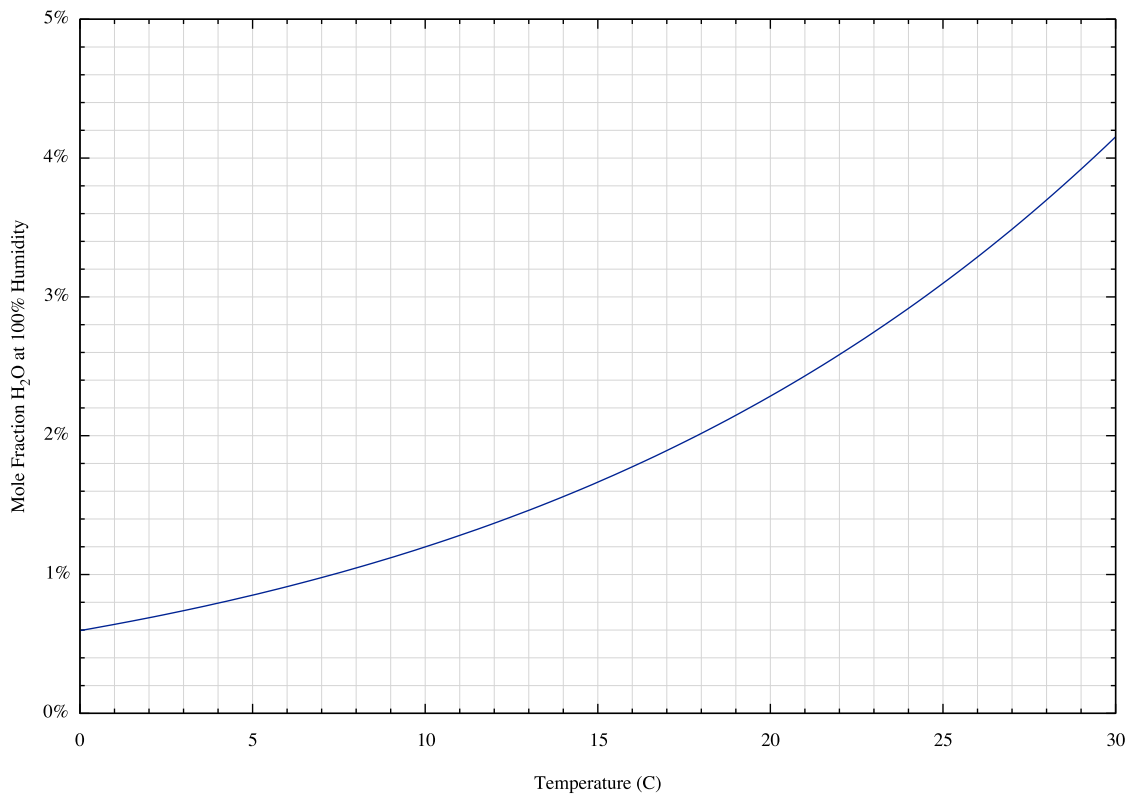


Figure 4.14 Mole Fraction H₂O at 100% Humidity

Over the relevant temperatures, the maximum water content is below 5%. While there is perhaps a 20% increase in diffusivity in water vapor versus air, the maximum increase in gas diffusivity is less than 1%.

In addition, there is appears to be a trend of the lighter species being disproportionately slowed. The humidity effect would, albeit slightly, favor the heavier tracer species. As the diffusivity as determined by the QSSA is unaffected by sorption effects, this can be ruled out.

The remaining option is that the Knudsen pore diameter has been decreased. As shown in Figure 2.3, lighter gas species are more adversely affected by diminished pore sizes than heavier species. This is consistent with the observation here.

The pores are certainly diminished in size if only from volumetric displacement. In addition, because the media is unconsolidated, additional surface tension may cause the particles to pack slightly tighter. Furthermore, as water is a wetting fluid, it may have coated the solid surfaces, thus leaving narrow capillaries, which leave a narrow, but non-tortuous pathway.

Proceeding with this approach, a value for the pore diameter was selected that minimized the deviation in the effective geometries for the tracer species. Using a pore diameter of $1 \mu\text{m}$ results in the following diffusivities:

Table 4.13 Comparison of Nitrogen, Knudsen, and Dusty Gas Diffusivities at $1 \mu\text{m}$

Species	m_i	D_{i,N_2} (cm^2/s)	$D_{i,K}$ (cm^2/s)	D_i (cm^2/s)	$\frac{\varepsilon(1-S)}{q^2}$
Kr	83.80	0.148	0.907	0.128	0.232
Xe	131.29	0.122	0.725	0.104	0.239
SF6	146.06	0.092	0.687	0.081	0.238

As indicated in the table, doing so results in a more consistent porosity-tortuosity-saturation factor amongst the tracer species. However, while contraction of the pore dimensions appears to be possible in the presence of water, it would not explain the

increased diffusive flux or apparent volume of xenon over sulfur hexafluoride. On the contrary, microporous media causes xenon and sulfur hexafluoride much more similarly.

Despite the good correlation, the apparent asymmetry in krypton volumes returned in the wet test. Thought not demonstrable with this data, potential errors may have occurred if there was already ample Kr absorbed into the water prior to beginning the experiment. In contrast, the xenon asymmetry was further reduced. This indicates a far more substantial inventory of xenon may have absorbed into the media, dampening the asymmetry.

Finally, comparing the equilibrium fractions of the tracer species, xenon again converged at the lowest fraction of initial concentration. These are tabulated in Table 4.14

Table 4.14 Apparent Volumes of Tracers in Wet Media versus Argon in Dry Media

Gas	C_{∞}/C_0	$\tilde{V}_i(\text{cm}^3)$	$\tilde{V}_i - \tilde{V}_{Ar}(\text{cm}^3)$
Kr	0.4039	1854	-108
Xe	0.3677	2037	74
SF ₆	0.3810	1965	3

Difficulties in SF₆ analysis make its measurements of questionable value, but nevertheless indicate convergence at a higher fraction. The greatest significance of the xenon convergence is its similarity to the dry case. That is, despite the reduction of approximately 50 mL of gas phase volume, the xenon behaved much the same while the less soluble gases remained more concentrated. Perhaps related to the unexpected asymmetry, krypton converged at an unexpectedly high concentration.

4.8. CONCLUSIONS

While eight trials were detailed here, there were many more trials conducted before reaching a satisfactorily reliable method. The use of either nitrogen or carbon tetrafluoride as an internal standard greatly improved the reliability over the external calibration method. Of these methods, the carbon tetrafluoride was the most reliable.

The results indicate that the porosity-tortuosity factor is a reasonably consistent method of accounting for the effects of dry porous media with macropores. No major significant deviations from theory were observed in the dry case.

In contrast, diffusivity in the wet case behaved unexpectedly. While only slight deviations from nitrogen diffusivity ratios were observed, these were towards a Knudsen diffusion region where heavy gases act more similarly, not less. Thus, no partitioning of xenon from sulfur hexafluoride is expected due to diffusivity.

The largest deviation from the theory as described in chapter 2 was how little the saturation affected the flux. The impact was definitely below that of volumetric displacement effects. As there is a great deal of uncertainty in the tortuosity, these results are consistent with the hypothesis that water is preferentially retained in pores that are less significant for gas transport. Additional testing by these methods on a range of saturations would provide greater insight to this effect. Nevertheless, this effect does not appear to result in selective transport of any species over ordinary gas diffusion.

5. Adsorption of Permanent Gases on Geological Materials

Gas adsorption is the process in which molecules of a gas adhere to the surface of a surrounding liquid or solid. It is further categorized by the strength and selectivity of the interactions between the gas adsorbate and the surface. Strong interactions, on the order of 0.5 eV, that depend on the chemical identity of the gas and surface are known chemisorption. Because of the inertness of both noble gases and sulfur hexafluoride, chemisorption is not anticipated. However, the weaker category of interaction known as physisorption is ubiquitous. Physisorption relies on van der Waals forces between either permanent or instantaneously induced dipoles in the adsorbate and adsorbent.

Molecules composed of two or more elements with differing electronegativity will form permanent dipoles, unless balanced through symmetry. Water is a prime example of this a polar molecule. While sulfur hexafluoride satisfies the first criteria, the octahedral symmetry prohibits the formation of permanent dipoles. In contrast, the noble gases are monoatomic and cannot have permanent dipole moments.

Instead, monoatomic gases and, to a lesser degree, molecules form instantaneous dipoles through London dispersion forces. From the Schrodinger wave equation, electronic wave functions centered on a nucleus are presumed spherically symmetry. However, because electrons also have particle-like properties, there is a probability that, at any given instant, the electron charge will not be evenly distributed. Consequently, an instantaneous dipole may arise even in a solitary monoatomic gas.

When two atoms or molecules approach each other, the instantaneous dipole of one may influence the dipole in the other, perturbing its electron orbitals. This acts to reinforce the dipole and results in an attractive interaction. The strength of this interaction is largely dependent on the diameter of the atomic orbitals and only slightly with molecular diameter. This is a result of the outermost electrons being both located further from the nucleus and partially screened by the inner electrons. Consequently, among the noble gases, radon and xenon will experience the strongest intermolecular forces whereas helium and neon will have the weakest. Furthermore, sulfur hexafluoride will experience relatively weak interactions despite having a greater total number of electrons than xenon as those electrons are all tightly bound.

Very little experimental data is available on the adsorption of xenon geological material, though there is considerably more data available on synthetic materials. One exception is a study exploring the discrepancy of between the abundances of noble gases in the earth atmosphere versus gas samples obtained from. Figure 5.1 displays the relative abundances of primordial noble gas nuclides. Here, primordial means the exclusion of gases formed from decay products, i.e. ^{40}Ar is excluded as it forms from the decay of ^{40}K , but ^{38}Ar , is included.

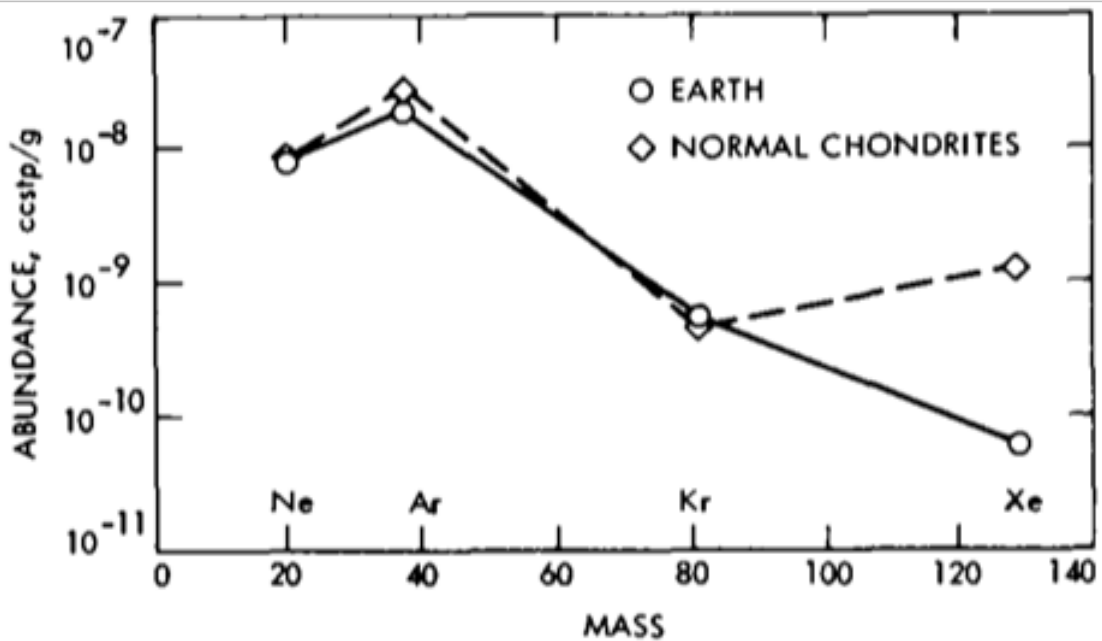


Figure 5.1 Noble Gas Abundances in Atmosphere and Chondrites (Fanale and Cannon 1971)

Presumably, the chondrites were formed by the same stellar nucleosynthesis as the earth. Consequently their noble gas abundances should be well correlated. This corollary holds except for xenon; the atmosphere of the earth has only one-tenth the composition of xenon as a chondrite. Fanale and Cannon have proposed adsorption as a potential mechanism by which planetary primordial xenon is sequestered in the earth's crust. Two shale formations were chosen for the study due to their large abundance and anticipated high adsorption capacity.

As discussed in the transport theory and shown in Figure 2.5, there is nearly an order of magnitude in selectivity for xenon adsorption over krypton adsorption at relevant terrestrial temperatures. The linearity of the plot is representative of physisorption, where adsorbate may form multiple layers or is otherwise not significantly limited by a finite

number of adsorption sites. Because of this linearity, Henry's Law holds and the fraction of total will adsorb even as the gas phase concentration approaches zero.

However, it is not possible to directly apply this data to the discrepancy between xenon and sulfur hexafluoride transport until more data is taken on the latter species. In addition, as the geology at the Nevada Test Site is not predominately shale, the validity of the physisorption model should be confirmed on a variety of substrates.

5.1. METHODOLOGY

To explore this, adsorption isotherms were measured on a variety of geological substrates, using a Micromeritics Flex3 Surface Area Analyzer provided by Dr. Hugh Daigle. Eight geological samples of various rocks were selected to provide a range of material compositions and structures. They were selected to study of the universality of the adsorption effect and to estimate the range of the effect.

Five of the samples were procured from a specimen vendor in the United Kingdom – Geology Superstore. Two were marine shale samples provided by the Daigle group. The final was a limestone sample from Austin, Texas. All of the samples were crushed to a suitable particle size for packing into the chamber for the surface area analyzer. The samples were then heated and flushed with helium overnight to desorb any tightly bound atmospheric gases or water vapor. Samples were evaluated at 0°C and 20°C as these temperatures represent the range of temperatures encountered during underground transport.

5.2. RESULTS:

Data from the Micromeritics Surface Area Analyzer is reported in cubic centimeters of gas at standard temperature and pressure adsorbed per gram mass of substrate. As there are a number of data series, data was collected by species onto individual plots. Figure 5.2 depicts the xenon adsorption measured at both temperatures.

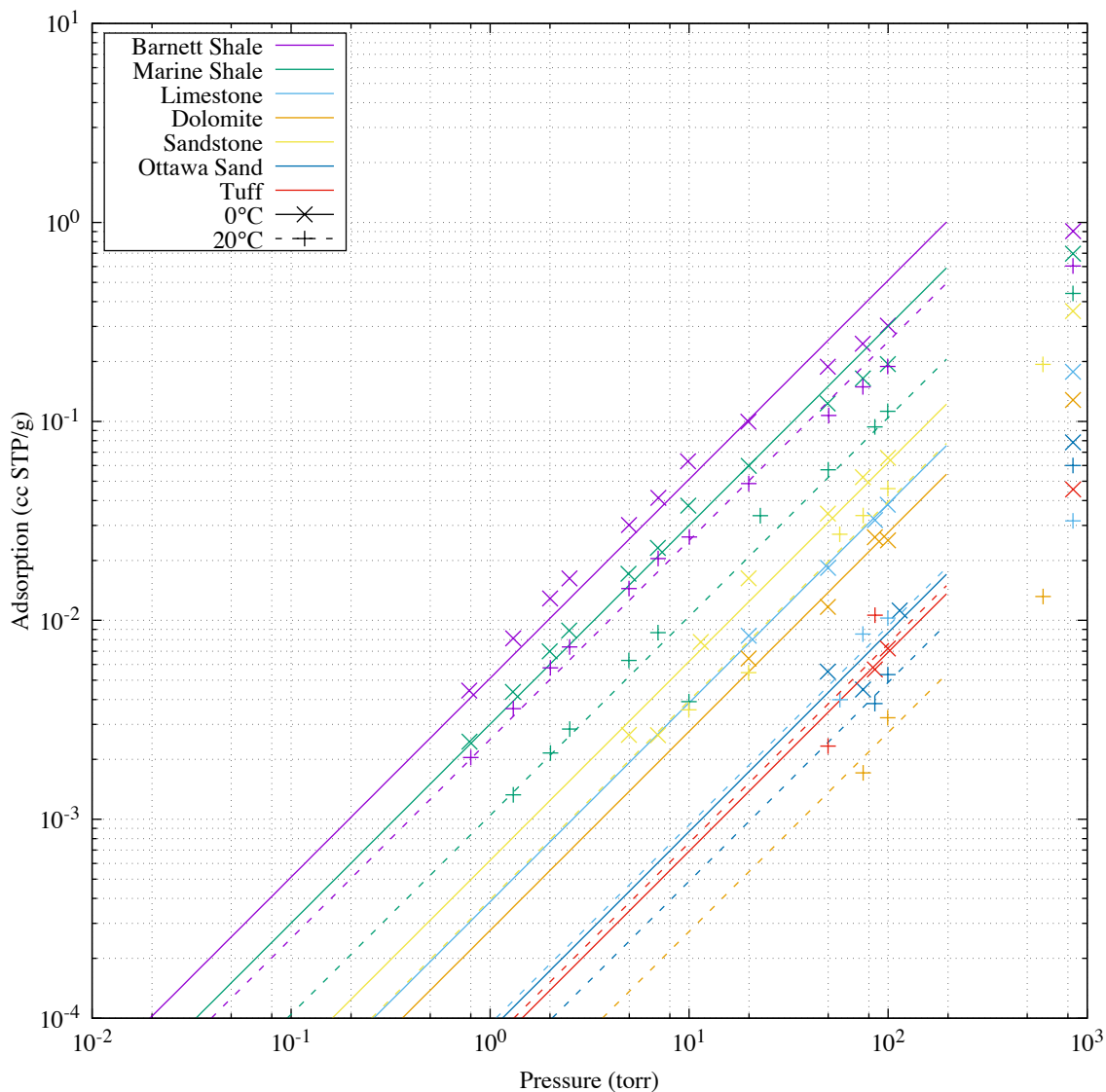


Figure 5.2 Xe Adsorption Isotherms on Geological Media

For xenon, linearity out to approximately 100 torr is confirmed. Because some deviation from linearity occurred about 100 torr, the curve fits were conducted only on points below this threshold. While some deviation occurred in the shale at approximately 80 torr, it did not have a significant impact on the overall strength of adsorption and was utilized for curve fitting. If the isotherm follows Henry's Law, the Henry's Law coefficient can be quickly deduced by the value at which the isotherm cross 1 torr. Here, the Ottawa sand at 20°C was observed to intersect this point at approximately $1\text{E-}4\text{ cm}^3$ at STP/g/torr, which is consistent with the observations from the two-bulb experiments. However, this isotherm is among the weaker adsorption affinities.

Due to weaker adsorption, comparatively less data was within range for sulfur hexafluoride. Figure 5.3 lists the available isotherms. Notably, the comparable Ottawa sand isotherms at 0°C shown SF_6 adsorbing at about one-tenth the levels of Xe. While weaker than the Xe isotherm, the sandstone was unusually strong; potentially indicating the processes is not solely physisorption. However, as the signal response was not great, there is some uncertainty in all of these measurements.

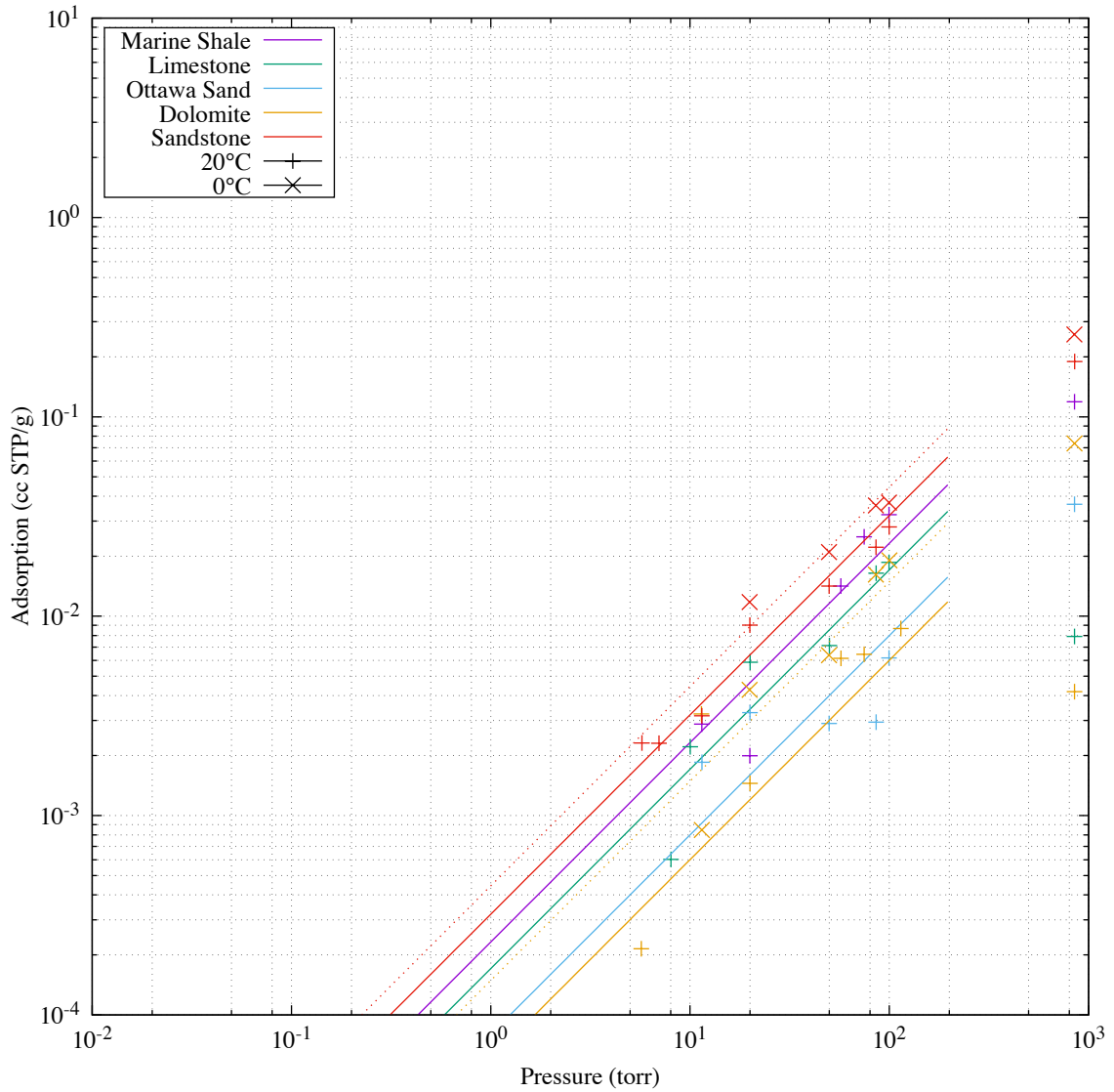


Figure 5.3 SF_6 Adsorption on Geological Media

To confirm the hypothesis that argon was the least adsorbent gas, a few isotherms were measured using this gas. As the effect was expected to be weak, it was restricted to 0°C temperatures.

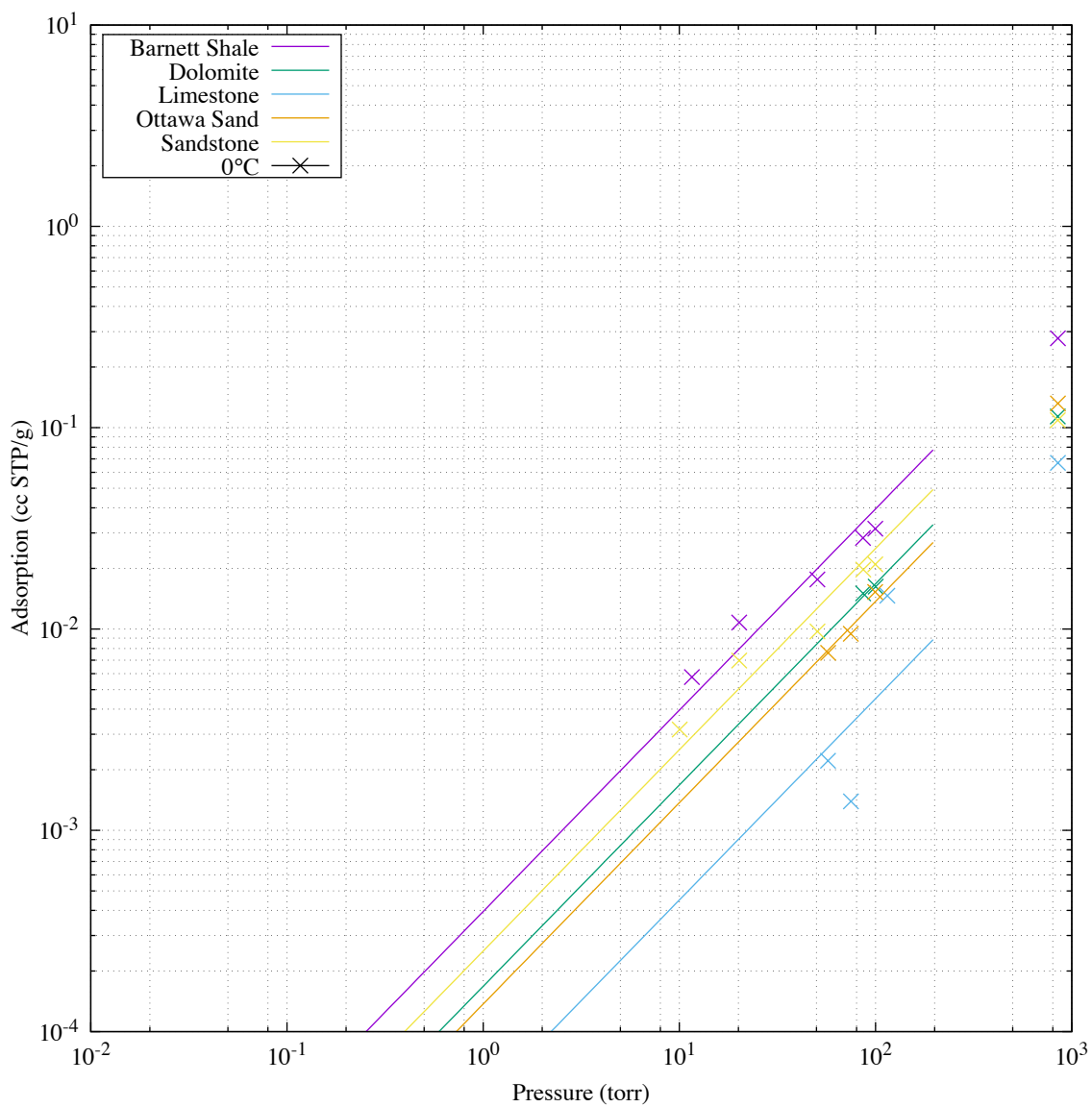


Figure 5.4 Ar Adsorption on Geological Media

As expected, the argon adsorption isotherms are comparatively weak. Even the most sorbent materials are an order of magnitude weaker for Ar than Xe.

5.3. ANALYSIS

From these data, it is apparent that each of these gases has approximately linear isotherms up to the a few torr. As the application is concerned with partial pressures of far below these ranges, saturation of the surface is not a possibility. Behavior at lower partial pressures can be safely estimated by extrapolating with Henry's Law.

Shale materials had the largest specific adsorption, which is anticipated based on their high specific surface area. However, adsorption also occurred on the sandstone, limestone, dolomite, slate, and tuff samples. Slate appeared, in all cases, to be below measureable limits and was not reported. As xenon is of primary interest, the estimated isotherms are reported in the following table:

Table 5.1 Henry's Law Isotherms for Xenon on Geological Materials

Xe Substrate	$K_H(0^\circ C)$ (cc STP/g/torr)	$K_H(20^\circ C)$ (cc STP/g/torr)
Barnett Shale	5.12×10^{-3}	2.52×10^{-3}
Marine Shale	3.01×10^{-3}	1.05×10^{-3}
Limestone	3.85×10^{-4}	9.36×10^{-5}
Dolomite	2.77×10^{-4}	2.73×10^{-5}
Sandstone	6.22×10^{-4}	3.95×10^{-4}
Ottawa Sand	8.68×10^{-5}	4.88×10^{-5}
Tuff	6.91×10^{-5}	7.60×10^{-5}

For comparison, the estimated isotherms from the two-bulb diffusivity test were between 1.14×10^{-4} and 1.21×10^{-4} cc STP/g/torr. Considering the uncertainty in the porosity of the Ottawa sand, these results are consistent. As SF₆ and Ar adsorb considerably less, the differences in apparent volume in the dry diffusivity tests can reasonably be explained by adsorption.

In addition, the data measured for the shale samples were comparable to that reported by Fanale and Cannon. As anticipated, the isotherms were markedly lower for the other materials, but still linear. Comparable adsorption between limestone, dolomite, and sandstone indicate the isotherms are not dramatically affected by chemical composition (CaCO_3 , $\text{CaMg}(\text{CO}_3)_2$, and SiO_2). The specific surface area of the coarse sifted Ottawa sand was markedly different from the grain sizes in the sandstone sample, thus explaining the difference between sandstone and Ottawa sand. Unfortunately, the measurements on Ottawa sand and tuff were near the detection limits and no definitive conclusions can be made for these materials.

Given these isotherms, the logical question is how much do these values affect the volumetric capacity of the porous media. As the samples were crushed for processing, the original porosity cannot be known. If, however, we assume a real geological system is composed of these constituent grains, with various degrees of porosity, the capacity versus porosity can be calculated by:

$$\kappa_i = 1 + \frac{RT}{P} \left(\frac{1}{\varepsilon} - 1 \right) \rho_s K_i$$

Atmospheric pressure will be assumed to be 760 torr in all cases. An approximate grain mass density of 2.62 g/cm^3 for the silica based samples and 2.71 g/cm^3 for the calcium carbonate based samples will be assumed. Using these parameters, Figure 5.5 illustrates the range of capacity factors are possible for materials of various porosity.

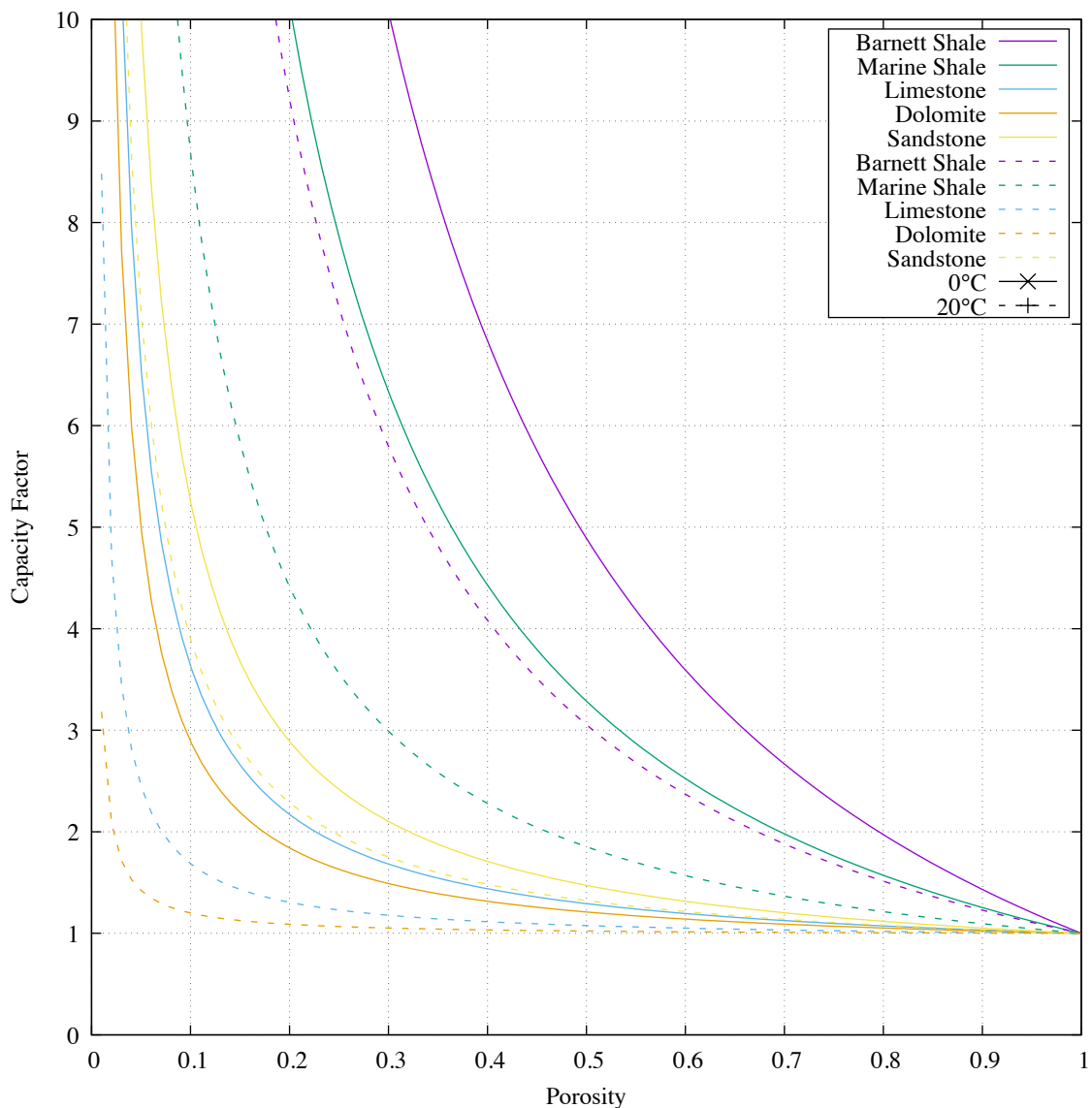


Figure 5.5 Volumetric Capacity vs. Porosity due to Adsorption

From this plot it is evident that, in shale formations, far more xenon is adsorbed than is in the gas phase. That is, the capacity factor is well over two for realistic porosities, and may be well over ten. This further supports the hypothesis of Fanale and Cannon that the missing atmospheric xenon may be adsorbed in the earth's crust.

However, even for sandstone, limestone, and dolomite formations, a non-negligible fraction adsorbs at modest porosities.

The relative magnitude of this effect far exceeds the capacity factor due to solubility in water except at near saturated conditions. Indeed, as discussed in section 2.16, reaching the 1.5 capacity factor necessary for ^{127}Xe to transport similarly to ^{37}Ar appears readily achievable for most media at 20°C. Consequently, differential transport of xenon from the fracture into the matrix is likely even in dry geological systems as well as wet.

5.4. CONCLUSIONS

Noble gases physically adsorb to a variety of geological media, with affinities increasing with atomic number and mass. Sulfur hexafluoride also physically adsorbs to most media, as is to be expected due to its large molecular weight and higher boiling point. However, it does so far less than xenon in most cases. Regardless, this raises the question if either tracer can be considered a conservative tracer over large distances. Limited argon adsorption was demonstrated at 0°C, showing it best represents an ideal tracer.

Clearly, adsorption can account for an increased apparent volume for finite media. However, for infinite media – or a sufficiently radioactive tracer in finite media – this increased capacity must be coupled to a multi-phase transport model to account for the effective dilution as a function of time.

6. Conclusions

Over the course of this work, a number of nuanced findings were made on the properties of inert gas tracers, which deviate from the expected ideality. They can be related to the goals as set forth in the introduction as follows:

6.3. ATTAINMENT OF GOALS

Goal 1: As detailed in the transport theory section, a combined three phase – gas, absorbed liquid, and adsorbed solid – model was derived using elementary arguments. Additionally, consideration was made on the effects of radioactive decay, which may cause an otherwise finite media to act as if infinite. Consequently, the relative importance of the volumetric capacity factor remains a factor over all time frames as in a finite matrix for a stable tracer.

Goal 2: After multiple iterations, an effective and reliable method of quantifying trace gas tracer species was developed. The implementation of this method required the use of internal reference standards to account for systematic error in detector sensitivity and to reduce random error in the sample quantities. The use of trace atmospheric components – $^{15}\text{N}^{14}\text{N}$ – is acceptable for open systems, but if the system can be closed, the use of synthetic gases – here CF_4 – provided more reliable results.

Goal 3: Through the use of a two-bulb apparatus employing a quasi-steady-state approximation, reproducible estimates of the effective diffusivity in porous media were achieved. The porosity-tortuosity factor as discussed in chapter 2 was shown to be

consistent for each tracer species tested when the media was dry. However, the equilibrium concentration fraction was found to be inconsistent by tracer species, indicating the volumetric capacity of the system varied by gas.

In the wet case, the impact of porosity-tortuosity and saturation was nearly consistent by tracer species, but the reduction in porosity-tortuosity with saturation did not follow a simple linear relationship. Potentially, the water is being retained in pore volumes on the more tortuous paths, and the effective pore diameter is being modified, resulting in contributions from the Knudsen diffusion coefficient. Nevertheless, the experimental method in its present form is capable of reliably measuring these effects.

Goal 4: Adsorption isotherms of the tracer species were measured on a variety of geological materials, including the Ottawa Sand packed into the two-bulb apparatus. These measurements confirmed the small variations in equilibrium concentration fraction observed are within bounds of what may be caused by adsorption. Furthermore, for a strongly adsorbing gas, namely xenon, the relative magnitude of the material in the adsorbed phase may exceed the gas phase quantity. This was consistent with the theory of Fanale and Cannon.

6.4. MAJOR FINDINGS RELATED TO TRANSPORT

During the course of this research a number of findings were made. First, the diffusivities of xenon and sulfur hexafluoride are not directly altered by the presence of macroporous media. That is not to say the effective diffusivity is not altered, but only that the diffusivity within a linear pore space is consistent with the bulk gas diffusivities. The

decrease in cross-sectional area and increase in distance due to circuitous routes can be adequately modeled with porosity and tortuosity. At smaller pore dimensions, approximately 1 μm for atmospheric pressures, the diffusivity is adversely affected by Knudsen diffusion. However, the effect of Knudsen diffusion theoretically brings the diffusivities of Xe and SF₆ into closer alignment. This would not explain the apparent high diffusivity of xenon in an underground release.

Secondly, both adsorption and absorption effects are particularly strong for xenon. The high solubility of xenon in water is well studied, but the high physisorption affinity of xenon for geological material is a seldom-studied field. Measurements taken on geological samples for this research are in agreement with the limited literature data that suggests the rarity of xenon in the earth's atmosphere may be a result of this sequestration. In addition, the magnitude of the adsorption effect exceeds that of the absorption effect except at very high degrees of water saturation. While transport of radionuclides to the surface after an underground nuclear explosion is not completely analogous to stellar nucleosynthesis, xenon produced by a nuclear explosive may partition by similar mechanisms.

Third, the increase in volumetric capacity of a matrix due to sorption results in a net increase in the flux from the perspective of the fracture. As adsorption kinetics occur on the time scale of diffusion in a pore, the rate of adsorption-desorption far exceeds the rate of diffusion over meters. In doing so, and solving for the resulting transient reactive-diffusive equation, the flux into the matrix is amplified during periods of accumulation or steady state radioactive decay. Consequently, a gas species with a high capacity factor

may behave analogously to a gas species with a higher diffusivity in either infinite media or when undergoing radioactive decay. The presence of retained groundwater will impact the capacity factor but, as adsorption of xenon on geological materials is strong, significant sorptive capacity may be observed regardless of water content.

Having confirmed that the capacity factor of xenon may very well be in excess of 1.5, this effect can be illustrated by integrating the flux in Figure 2.7 with respect to time. Doing so provides a measure of the dilution factor of a tracer in a matrix due to diffusive flux. Plotting the integrated fluxes on a parametric scale with respect to the reference gas, SF₆, yields Figure 6.1.

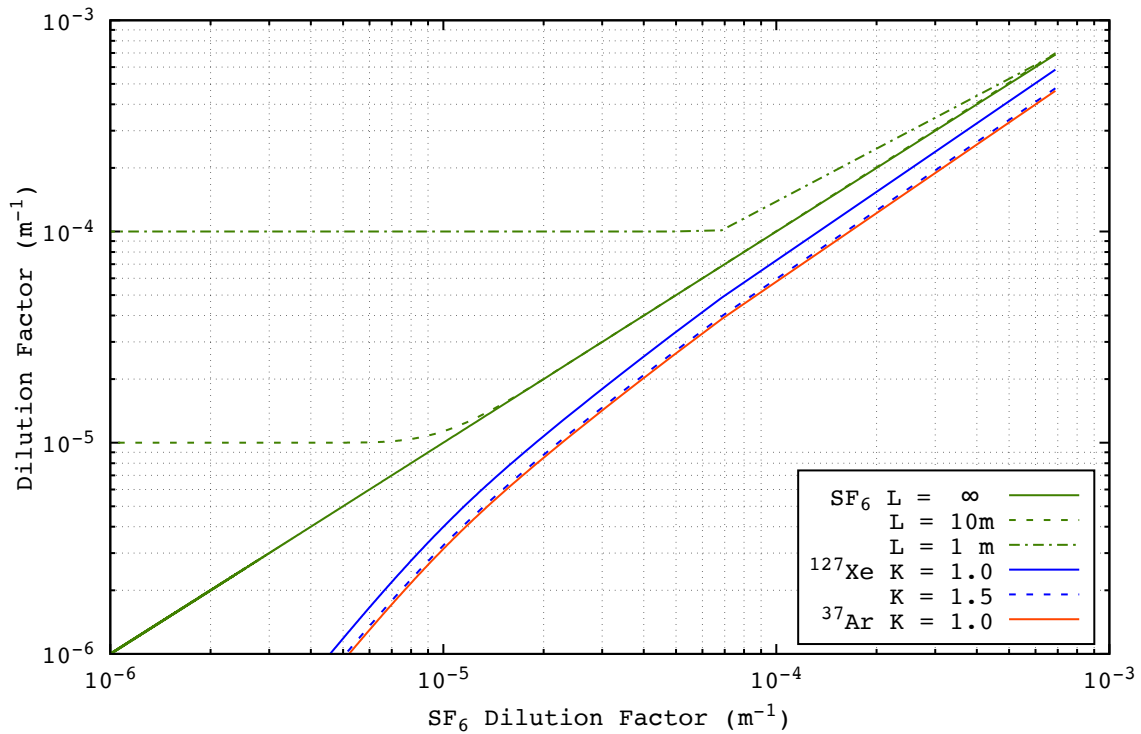


Figure 6.1 Dilution Factor due to a Sorbent Reactive-Diffusive Matrix

In this format, the dilution factor is an indication of the losses into the matrix per unit for fracture-matrix surface area. In comparison, Olsen et al. reported the total dilution factor observed in field tests at the NNSS; see Figure 6.2.

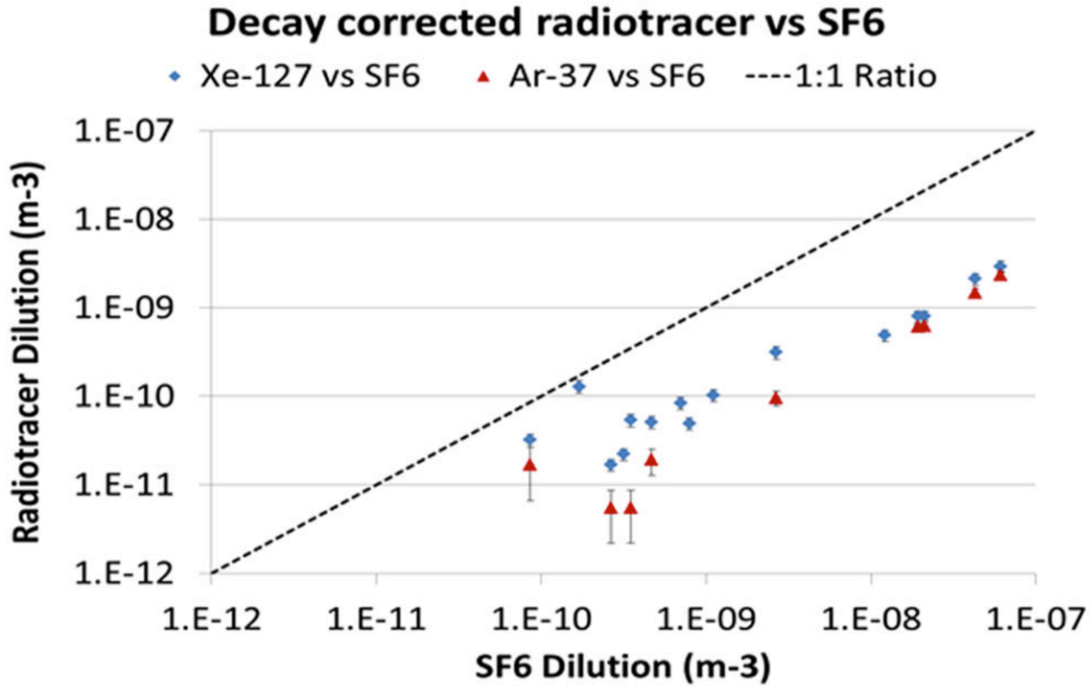


Figure 6.2 Dilution Factor of Tracer Gases at the NNSS (Olsen, et al. 2016)

Because the total fracture-matrix interfacial area is not known, the quantitative results cannot be directly compared. Qualitatively, these results are in agreement with the sorptive transport model demonstrated in this work; the selective sorption of Xe versus Ar or SF₆ results in larger diffusive losses into the matrix.

While the dilution factor assuming an infinite matrix does not yield the approximately ten-to-one ratio of SF₆ to the radioactive tracers, a finite matrix can yield

this degree of selectivity or even greater. In both Figure 2.7 and Figure 6.1, the finite line for SF₆ assumes a matrix length of 10 m. Clearly the finite-medium flux deviates strongly as the finite system reaches equilibrium.

The choice of a singular characteristic matrix length is unlikely to adequately model a real geological system – particularly with transport occurring over multiple strata. Consequently, the diffusive flux of a stable tracer in a field scenario may be subject to infinite boundaries in some formations while be finite in others. As only the cumulative diffusive losses can be measured at the surface, the observed dilution factor will be the summation of losses in each layer. That is, each layer will have its own Fourier modulus and will have its own transient response. Conceptually, a heterogeneous system could be modeled by summing the finite losses in each layer weighed by the area of the corresponding fracture-matrix interface.

More importantly, radioactive tracer gases are indifferent to the dimensions of the matrix provided that the Thiele modulus is large. Thereby, strata that have relatively small dimensions and have negligible contributions to stable gas transport may nevertheless have substantial contributions to radioactive gas transport.

6.3. FINDINGS RELATED TO LABORATORY METHODS

In addition to the conclusions applicable to modeling the transport of radionuclides after a suspected nuclear event, advancements were made in the laboratory methods necessary to produce needed experimental evidence. As noble gases cannot be detected through ordinary molecular spectroscopy not all chemical surrogates, notably

SF₆, can be readily activated, gas chromatography-mass spectroscopy was procured and implemented to support this project.

The implementation of a successful quantitative method was iterative. While high precision measurements are possible with GC-MS, this requires careful selection of equipment, procedures, and experimental planning. Due to the high variability of gas sampling with manual syringes and systematic biases in the mass spectrometer itself, an internal standard was necessary to provide realistic responses. While trace atmospheric gases were used with some success – and are the only option in field experiments – spiking a confined test apparatus with an introduced internal standard yielded superior precision. In addition, the use of a molecular sieve column capable of separating the noble gases yielded less background noise and more symmetric peaks with less integration error.

The use of the quasi-steady state approach to measure diffusivity was success when coupled with GC-MS. As analysis on the samples takes on the order of minutes, other transient methods are unsuitable for this technology. While a fully steady state approach was considered, and would provide operational advantages and potentially higher fidelity diffusivity measurements, the quasi-steady state method was favored for its simplicity of materials. However, to produce quality estimates of diffusivity by this method, development of a numerical algorithm to simultaneously fit the eigenvector and eigenvalues was necessary. In addition to a measurement of diffusivity, this method yields a small indicator of sorption effects. A more generally accepted method of

quantifying these effects is through the use of a surface area analyzer or similar direct pressure measurement instruments.

6.4. RECOMMENDATIONS

Going forward, diffusivity in other geological materials, including micro and mesoporous materials, can be measured through the two-bulb quasi-steady-state method. Measuring the effective diffusivity in consolidated geological materials, particularly with mesoporous or microporous structures may provide additional insight into what the effective Knudsen pore diameter is, and whether the assumption that it is identical for all gases is adequate.

However, with the strong evidence of sorption effects, it is clear that the steady state, or quasi-steady state, response is, while related, not equivalent to the transient response. Unfortunately, GC-MS is unsuitable for rapidly changing tests as time to analyze a sample – approximately 5 minutes – is such that the laboratory test apparatus would need to be excessively large to capture an idealized the transient response.

Instead, an alternative method is to utilize the infinite approximation discussed in section 2.15 for a radioactive tracer. By sizing a test apparatus such the infinite approximation is valid, the desired parameters of diffusivity and capacity are readily calculable. Furthermore, with compatible gamma-emitting radionuclides, this method is minimally invasive – minimizing error in drawing aliquots – and less laborious. Of course this method relies on compatible radionuclides and is not possible for all species, notably SF₆. Details of this concept are discussed in Appendix B.

Appendices

APPENDIX A: QUASI-STEADY-STATE NUMERICAL METHOD

```
## Copyright (C) 2017 Matthew Paul

function [A1,A2,B,C] = quasisteady(x1,y1,x2,y2)

# Tolerance
  tol = 0.001;

## The objective is to find the eigenvalue and eigenvector
that best
## fit the quasi-steady state model.

##  $[y1,y2] = [A1,A2]e^{(-B*x)} + C[1,1]$ 

## Four arrays are passed.
## x1 and x2 are the abscissae
## y1 and y2 are the ordinates

## The parameters A1, A2, B1, and B2 are found by
minimizing the
## weighted squared residuals in linearized space.

  c_high = min(y1) - tol;
  c_low  = max(y2) + tol;
  c_mid  = 0.5 * (c_low + c_high);

  x_high = x1;
  y_high = y1;
  x_low  = x2;
  y_low  = y2;

  e_low  =
quasisteady_error(x_high,y_high,x_low,y_low,c_low);
  e_mid  =
quasisteady_error(x_high,y_high,x_low,y_low,c_mid);
  e_high =
quasisteady_error(x_high,y_high,x_low,y_low,c_high);

# Loop until steady state eigenvector is within tolerances.
```

```

while (c_high - c_low > tol)
# Select the new tightened boundaries
  if sign(e_mid) == sign(e_low)
    c_low = c_mid;
    e_low = e_mid;
  else
    c_high = c_mid;
    e_high = e_mid;
  endif
  c_mid = 0.5 * (c_low + c_high);
  e_mid =
quasisteady_error(x_high,y_high,x_low,y_low,c_mid);
endwhile

## Accept the steady-state eigenvector to be the midpoint
of the final
## estimates.
  C = (c_high + c_low) / 2;

## Calculate the transient eigenvector and eigenvalue based
on the
## final steady-state eigenvector.
  [a_1,b_1,ssr_high] = quasisteady_fit(x_high,y_high-C);
  [a_2,b_2,ssr_low ] = quasisteady_fit(x_low ,C-y_low );

  A1 = exp(a_1)
  A2 = -exp(a_2)
  B = 0.5 * (b_1 + b_2)

Endfunction

```

```

function [db] =
quasisteady_error(x_high,y_high,x_low,y_low,c)
## Find the squared difference in the transient eigenvalue
B subject to
## the steadystate eigenvector C.

    [a_high,b_high,ssr_high] = quasisteady_fit(x_high,y_high-
c);
    [a_low ,b_low ,ssr_low ] = quasisteady_fit(x_low,c-
y_low);

    db = b_high-b_low;

endfunction
function [a,b,ssr] = quasisteady_fit(x, y)
## Find the least squares fit subject to logarithmic error
weighting.

    syy = sum(y.*y);
    sxyy = sum(x.*y.*y);
    sxxyy = sum(x.*x.*y.*y);
    syyly = sum(y.*y.*log(y));
    sxyyly = sum(x.*y.*y.*log(y));

    denominator = syy*sxxyy-sxyy**2;

    a = (sxxyy*syyly - sxyy*sxyyly) / denominator;

    b = (syy*sxyyly - sxyy*syyly) / denominator;

    err = y - exp(a+b*x);

    ssr = sum(err.*err);
endfunction

```

APPENDIX B: SEMI-INFINITE APPROXIMATION FOR RADIOACTIVE TRACERS

Recalling that the decay length of many of the noble gas radionuclides was on the order of meters in air – see Table 2.2 – and would be further reduced by the porosity-tortuosity; it is not unreasonable to construct a test apparatus with a Thiele Modulus well in excess of two for most species. As under these conditions, the diffusion of the tracer in a closed system would be equivalent to that of stable tracer in an infinite medium. Consequently, unlike the steady-state methods, the transient accumulation due to sorptive capacity can be captured along with the effective diffusivity.

The response for this system subject to an impulse source would be that of the kernel of the Green's function discussed in section 2.15:

$$c_i(x, t) = c_0 \frac{e^{-\lambda_i t - \frac{\kappa_i x^2}{4\mathcal{D}_i t}}}{\sqrt{2\lambda_i t}}$$

As the half-lives of the tracer species are well known, there are essentially constants – although they govern the size such an apparatus must be. Locating a high-purity germanium (HPGe) detector at a fixed but known distance from the injection results in the intensity of the radiation as a function of time and two unknown parameters.

$$I_i(t) = \frac{A_i}{\sqrt{t}} e^{-\lambda_i t - \frac{B_i}{t}}$$

The parameter A_i represents the total quantity of the radionuclide injected and counting efficiencies. However, the only requirement of such a test is that these be constant with time. The second parameter is sufficient to determine the diffusivity and capacity given accurate measurements of time and position:

$$B_i = \frac{\kappa_i x^2}{4\mathcal{D}_i}$$

Previously at NETL, Carlos Perez had conducted an exploratory study in a 1-m cylinder, partially packed with silica sand, with three xenon isotopes: ^{125}Xe , ^{133}Xe , and ^{135}Xe . Data was acquired in list-mode so that both the timing and energy of detected radiation is recorded. While no analysis has been published on this experiment to date, the data fits this theoretical model proposed in chapter 2.15 well for ^{125}Xe and ^{135}Xe . A plot of the list-mode data and the impulse response function fits – with the error weighted appropriately for counting statistics – are shown in the following figure:

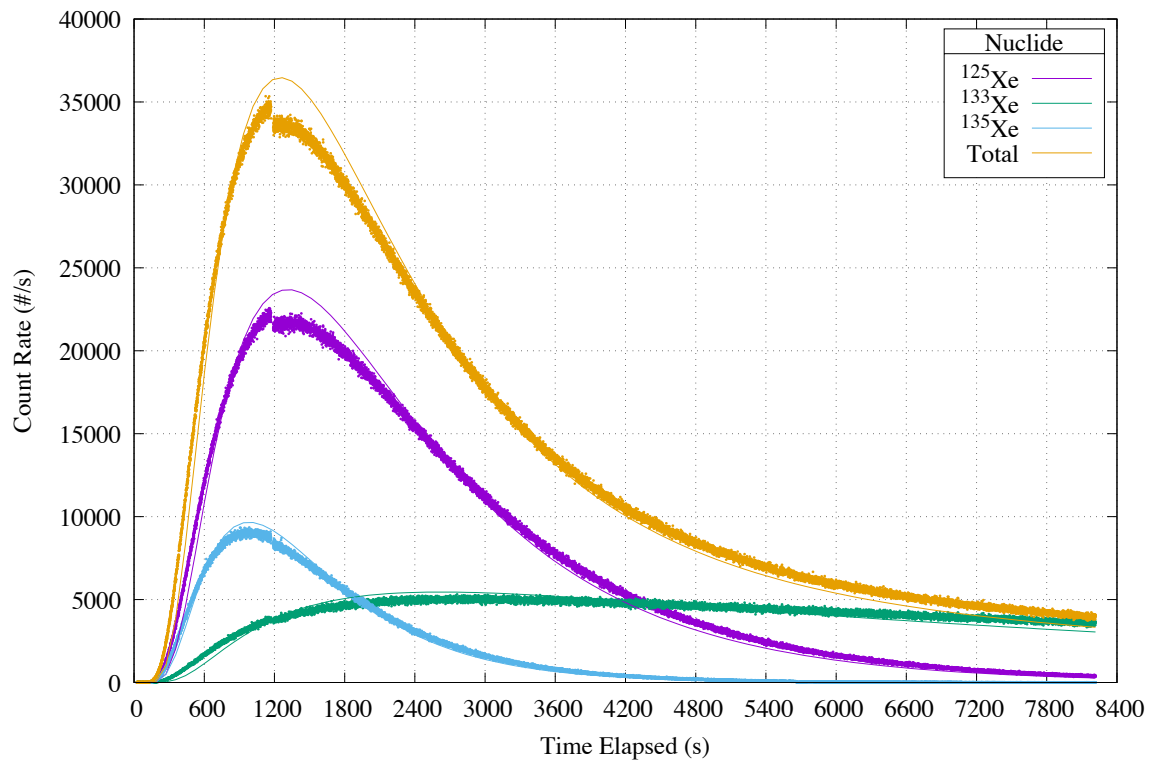


Figure B.1 Infinite Approximation Fit vs. List-Mode HPGe Data for Radioxenon

Qualitatively, the infinite reactive-diffusive solution is quite good. Unfortunately, there are two regions that are deficient that prevent this data from being directly utilizable. First, there is clearly a discontinuity located near 1200 seconds. This occurred again at approximately 5500 seconds, but with less deleterious effect. In addition to the discontinuity that is pictures, there were additional clearly spurious data points – count rates near zero – that were removed as they negatively impacted the curve fitting procedures. It is believed there was a hardware malfunction, as the counting rate does not appear to have immediately returned to its pre-failure state.

Even without the discontinuity, there is still a large gap near the peak count rate. It appears only the real-time of the measurements was collected and no adjustments were made for counter dead time. Consequently, the peak activity reported here is likely an underestimate of the live-time activity. Adjusting the peak activity upwards would provide an even better qualitative fit and would subsequently correct the slight deviations in the leading and trailing edges.

Aside from the quality of the graphical fits, the following quantitative parameters were found:

Table B.1 Infinite-Approximation Parameters for Radioxenon Isotopes

Radionuclide	A (#/s ^{1/2})	B(s)
¹²⁵ Xe	8.548x10 ⁶	1839
¹³³ Xe	7.440x10 ⁵	1938
¹³⁵ Xe	5.979x10 ⁶	1711

As the first parameter, A_i , is a function of initial activity and counting efficiency for the channel, no intrinsic properties can be deduced directly or indirectly without

knowing accurate information on the quantity of the released source and counting geometries. Therefore, this parameter has little meaning unless it is time varying – as it appears was the case due to dead time.

The second parameter, B_i , is, however, far more valuable. Provided with an accurate measurement of distance – and a homogeneous diffusion medium - a direct measurement of the diffusivity and capacity can be found.

Here, the detector position was not recorded, but still the ratio of these parameters provides a relative measure of the diffusivity and capacity.

$$\frac{B_i}{B_j} = \frac{\mathcal{D}_j \kappa_i}{\mathcal{D}_i \kappa_j}$$

Thus, for two radionuclides of the same chemical species, the capacity factors are the same and the relative values of the diffusivities can determine isotopic fractionation. Here, the ^{135}Xe data is likely the most reliable, and the parameters for ^{125}Xe and ^{133}Xe are flattened out by the discontinuity introduced by hardware failure and lack of accounting for dead time. In addition, as ^{133}Xe has a somewhat longer half-life, the 1-m size may not have been a quite large enough for the infinite approximation. This can be observed as the magnitude of the deviation between fit and reported values is increasing near the end of the experiment. However, it is not be unreasonable to use a marginally longer pipe than 1 m for ^{133}Xe .

The major advantage of this method is utilizing tracers of different chemical species. Ideally, a comparison could be made between ^{37}Ar and the four radioxenon species of interest to the CTBT. As ^{37}Ar decays through electron capture and has a half-

life of it is not ideal for a laboratory test. Fortunately, ^{41}Ar decays are accompanied by a 1294-keV gamma ray. Additionally, ^{41}Ar has a half-life of 109.6 minutes, so despite its higher diffusivity, the required length for a large Thiele Modulus is comparable to that of ^{135}Xe – half-life 548.4 minutes. Provided with ^{41}Ar and radioxenon data, a direct assessment of the combined diffusivity and capacity factors can be made.

The major limitation of this proposed method is that the gas must be a gamma-emitter and, as such, cannot be used with stable tracers such as SF_6 . Therefore, it is more of a niche application compared with the general GC-MS method discussed in chapter 4. But as ^{41}Ar and ^{135}Xe meet the criteria of gamma-emitters with acceptable half-lives, and it is relatively easy to scale the diffusivity of isotopes versus chemical species, this may not be a significant limitation for research supporting the CTBT.

Bibliography

Bateman, H. "Solution of a System of Differential Equations Occuring in the Theory of Radio-active Transformations." *Proc. Cabridge Philos. Soc.* 15 (1910): 423-427.

Baum, E. M., M. C. Ernesti, H. D. Knox, T. R. Miller, and A. M. Watson. *Nuclides and Isotopes*. 17th ed. Schenectady, NY: BMPC, 2010.

Bear, Jacob. *Dynamics of Fluids in Porous Media*. New York, NY: American Elsevier, 1972.

Bird, Robert Byron, Warren E. Stewart, and Edwin N. Lightfoot. *Transport Phenomena*. 2nd Ed. New York, NY: John Wiley & Sons, 2002.

Bridgeman, O. C., and E. W. Aldrich. "Vapor Pressure Tables for Water." *J. Heat Transfer* 86, no. 2 (1964): 279-286.

Carman, Philip Crosbie. *Flow of Gases Through Porous Media*. New York, NY: Academic Press, 1956.

Carrigan, C. R., R. A. Heinle, G. B. Hudson, J. J. Nitao, and J. J. Zucca. "Trace Gas Emissions on Geological Faults as Indicators of Underground Nuclear Testing." *Nature* 382, no. 6591 (August 1996): 528-531.

Chapman, Sydney, and T. G. Cowling. *The Mathematical Theory of Non-Uniform Gases*. 3rd Edition. New York, NY: Cambridge University Press, 1970.

Clever, H. Lawrence. *Argon: IUPAC Solubility Data Series*. Vol. 4. Oxford: Pergamon Press, 1980.

—. *Helium and Neon: IUPAC Solubility Data Series*. Vol. 1. Oxford: Pergamon Press, 1979.

Clever, H. Lawrence. "IUPAC-NIST Solubility Data Series. 80. Gaseous Fluorides of Boron, Nitrogen, Sulfur, Carbon, and Silicon and Solid Xenon Fluorides in all Solvents." *Journal of Physical and Chemical Reference Data* 34, no. 1 (2005): 201-438.

—. *Krypton, Xenon and Radon: IUPAC Gas Solubility Data Series*. Vol. 2. Oxford: Pergamon Press, 1979.

Comprehensive Nuclear-Test-Ban Treaty Organization. *International Monitoring System: Global Overview*. March 16, 2017. https://www.ctbto.org/tiles/pdf/CTBTO-Map-IMS-2017-03-16-All_Stations-Overview.pdf (accessed March 16, 2017).

Cotton, F. Albert, and Geoffrey Wilkinson. *Advanced Inorganic Chemistry: a Comprehensive Text*. New York, NY: Interscience Publishers, 1972.

Crank, J. *The Mathematics of Diffusion*. 2nd Ed. New York, NY: Oxford University Press, 1975.

Egnatuk, Christine M, and Steven R. Biegalski. "Radioargon production through the irradiation of calcium oxide." *J Radioanal Nucl Chem* 298 (2013): 475-479.

Egnatuk, Christine Marie. *Radioargon Production at the University of Texas at Austin*. Dissertation, Austin, TX: The University of Texas at Austin, 2012.

Ettre, L. S. "Nomenclature for Chromotography." *Pure & Appl. Chem.* 65, no. 4 (1993): 819-872.

Fanale, F. P., and W. A. Cannon. "Physical adsorption of rare gas on terrigenous sediments." *Earth and Planetary Science Letters* 11 (1971): 362-368.

Farlow, Stanley J. *Partial Differential Equations for Scientists and Engineers*. New York, NY: Dover Publications, 1993.

Haas, D. A., S. R. Biegalski, and K. M. Foltz-Biegalski. "Radioxenon Production through Neutron Irradiation of Stable Xenon Gas." *Journal of Radioanalytical and Nuclear Chemistry* 282 (2009): 677-680.

Hayter, Anthony J. *Probability and Statistics for Engineerings and Scientists*. 2nd Edition. Pacific Grove, CA: Duxbury Thomson Learning, 2002.

Israelachvili, Jacob N. *Intermolecular and Surface Forces*. 3rd ed. San Diego, CA: Academic Press, 2011.

Jong, Edmund C., Paul V. Macek, Inoka E. Perera, Kray D. Luxbacher, and Harold M. McNair. "An Ultra-Trace Analysis Technique for SF₆ Using Gas Chromatography with Negative Ion Chemical Ionization Mass Spectrometry." *J Chromatogr Sci* 53, no. 6 (2014): 854-859.

Katakura, Jun-ichi. *JENDL FP Decay Data File 2011 and Fission Yields Data File 2011*. Tokai: JAEA, 2011.

Kranz, A. Z., and W. W. Watson. "Chlorine Isotope Separation by Thermal Diffusion." *Phys. Rev.* (American Physical Society) 91, no. 6 (Sep 1953): 1469-1472.

Kreyszig, Erwin. *Advanced Engineering Mathematics*. 5th Edition. New York, NY: John Wiley & Sons, 1983.

Leddicotte, G. W. *The Radiochemistry of Sulfur*. Washington, DC: Department of Commerce, 1962.

Leonardi, Erminia, and Celestino Angeli. "On the Maxwell-Stefan Approach to Diffusion: A General Resolution in the Transient Regime for One-Dimensional Systems." *J. Phys. Chem. B* 114 (2010): 151-164.

Lowrey, Justin David. *Subsurface Radioactive Gas Transport and Release Studies using the UTEX Model*. Dissertation, Department of Mechanical Engineering, Austin, TX: The University of Texas at Austin, 2013.

Marrero, T. R., and E. A. Mason. "Gaseous Diffusion Coefficients." *J. Phys. Chem. Ref. Data*. 1, no. 1 (1972): 3-118.

Mason, E. A., and A. P. Malinauskas. *Gas Transport in Porous Media: The Dusty-Gas Model*. New York, NY: Elsevier, 1983.

McQuarrie, Donald A. *Statistical Mechanics*. Sausalito, CA: University Science Books, 2000.

McQuarrie, Donald A., and John D. Simon. *Physical Chemistry: a Molecular Approach*. Sausalito, CA: University Science Books, 1997.

Myers, A. L., and J. M. Prausnitz. "Thermodynamics of Mixed-Gas Adsorption." *AIChE Journal* 11, no. 1 (Jan. 1965): 121-127.

Ney, Edward P., and Fontaine C. Armistead. "The Self-Diffusion Coefficient of Uranium Hexafluoride." *Physical Review* 71, no. 1 (Jan 1947): 14-19.

Nilson, R. H., E. W. Peterson, K. H. Lie, N. R. Burkhard, and J. R. Hearst. "Atmospheric pumping: A mechanism causing vertical transport of contaminated gases

through fractured permeable media." *Journal of Geophysical Research: Solid Earth* 96, no. B13 (12 1991): 21933–21948.

Ogata, Akio, and R. B. Banks. *A Solution of the Differential Equation of Longitudinal Dispersion in Porous Media*. USGS, Washington: US GPO, 1961.

Olsen, K. B., et al. "Noble gas migration experiment to support the detection of underground nuclear explosions." *J Radioanal Nucl Chem* 307 (2016): 2603-2610.

Paul, Matthew J., Steven R. Biegalski, Derek A. Haas, and Justin D. Lowrey. "Diffusive Transport of SF₆ vs. Xe in a Porous Media Column." Austin, TX, Dec 2015.

Riley, K. F., M. P. Hobson, and S. J. Bence. *Mathematical Methods for Physics and Engineering*. 2nd Ed. Cambridge: Cambridge University Press, 2004.

Ringbom, Anders, and Harry Miley. "Radionuclide Monitoring." *Science for Security*. Vienna: CTBTO, 2009. 23-28.

Robertson, J. B. *Behavior of Xenon-133 Gas After Injection Underground: Molecular Diffusion, Materials Balance, and Barometric Pressure Effects*. Idaho Falls, ID: USGS, 1969.

Saey, Paul R.J. "Ultra-Low-Level Measurements of Argon, Krypton, and Radioxenon for Treaty Verification Purposes." *ESARDA Bulletin* 36 (June 2007): 42-56.

Sanloup, Chrystèle, Burkhard Schmidt, Eva Maria Chamorro Perez, Albert Jambon, Eugene Gregoryanz, and Mohamed Mezouar. "Retention of Xenon in Quartz and Earth's Missing Xenon." *Science* 310 (November 2005): 1174-1177.

Schulze, Joachim, Matthias Auer, and Robert Werzi. "Low level radioactivity measurement in support of the CTBTO." *Applied Radion and Isotopes* 53 (2000): 23-30.

Shcheka, Svyatoslav S., and Hans Keppler. "The origin of the terrestrial noble-gas signature." *Nature* 490 (October 2012): 531-534.

Smith, J. M., H. C. Van Ness, and M. M. Abbott. *Introduction to Chemical Engineering Thermodynamics*. 6th. Boston, MA: McGraw-Hill, 2001.

Stein, S. E. "Mass Spectra." In *NIST Chemistry WebBook, NIST Standard Reference Database Number 69*, edited by P. J. Linstrom and W. G. Mallard. Gaithersburg, MD: National Institute of Standard and Technology, 2014.

Thiele, E. W. "Relation between Catalytic Activity and Size of Particle." *Industrial and Engineering Chemistry* 31, no. 7 (July 1939): 916-920.

Thorstenson, D. C., and D. W. Pollock. "Gas Transport in Unsaturated Zones: Multi-Component Systems and the Adequacy of Fick's Laws." *Water Resources Research* 25, no. 3 (Mar. 1989): 477-507.

Tuli, Jagdish K. *Nuclear Wallet Cards*. 7th Ed. Upton, NY: National Nuclear Data Center, 2005.

United States Committee on Extension to the Standard Atmosphere. *U.S. Standard Atmosphere: 1962; ICAO Standard Atmosphere to 20 Kilometers; Proposed ICAO Extension to 32 Kilometers; Tables And Data to 700 Kilometers*. Washington, D.C.: U.S. Govt. Print. Off., 1962.

Welty, James R., Charles E. Wicks, Robert E. Wilson, and Gregory Rorrer. *Fundamentals of Momentum, Heat, and Mass Transfer*. 4th ed. New York, NY: John Wiley & Sons, Inc., 2001.

Wise, D. L., and G. Houghton. "Diffusion coefficients of neon, krypton, xenon, carbon monoxide and nitric oxide in water at 10-60C." *Chemical Engineering Science* (Pergamon Press) 23 (1968): 1211-1216.

Zalc, Jeffrey M., Sebastián C. Reyes, and Enrique Iglesia. "The effects of diffusion mechanism and void structure on transport rates and tortuosity factors in complex porous structures." *Chemical Engineering Science* 59 (2004): 2947-2960.

Vita

Matthew John Paul was born in Pittsburgh, Pennsylvania and attended Shaler Area High School. He studied Chemical and Biomolecular Engineering at the Georgia Institute of Technology, graduating in 2007. He then continued his Chemical Engineering education at the University of California at Santa Barbara, completing a Master of Science degree in 2009. Afterwards, he accepted a thermal-hydraulic engineering position at the Bettis Atomic Power Laboratory. In 2015, he returned to full-time graduate studies at The University of Texas at Austin in the Nuclear and Radiation Engineering program within the Mechanical Engineering Department.

Permanent email address: mpaul@utexas.edu

This dissertation was typed by the author.